Title

Low-Energy Control of Magnetization Dynamics for Magnetic Computing

Author

Nance, John Austin

Publication Date

2021

UNIVERSITY OF CALIFORNIA

Los Angeles

Low-Energy Control of Magnetization Dynamics for Magnetic Computing

A dissertation submitted in partial satisfaction of the
requirements for the degree of Doctor of Philosophy
in Mechanical Engineering

by

John Austin Nance

2021

ABSTRACT OF THE DISSERTATION

Low-Energy Control of Magnetization Dynamics for Magnetic Computing

by

John Austin Nance
Doctor of Philosophy in Mechanical Engineering
University of California, Los Angeles, 2021
Professor Gregory P. Carman, Chair

Magnetism plays a significant role in the field of computing, both as a medium on which data is stored, as well a physical phenomenon by which next-generation, non-boolean computation is conducted. Most computing applications that utilize magnetism rely on ferromagnetic materials, electric current-based write methods, and steady-state excitation. While these choices have served us well up to this point, our computing needs are changing more now than ever. The need for more energy efficient computer memory, and the goal of producing powerful next-generation computing architectures like neural networks, require investigation into new magnetic materials, new methods of magnetic control, and new excitation schemes. It is the focus of this dissertation to investigate these topics in the context of three computing applications, image recognition, neuromorphic computing, and magnetic memory. Hardware solutions that are suitable for solving the quadratic optimization problems associated with image recognition are currently under development with the goal of replacing slow, expensive software algorithms. One example utilizes an array of nanomagnetic elements to solve this quadratic optimization problem, but faces an issue of array programmability. Here, dynamic application of spin-orbit torque is investigated as an energy efficient method of magnetic array programmability to enable array re-usability in this non-boolean computing architecture. In the field of neuromorphic computing, there is a need for a high-speed, energy efficient programmable synapse for use in AI systems that must adapt in real-time to continuous data streams. On this front, the utility of a multiferroic antiferromagnetic material is studied, and an upper bound on strain-mediated antiferromagnetic programming is determined. Finally, the last area focused on in this work is magnetic memory. In the current state of the art, magnetic elements with perpendicular anisotropy are switching between binary states using spin-orbit torque. This type of switching requires breaking OOP symmetry, with many mechanisms of symmetry breaking having been proposed. In this work, a symmetry breaking mechanism utilizing intrinsic material properties is studied in combination with voltage-induced strain, with the goal of reducing the dependency on electric current in magnetic memory applications.

The dissertation of John Austin Nance is approved.

Kang L. Wang
Robert N. Candler
Yongjie Hu
Gregory P. Carman, Committee Chair

University of California, Los Angeles
2021

Table of Contents

List of Figures

Acknowledgements

The first time I spoke with Professor Carman was when he called me in 2017 and, in the space of 10 minutes, convinced me not only to choose UCLA for my graduate studies, but also to switch from the Masters program that I applied for to a PhD. Over the past four years, I’ve never regretted that decision. I have grown immensely as a researcher and as a person thanks to Professor Carman’s guidance and I know that I would not be where I am today if he hadn’t decided to call me that day in 2017. I owe just as much to my fellow members of the Active Materials Laboratory. The work shown here is as much theirs as it is mine, for all the questions they’ve answered and ideas they’ve inspired. Whether it be driving across town for authentic dim sum, or fishing off of a boat miles out to sea, my labmates have made my time at UCLA thoroughly enjoyable. Finally, I would like to thank my family and friends both here in California and back in North Carolina. Their support, advice, and time have been precious to me and I can’t imagine that I would have finished this degree without them.

This material is based upon work supported by or in part by the U.S. Army Research Office and the NSF Nanosystems Engineering Research Center for Translational Applications of Nanoscale Multiferroic Systems (TANMS). The work discussed in Chapter 2 is a version of *J. A. Nance, K. A. Roxy, S. Bhanja and G. P. Carman, "Spin–Orbit Torque and Dipole Coupling for Nanomagnetic Array Programmability," in IEEE Transactions on Magnetics, vol. 56, no. 7, pp. 1-8, July 2020, Art no. 1300108, doi: 10.1109/TMAG.2020.2995514.* In particular, I would like to acknowledge Dr. Kawsher Roxy for the data presented in Figures 2-2 and 2-3, as well as both Dr. Sanjukta Bhanja and Dr. Kawsher Roxy for their discussion and collaboration in the work presented in Chapters 2 and 3.

VITA

Education

2017 – 2019	M.S. in Mechanical Engineering University of California, Los Angeles
2013 – 2017	B.S. in Physics University of North Carolina, Chapel Hill

Employment History

2017 – 2021	Graduate Student Researcher University of California, Los Angeles
2021	Hardware Engineering Internship Apple, Inc. (Los Angeles, CA)
2015 – 2017	Undergraduate Researcher MAJORANA Collaboration, UNC – Chapel Hill
2017	Research Intern National Institute for Materials Science, Tsukuba, Japan
2016	Research Intern Sensors and MEMS/NEMS Lab, Georgia Institute of Technology

Publications

J. A. Nance, K. A. Roxy, S. Bhanja, and G. P. Carman, "Spin-Orbit Torque and Dipole Coupling for Nanomagnetic Array Programmability," *IEEE Trans. Magn.*, vol. 56, no. 7, pp. 1–1, 2020, doi: 10.1109/tmag.2020.2995514.

J. A. Nance, K.A. Roxy, S. Bhanja, and G. P. Carman, "Antiferromagnetic Multiferroic Artificial Synapse for Neuromorphic Computing Applications,". *To be submitted*

H. Wu, J. Nance, S. A. Razavi, D. Lujan, B. Dai, Y. Liu, H. He, B. Cui, D. Wu, K. Wong, K. Sobotkiewich, X. Li, G. P. Carman, and K. L. Wang, "Chiral Symmetry Breaking for Deterministic Switching of Perpendicular Magnetization by Spin-Orbit Torque," *Prepr. à Ref.*, vol. 21, no. 1, pp. 515–521, 2021, doi: 10.1021/acs.nanolett.0c03972.

H. Wu, … , J. A. Nance, *et al.*, "Magnetic memory driven by topological insulators," *Nat. Commun.*, vol. 12, no. 1, pp. 1–7, 2021, doi: 10.1038/s41467-021-26478-3.

F. Kargar, M. Balinskiy, H. Chiang, A. C. Chavez, J. Nance, A. Khitun, G. P. Carman, and A. A. Balandin, "Brillouin-Mandelstam spectroscopy of stress-modulated spatially confined spin waves in Ni thin films on piezoelectric substrates," *J. Magn. Magn. Mater.*, vol. 501, 2020, doi: 10.1016/j.jmmm.2020.166440.

1 Introduction

Thousands of years ago, there lived a shepherd in ancient Greece named Magnes. One day, as he was tending to his sheep, Magnes noticed that the nails in his shoes and the metal in his crook were stuck to a rock underfoot. He unearthed the rock and in doing so, procured the first lodestone acknowledged in written history. While the historical accuracy of this tale is impossible to confirm, Magnes is often credited with the discovery of magnetism. Lodestones are comprised of magnetite and have a strong naturally occurring magnetization. Because of this, humans have used lodestones as compasses for thousands of years. By observing the behavior of the stone within earth's magnetic field, one can determine their orientation. Even today, modern navigation relies on compasses that use the same principle of operation. The behavior of a small magnetic material within earth's magnetic field is used to determine the device's orientation. But while this basic principle is the same, modern compasses are orders of magnitude smaller, faster, and more sensitive. These improvements came about because over the thousands of years that have passed since magnetism was discovered, we have studied it in depth and learned a great deal. This allows us to take advantage of magnetic properties unknown to our ancestors, like magnetoresistance (MR) or the Hall effect. Today, this study is ongoing and new magnetic properties are always being discovered, meaning that continued improvements on existing magnetic systems are inevitable.

This work focuses on using novel magnetic properties to develop improvements in two fields to which magnetism is essential, computer memory and non-boolean computation. Regarding computer memory, magnetoresistive random access memory (MRAM) has garnered significant attention due to its prospective benefits in speed, energy efficiency, endurance, and non-volatility over traditional CMOS based RAMs (static/dynamic RAM) [1]. Similarly, magnetism is utilized in the field of non-boolean computing to help solve problems that would be unwieldy for conventional computers, like image or pattern recognition [2]. The type of magnets utilized in both fields are typically ferromagnetic (FM) and are usually controlled using electric-current mediated read and write processes. These two factors intrinsically limit the speed and efficiency of these devices. By taking advantage of novel magnetic properties and materials, and focusing on magnetization dynamics, further improvements in energy efficiency, speed, and device size can be achieved.

1.1 Magnetic Memory

As we progress onward into the age of the internet, our reliance on apps, websites, and online services is steadily increasing. One consequence of this is the never-ending production of an enormous amount of data. Whether it be information as inane as your favorite tweets, or as important as your medical records, all of this represents data that must be physically stored somewhere. This storage usually happens in hard drives comprised of small magnetic bits, in which an electric current can be used to read and write information to the bit by changing its magnetization state. To keep up with the ever-rising tide of data production, a significant amount of research and development has gone into increasing hard drive storage density. Comparing the areal density of current hard drive technology to that of the original hard drive (the IBM 350), one sees an increase by a factor of over five hundred million, from 2 kilobytes per square inch in 1956 to over 1 terabyte per square inch now [3], illustrated in Figure 1-1. This increase in density has been accompanied by a significant decrease in price. From 1957 to 2018, the price of hard drives decreased from 9,200,000 to 0.019 dollars/gigabyte. While this appears

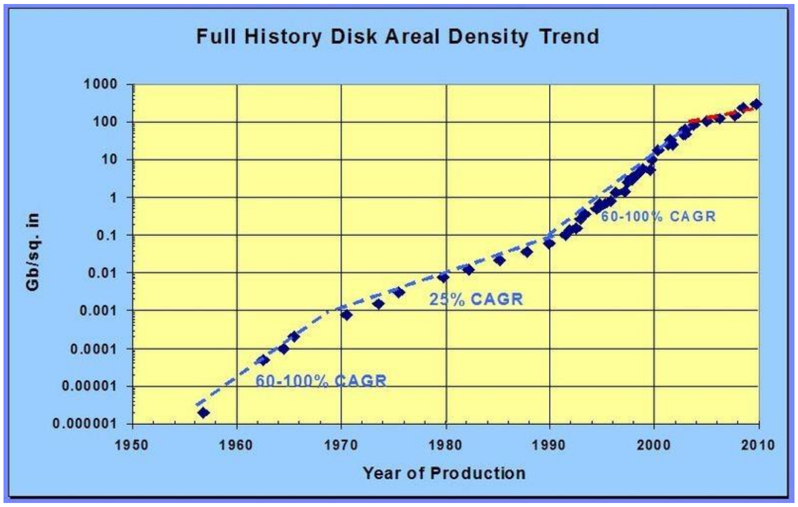

Figure 1-1. Hard drive areal density over time [1].

beneficial for the massive server farms that store our data, as device storage density increases, so too does the power density required to run them. Data centers use an enormous amount of power, roughly 3% of all the electricity used worldwide [4].

In addition to the long-term storage provided by hard drives, faster forms of memory known as static RAM (SRAM) and dynamic RAM (DRAM) are used to enable fast access to data during computation. These forms of storage use transistors and capacitors rather than magnetic bits to store information and exhibit read and write times on the order of nanoseconds. But while static and dynamic RAMs are fast, they cannot compete with the storage density provided by hard drives, and they are volatile, meaning that when power is turned off, all currently stored data is lost. This makes existing RAM undesirable in terms of device size and energy efficiency. This is where MRAM comes into play. MRAM has access speeds comparable to SRAM and DRAM technologies, can achieve high density, and is non-volatile, meaning that no data is lost in the absence of power [1].

In this section, important advancements in the field of magnetic memory will be discussed and the current state of ongoing research in the field will be reviewed. Finally, areas in which the current state-of-the-art could be improved will be addressed. Magnetic memory has undeniable benefits, whether it be the ultra-high storage density in hard drives, or the high speed and non-volatility of MRAM, but its electric current-based read and write methods waste a significant amount of energy through Joule heating. It is paramount that the rate of improvement in magnetic memory matches the pace of data production, as the sheer amount of data being produced shows no signs of slowing.

a. Perpendicular Magnetic Anisotropy

Historically, many of the improvements in the field of magnetic recording and storage have been spurred by the need to increase storage density. In 1991, the ring-shaped magnetic read head that had been used in magnetic recording since 1933 was replaced by a magnetoresistive read head, as shrinking head sizes pushed the ring-shaped head to its sensitivity limit [5]. MRAM exhibits a similar trend. Until recently, the bulk of MRAM research utilized the easily manufactured in-plane (IP) magnetic tunnel junction (MTJ), in which the storage layer exhibits IP anisotropy. However, the ever-increasing storage densities required in modern memory systems promise to render IP MTJs obsolete. As the size of an IP magnetic memory bit decreases, so too does its thermal stability [6]. This trend has driven a significant research effort to develop an MRAM system that utilizes storage layers with perpendicular magnetic anisotropy (PMA). Magnetic films with PMA exhibit large anisotropy which results in higher thermal stability at reduced dimensions [6]. This phenomenon was first observed in single-atomic-layer NiFe, in which the PMA is attributed to surface anisotropy effects [7]. Subsequent efforts to develop magnetic films with PMA focused on producing out-of-plane (OOP) magnetization in systems that could be more easily fabricated for industrial application (i.e. integrated into perpendicular-MTJ (pMTJ) structures). This requires a material system that simultaneously exhibits PMA and large tunnel magnetoresistance (TMR), a necessity for readout. Counterintuitively, both of these requirements were satisfied by a material system initially used in IP MTJs. In 2008, a large TMR value of 604% was observed in a CoFeB/MgO/CoFeB layer structure [8]. The CoFeB in this structure had thicknesses varying from 2 – 6 nm and exhibited IP anisotropy. Only two years later, it was observed that in CoFeB – MgO bilayers, the direction of CoFeB's anisotropy switches from IP to OOP as its thickness is reduced to ~1 nm [9]. These two factors make CoFeB and MgO ideal for producing high density magnetic memory bits. Indeed, later that year, a pMTJ with CoFeB magnetic layers and MgO tunneling barrier was fabricated, shown in Figure 1-2, demonstrating the capability to produce high-density, high-TMR magnetic memory bits [10].

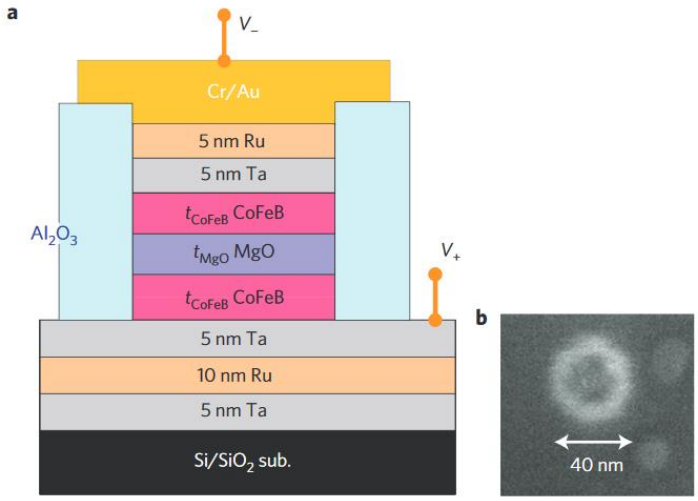

Figure 1-2. a) Schematic of the standard CoFeB MTJ layer structure used for both IP and pMTJs. b) Top view of MTJ pillar highlighting small dimension (40 nm) of pMTJ [10].

b. Writing Methods

While PMA does enable increased density in magnetic memory systems, one of the central benefits of MRAM over traditional CMOS-based memory is energy efficiency. MRAM promises non-volatility, meaning that no energy is required to maintain the state of the memory bit. While this does guarantee lower energy consumption than non-volatile systems, it also means that the efficiency of the MRAM system is entirely dependent on the read and write methods used in that system. At the large scale, a coil of wire is used for both processes. The state of a magnet is read by measuring the magnetic flux through a coil, and one can generate a strong magnetic field by passing an electric current through a coil. These are the same principles used in the early days of magnetic recording at the small scale. In early memory systems, read and write heads consisted of a small coil of wire wrapped around a soft magnetic material. The state of each magnetic domain was read by measuring its associated magnetic flux, and by passing a current through the coil, one could change the state of each magnetic bit [11].

However, as the dimensions of magnetic memory systems have decreased, these read and write methods can no longer be used. The sensitivity of the read head at small dimensions is limited, and the energy consumption of the writing process becomes untenable, as more and more energy is wasted through Joule heating. On the read-side, this dilemma was first solved through the use of anisotropic magnetoresistance (AMR), followed by giant magnetoresistance and TMR [5]. Rather than measuring magnetic flux, these methods rely on electrical resistance changes caused by changes in magnetization to identify the state of the memory bit. On the write-side, this issue was resolved by utilizing spin-polarized current, rather than traditional unpolarized electric current. This method, known as spin transfer torque (STT), was first predicted theoretically in 1996, with lower critical switching currents than those in the older coil-based read head [12]. Passing electric current through a FM layer produces a spin-polarized current with spins aligned along the FM layer's magnetization direction. If this spin-polarized current is then passed through a second, thin FM layer, it switches the magnetization of that layer, aligning it with the polarization of the current. This mechanism is illustrated in Figure 1-3 [13]. Following its theoretical treatment, this method was effectively demonstrated by switching the magnetization of thin film cobalt in a Co/Cu/Co stack [14], with critical switching current matching that predicted in [12]. In the years since, STT has received significant research attention as the go-to write method for MRAM, including its integration and optimization in CoFeB – MgO pMTJs [15]. But while STT does provide improvements over the use of a magnetic field-based write method, it comes with its own drawbacks. To use STT to switch an MTJ, the current must be applied vertically, directly through the stack structure. This exposes the thin dielectric layer to a relatively large electric field, leading to dielectric breakdown and shortening the life of the STT MRAM system [16]. This is a difficult issue to address, as the electric field experienced by the dielectric layer is proportional to the switching barrier exhibited by the MTJ, and a large switching barrier is necessary to ensure adequate thermal stability.

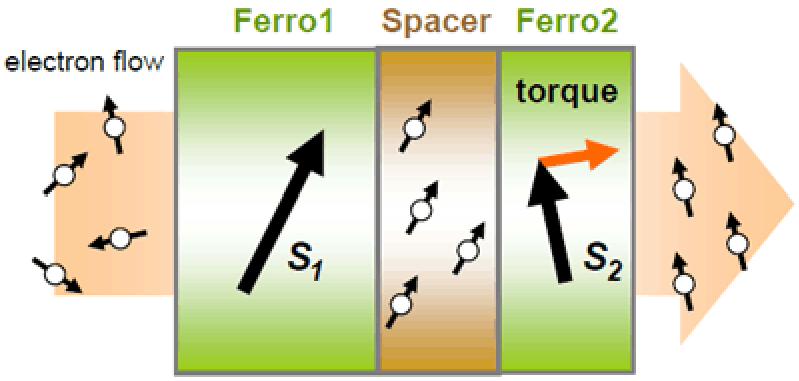

Figure 1-3. A diagram showing the torque associated with a spin-polarized current passing through a ferromagnet.

This issue of degradation in STT MRAM has been addressed in recent years using an unrelated spin current phenomenon known as the spin hall effect (SHE). Discovered in 1971, this effect describes the behavior of an unpolarized electrical current being driven through a metal with strong spin orbit coupling. Due to this spin orbit coupling, electrons with opposite spins experience opposite, transverse forces within the metal, resulting in an accumulation of polarized spins at the metal's edges [17], [18], illustrated in Figure 1-4. It was not until many years later that this phenomenon was used to manipulate the magnetization of a magnetic layer. In 2010, it was shown that electrical current in platinum produced spin waves in an adjacent $Y_3Fe_5O_{12}$ layer, a magnetic insulator. These spin waves were then detected on the other side of the $Y_3Fe_5O_{12}$ layer as a voltage in a second Pt layer [19], demonstrating the ability to both generate and detect spin waves using the SHE.

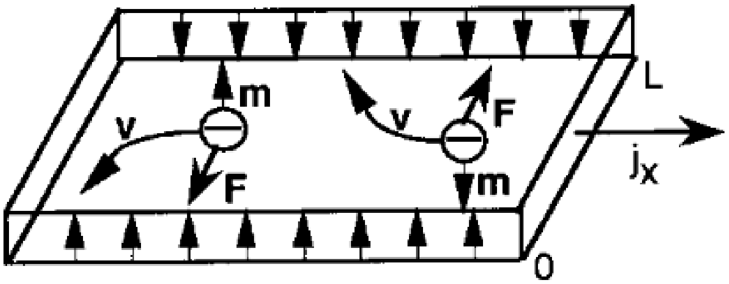

Figure 1-4. A diagram showing the trajectory of electrons with opposite spin due to the spin hall effect [18].

Shortly after, this effect was used to deterministically switch magnetic films with PMA in the presence of a small magnetic field aligned parallel to the applied electric current [20], [21]. The current density used in these studies is competitive with that used in STT switching, and could be further decreased using materials with a stronger SHE [20], [22]. The mechanism behind this method of switching relies on the transfer of torque from the accumulated polarized spins at the edge of the metal layer to the adjacent spins in the magnetic layer, aligning them.

Now termed spin orbit torque (SOT), this method avoids the endurance issue present in STT as the current passes underneath the magnetic stack, rather than directly through it. The only drawback present in these SOT switching studies is the necessity for an external magnetic field. In both [20] and [21], deterministic switching only occurred in the presence of a small magnetic field colinear to the applied current. This magnetic field is necessary is to break the OOP symmetry in the device. The torques applied by SOT are purely IP, meaning that once the SOT current is removed the magnetization has no preference between positive or negative OOP states. This requirement severely limits the applicability of SOT; producing external magnetic fields at the nanoscale is thoroughly avoided due to Joule heating and fabrication complications. For SOT to take the place of STT in industrial applications, a method of OOP symmetry breaking in the absence of an external field is needed.

c. Symmetry Breaking

Since the realization of SOT-based PMA switching, many methods have been investigated to break the OOP symmetry and enable field-free SOT switching. These efforts typically fall into two categories, the integration of additional structures or layers to produce an effective IP field replacing the applied field, or the introduction of lateral structural asymmetries. Rather than applying an external magnetic field IP, it has been demonstrated that introducing an antiferromagnetic (AFM) layer adjacent to the FM storage layer produces a uniaxial exchange bias field, which enables deterministic PMA switching [23], [24]. Similarly, it has been shown that adding an additional IP magnetized FM layer on top of the existing PMA stack, shown in Figure 1-5a, produces a large enough IP stray field to enable deterministic switching [25]. However, these solutions require adding additional layers into the memory stack that must be initialized into particular magnetization states, complicating fabrication. On the other hand, deterministic PMA switching enabled by the introduction of lateral asymmetries has also been demonstrated in various systems, without the need to add new layers into the stack. Using a carefully controlled ion milling process, a Ta/CoFeB/MgO stack was designed with a wedge at one end which produced a tilted anisotropy, leading to deterministic switching [26]. While this fabrication process may be too complex to integrate into industry-wide fabrication, simpler methods of producing wedge shaped layers have been utilized to similar effect. Deterministic switching has been demonstrated in stacks containing either a wedge-shaped oxide layer [27], or wedge-shaped magnetic layer [28], shown in Figure 1-5b. These wedge shaped structures can be produced via sputter deposition. The symmetry breaking that enables PMA switching in these cases is attributed to an oxidation gradient in the magnetic layer which produces an additional OOP effective field.

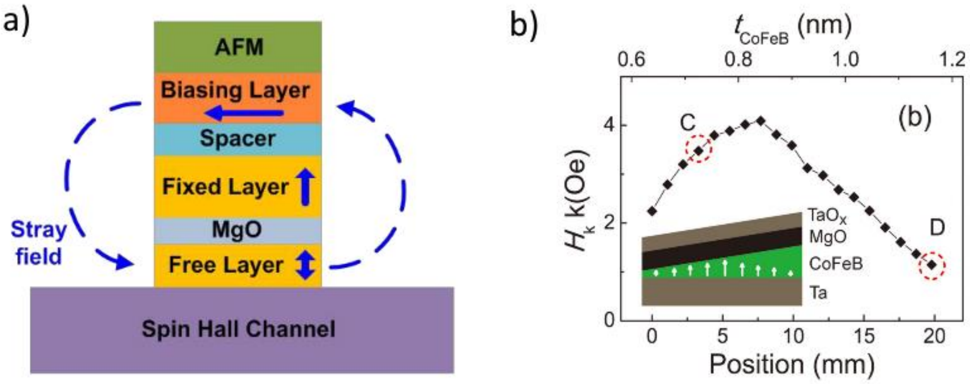

Figure 1-5. (a) shows the layer structure of a pMTJ that achieves field-free switching via the stray field of an additional biased ferromagnetic layer [25]. (b) plots the anisotropy field of CoFeB as a function of thickness. The gradient of oxidation in this structure allows field-free switching [28].

Very recently, deterministic switching in an even simpler system, without the need for an additional permanently magnetized layer or a structural asymmetry has been observed. In three material systems, Ta/[Gd$_x$(FeCo)$_{1-x}$]$_6$, Ta/CoFeB (wedge)/MgO, and Ta/CoFeB/CoFe/MgO, the presence of intrinsic asymmetric exchange breaks OOP symmetry and enables deterministic switching [29]. In the latter case, only two adjacent magnetic layers with no structural asymmetry are needed, a material system which could be integrated into existing MTJ technology [29].

d. Dzyaloshinskii – Moriya Interaction

Asymmetric exchange, or the Dzyaloshinskii – Moriya interaction (DMI), refers to an interaction between two adjacent magnetic spins which energetically favors canting of the spins relative to each other, as opposed to the traditional exchange interaction which prefers parallel or antiparallel alignment. This interaction was first identified in the mid-twentieth century [30], [31] as an explanation for weak ferromagnetism observed in some AFM materials. In AFM α-Fe_3O_3, $MnCO_3$, and $CoCO_3$, DMI induces canting of the magnetic spins from their perfectly antiparallel alignment. This slight canting means that the opposing magnetic moments no longer fully cancel out, leading to a small net moment in the material. An example of a spin structure stabilized by DMI is illustrated in Figure 1-6.

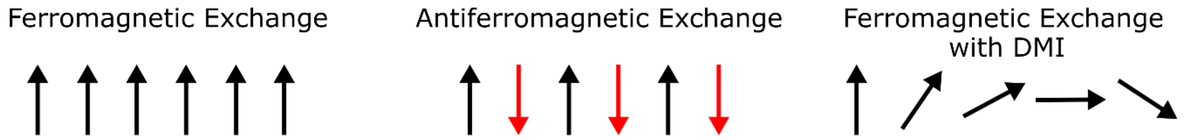

Figure 1-6. A diagram showing typical ferromagnetic and antiferromagnetic spin states, and a spin state corresponding to ferromagnetic exchange with a contribution from DMI that favors spin canting.

Although DMI was discovered several decades ago, its utilization in magnetic systems has begun only recently. Interest in DMI was recently revitalized due to its role in stabilizing skyrmions, a topological magnetic spin structure characterized by locally whirling spins. First observed in certain single crystal magnetic compounds [32], [33], skyrmions have now been observed in several different material systems that possess strong spin-orbit coupling and broken inversion symmetry [34]. One such system, consisting of a thin FM layer deposited on top of a heavy metal (such as platinum or tantalum), has been shown to exhibit strong interfacial DMI and has recently been utilized in various spintronic applications [35], [36]. It is this heavy metal/magnet heterostructure that is utilized for DMI-mediated field-free PMA switching.

To break OOP symmetry with DMI, two properties are needed. Of course, the material system must possess DMI, but in addition to that it must also exhibit some gradient in magnetic properties. The structures used in [29], $Ta/[Gd_x(FeCo)_{1-x}]_6$, Ta/CoFeB (wedge)/MgO, and Ta/CoFeB/CoFe/MgO, each exhibit both of these properties. For ferrimagnetic $Gd_x(FeCo)_{1-x}$ and ferromagnetic CoFeB, their interfaces with tantalum induce positive interfacial DMI coefficients D_{ij} of 15.2 $\mu J\ m^{-2}$ and 54.0 $\mu J\ m^{-2}$, respectively [29], [37]. In the case of $Gd_x(FeCo)_{1-x}$, the compositions of Gd and FeCo can be varied across the lateral dimension of the device, creating a gradient in saturation magnetization. In the cases utilizing a CoFeB magnetic layer, two options for creating a magnetic gradient are explored. First, by depositing the CoFeB in a wedge shape, the gradient in thickness creates a gradient in perpendicular anisotropy throughout the lateral dimension of the device. The second option involves stacking thin film CoFeB and CoFe to create an OOP gradient in saturation magnetization, an even simpler scheme that could easily be integrated into industrial manufacturing. These magnetic gradients are necessary because without them, DMI alone would provide no preference between positive or negative OOP states. This concept is explained by the switching process outlined in Figure 1-7. The applied SOT current aligns the magnetization with its spin polarization IP, then the SOT current is removed. In the absence of DMI and magnetic gradients, the magnetization can rotate from IP to either positive or negative OOP states with no preference between them. With DMI and no gradient, the result is the same. The sign of the DMI coefficient determines which chirality of spin canting is energetically preferred, clockwise (positive D_{ij}) or counterclockwise (negative D_{ij}), but this chirality can still be satisfied by switching in either direction. Only when both DMI and a magnetic gradient are present is switching from IP to a particular OOP state (either positive or negative) preferred. This is because the gradient causes different regions of the device to respond the PMA differently. For example, in the case with a gradient in PMA (wedged CoFeB), the region where the PMA is greater will return to the OOP direction first, and the preferred chirality governed by D_{ij} will determine which direction it will switch.

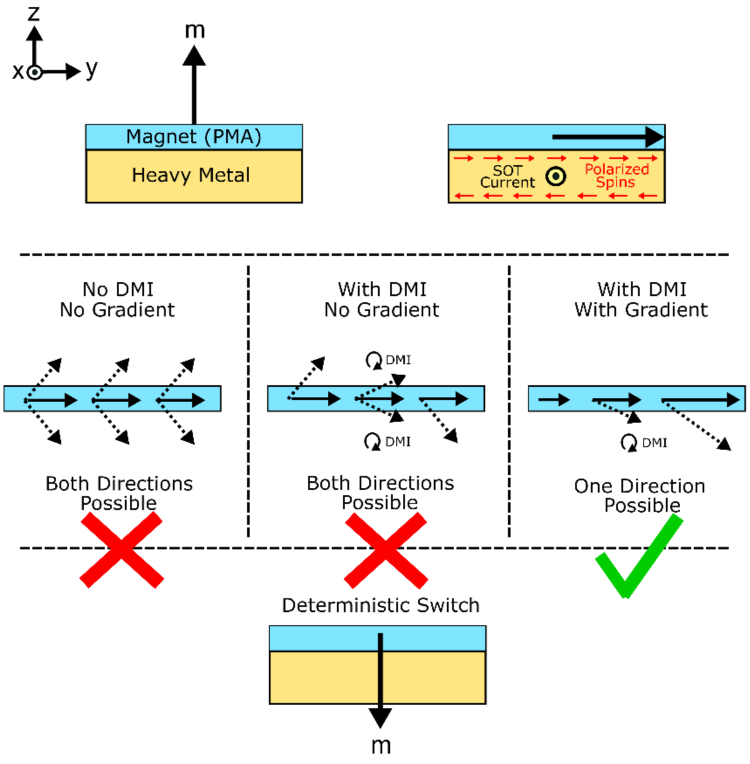

Figure 1-7. A diagram showing the switching process associated with field-free DMI-mediated switching. Only with DMI and a magnetic gradient is deterministic switching possible.

While this method does represent an extremely promising method of field-free PMA switching, its efficiency is intrinsically limited by its writing method. SOT relies on using electric current at the nanoscale, meaning that significant energy will still be wasted due to Joule heating. In the following section, a concept which promises ultra-efficient magnetization control via voltage, rather than current, will be discussed.

e. Multiferroics

Despite all of the significant advancements in the field of magnetic recording, including the advent of STT pMTJs, and field free SOT switching, we are still tied to electric current-based read and write methods decades after the coil-based read and write heads were abandoned. While we have engineered methods of magnetization control that improve upon the efficiency of an external magnetic field, the continued reliance on electric current means that device efficiency will still be limited by Joule heating, especially as the size of memory bits continue to decrease. A method of controlling the magnetization in a small memory bit that does not rely on electric current is needed.

One such method that has gained popularity in recent years is the use of multiferroics. In a multiferroic system, one can change the magnetization in a magnetostrictive material by applying a voltage to an adjacent piezoelectric material. The strain induced in the piezoelectric layer is transferred to the magnetostrictive layer, thereby inducing a change in its magnetization in the absence of any magnetic field or electric current [38]. In recent years, research on this field has steadily increased with progress on multiferroic solutions in a wide variety of applications, including antennas [39], micro-motors [40], cell sorting [41], and magnetic memory [42]–[45]. Following experimental demonstrations of magnetization control in various continuous-film piezoelectric/magnetostrictive heterostructures [42]–[44], electric field-induced 90º IP rotation of the magnetization in single-domain Ni ellipses was demonstrated in 2013 [45]. This was significant as it moved the field of magnetoelectric magnetization control a step closer to controlling individual magnetic bits, a necessary step if this method is to take the place of traditional current-based write methods. But for a magnetoelectric write method to become more attractive than traditional methods, it must be able to deterministically switch magnetic elements with PMA.

Several efforts have been made to develop a magnetoelectric PMA switching scheme, but these works generally utilize voltage to supplement other switching mechanisms. In 2017, deterministic switching of a CoNiCo ferromagnet was achieved by applying voltage to a PMN-PT substrate [46]. The device was similar to the magnetic/piezoelectric heterostructures used in multiferroic magnetization control, but the switching does not occur via voltage-induced strain. The applied voltage poles the piezoelectric layer prior to switching, then the electric field generated by the piezoelectric creates a lateral imbalance in SOT spin density, meaning that this method still fully relies on electric current. In 2018, deterministic switching in a PMN-PT/Ta/CoFeB stack was achieved numerically by applying both SOT and voltage-induced strain at a 45° angle to each other [47], but in this case, the strain was utilized only as a mechanism of symmetry breaking. In a few cases, strain from a piezoelectric layer has been used to lower the energy barrier for switching in magnetostrictive elements, with 30% reduction in coercive field [48] and 1-2 orders of magnitude reduction in switching energy dissipation [49], [50], but these methods are still reliant on spin torque from electric current.

There have been a few cases in which switching of a magnetic element with PMA in the complete absence of electric current has been demonstrated [51]–[53], but these take advantage of the magnetization’s precessional motion and require accurate timing of the applied voltage pulse (~1-10 ns) which is not ideal for commercial application. An example of this switching mechanism is shown in Figure 1-8. That said, these methods do highlight the efficiency afforded by purely magnetoelectric switching. In [51], a Terfenol-D nanodot was switched using only 22 aJ of energy, far superior to the ~ 100 fJ associated with current-based methods [1].

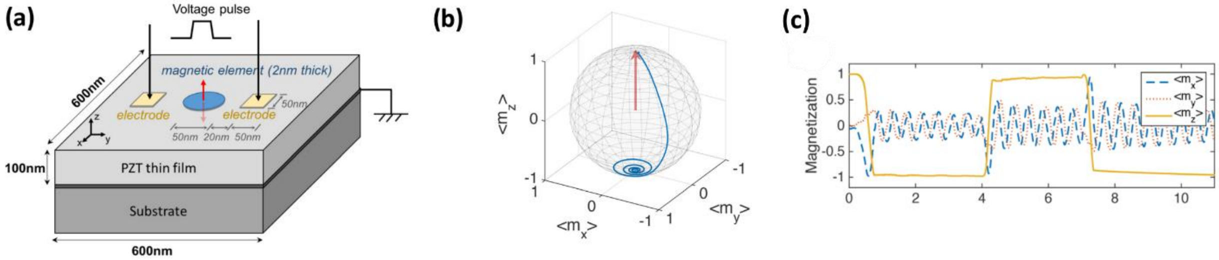

Figure 1-8. (a) A schematic showing the device structure in which 180 degree precessional switching of CoFeB was modeled. (b) The spin trajectory associated with OOP precessional switching. (c) A plot of magnetization over time, highlighting repeatable OOP switching using only strain pulses.

Achieving deterministic PMA switching using only strain is challenging due to the uniaxial IP nature of the strain-induced anisotropy. Like SOT, the effective field due to strain in a magnetostrictive element acts IP, with no preferential OOP component. Like PMA, the strain-induced effective field in multiferroic heterostructures is uniaxial, providing only a preferential IP axis, but not a preferential direction. This symmetry must be broken to enable strain-mediated PMA switching. Utilizing novel magnetic phenomena like interfacial DMI may represent a path towards pure strain-mediated PMA switching.

f. Antiferromagnetics

So far, this article has focused on the large storage density (via PMA) and the energy efficiency (via non-volatility and magnetoelectric writing capabilities) provided by MRAM. Another important factor to consider is MRAM’s access speed. In current computer architectures, the speed at which operations can be completed depends strongly on the read and write times associated with the device’s logic gates and RAM. If an operation requires information stored in RAM, the processor must wait for the signal to travel to that memory address, read the state of the bit, and travel back to the processor before the operation can be initiated. Similarly, if an operation results in new information that must be stored, the processor must wait for the signal’s travel time to and from the memory bit, plus the time associated with writing to that bit, before another operation can start. In current architectures, these access times for SRAM and DRAM are on the order of ~1 ns and 20-30 ns, respectively. Processors are conducting billions of operations each second and any extra nanoseconds add up, minimizing the access time associated with computer memory is essential to addressing the ever-growing need for improved performance.

For MRAM, read and write times are on the order of ~1 ns, faster than DRAM and comparable with SRAM [1]. These are the time periods associated with writing to the bit via spin polarized current and reading its state via magnetoresistance. In the writing process, for example, polarized spins exert a torque on the FM comprising the MTJ’s storage layer, switching its magnetization from one direction to another. The speed at which this can occur is determined by a phenomenon known as ferromagnetic resonance (FMR). If a FM material is placed in an external magnetic field, the field exerts a torque on the magnetization causing it to precess around the direction of the applied field. The frequency of this precession is known as the Larmor frequency and depends on the strength of the applied field [54]. In 1946, it was observed that if the applied field is oscillating at high frequency, matching the Larmor frequency, resonance occurs and the oscillating field loses energy to the precessing magnetization [55]. The resonant frequency for a thin-film ferromagnetic material is given by [56]:

$$\omega_0 = \gamma(BH_0)^{\frac{1}{2}}$$

where γ is the gyromagnetic ratio, B is the magnetic induction in the material, and H_0 is the applied static magnetic field. This resonant frequency sets the speed limit at which the magnetization can respond to an impulse, whether it be an external field, spin torque, or strain anisotropy. For ferromagnetic materials, FMR is on the order of 1-10 GHz. CoFeB, for example, has a FMR value of ~5 GHz [57]. These resonance values limit the temporal response of ferromagnetic materials to no faster than ~100 ps.

Antiferromagnetic materials provide a route to increasing this resonant speed limit. A basic example of the ordering of AFM spins is shown in Figure 1-6. Discovered by Louis Néel in 1948 [58], this type of magnetic ordering is defined by oppositely oriented magnetic moments in adjacent atoms. In this alignment, the magnetic moments cancel each other out, resulting in zero stray field and no demagnetization (shape anisotropy) effects. In addition to that, the strong antiferromagnetic exchange coupling between adjacent spins means that extremely large magnetic fields (>1 T) are needed to manipulate AFM states. These characteristics led Néel himself to state that AFMs, while interesting, are useless. Shortly after Néel's discovery, Kittel developed a theory for AFM resonance (AFMR) like that described for FMR above. The resonant frequency in AFM materials is given by [59]:

$$\omega = \gamma\left(H_0 \pm [H_A(2H_E + H_A)]^{\frac{1}{2}}\right)$$

where H_0 is the static magnetic field, H_A is the anisotropy field, and H_E is the exchange field. Given typical values for anisotropy and exchange fields in AFMs, this model predicts AFMR frequencies on the order of terahertz, three orders of magnitude higher than FMR. Subsequent experimental efforts confirmed AFMR values of 261.4 GHz and 1.11 THz in MnF_2 and NiO, respectively [60], [61], and demonstrated magnetization reorientation in under 5 picoseconds in AFM $TmFeO_3$ [62]. These works prove that AFM devices can operate significantly faster than

FM-based devices. This speed, combined with the lack of stray field and invulnerability to external fields, make AFM devices very attractive for magnetic memory applications.

After the initial discovery of AFM ordering, interest in studying AFMs diminished as the external fields required to control them were untenably large (>1 T) and alternative methods of control had not been found. For this reason, until the early twenty-first century, AFM materials were used almost exclusively to pin the fixed layer in MTJ stacks [63]–[65]. In 2007, however, experiments demonstrated that STT can alter the exchange bias of a FM/AFM bilayer [66], [67], evidence that torque from spin-polarized currents can manipulate spins in AFMs. About ten years later, control of AFM states via Néel spin-orbit torque was achieved in CuMnAs [68]. Néel spin-orbit torque takes advantage of the spin-orbit coupling in AFM materials to induce effective fields on each sublattice via electric current.

As this progress was being made on developing electrical control methods for AFMs, work was also being done on integrating AFM free layers into MTJ structures. For AFM memories to work, they must be able to produce a large enough TMR value for readout. In 2011, a spin valve-like structure comprised of Pt/MgO/IrMn/NiFe/Ta was used to create an AFM memory bit. The NiFe layer enabled switching of the AFM state via exchange-spring effect, and a 100% tunneling anisotropic magnetoresistance (TAMR) value was recorded at low temperature (4 K) [69]. Soon after in 2014, a room temperature AFM memory device using FeRh was developed. In this device, the AFM state was switched by raising the temperature until a FM state was created, then applying a large external field in the desired direction as the temperature cooled back down, shown in Figure 1-9. Using this method, stable high-resistance and low-resistance states were observed at room temperature [70]. While the use of an external field and temperature control is not ideal on-chip applications, achieving discernable high and low-resistance states does represent an important step on the path towards room temperature AFM MTJs.

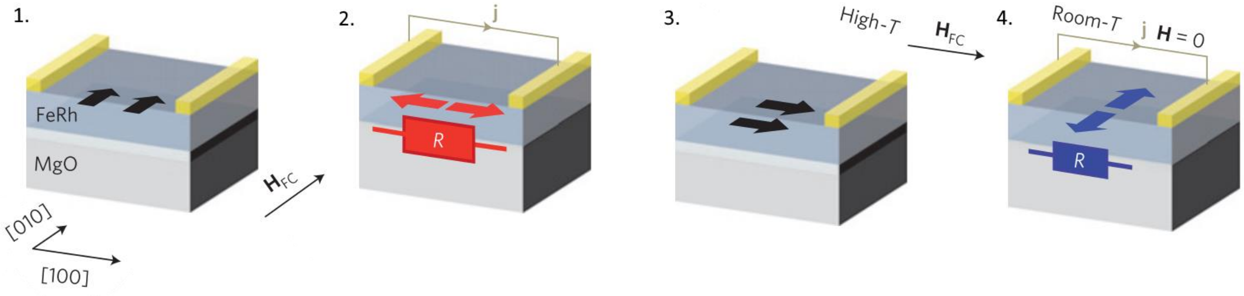

Figure 1-9. A diagram showing the switching process for the heat-assisted magnetic field switched AFM MTJ. At high temperatures, a field aligns the spins while they are in a FM state. Upon cooling down, a particular AFM state is deterministically achieved.

In addition to electrical control of AFMs, a good deal of research has gone into developing multiferroic methods to control AFM states. If realized, a multiferroic AFM memory bit would represent a significant improvement over current technology, with extremely fast and energy efficient writing. Theoretical evidence of the potential to switch AFM states via strain was first provided in 2010, when it was suggested using first-principles calculations that strains under 1% could reorient the Néel vector in bimetallic AFMs such as Mn_2Au and MnIr [71]. Again in 2016, an theoretical investigation of possible structural configurations at a $Mn_2Au/BaTiO_3$ interface provided evidence for strain-control of Mn_2Au spins via piezo-generated strain [72]. Finally, one year later, strain control of AFM domains was demonstrated. By comparing x-ray magnetic linear dichroism (XMLD) measurements of a Mn_2Au thin film under the influence of both a 70 T applied field, and a 0.1% tensile strain, evidence for domain orientation via strain was observed [73]. These works, along with several others showing modulation of AFM spins via applied strain [74]–[77], convincingly demonstrate the ability to control states in AFM materials using strain generated in adjacent ferroelastic layers.

Very recently, a MTJ structure comprised of PMN-PT/MnPt (AFM)/$MgAl_2O_4$/Pt exhibited a non-volatile MR ratio of 8.7% using piezo-induced strain to control the AFM layer [78]. This device is shown in Figure 1-10. While this MR ratio is low, and this MTJ did not demonstrate the desired THz speed afforded by AFM materials, it does represent an extremely important step towards creating an all-AFM memory bit. The MR ratio exhibited by AFM MTJs is likely to increase with studies on material choice, and THz switching using patterned electrodes has already been demonstrated numerically [79]. With further progress on these fronts, the development of an ultra-efficient, ultra-fast magnetic memory is inevitable.

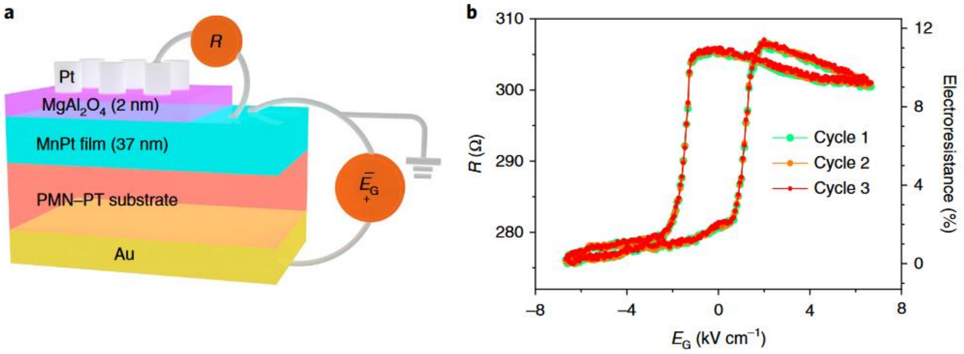

Figure 1-10. (a) A schematic of the AFM MTJ with switching induced by piezostrain. (b) The resistance loop corresponding to the high and low-resistance states achievable in the pictured MTJ.

g. Magnetic Memory: Summary

Just as the goal of increasing magnetic storage density led to the adoption of a magnetoresistive read head over the original ring-shaped head, so too did this goal lead to the adoption of PMA as the primary mechanism of storage in MRAM devices. PMA allows device sizes to be reduced while maintaining thermal stability, and since its discovery, has been the focus of an intense research effort. Initially, the goal of this research was to integrate PMA into MTJ structures such that it could be switched via STT. This goal soon changed as it was discovered that the STT current used for switching leads to breakdowns in the MTJ’s tunnel barrier. It was this drawback that shifted the focus onto SOT. SOT allows one to control the magnetization of a magnetic element without passing current through it, eliminating STT's endurance issue, and improving upon STT's energy efficiency. That said, SOT requires a method of symmetry breaking in order to switch elements with PMA, and this requirement can greatly complicate fabrication processes, as either an external magnetic field, additional layers, or structural gradients must be incorporated into the device. Furthermore, both STT and SOT still depend on electric current, meaning that their efficiencies are limited by Joule heating. The field of multiferroics offers a solution to this issue by providing magnetization control via electric field, rather than current. Extremely energy efficient magnetization switching has been demonstrated using multiferroics, but to this day, deterministic PMA switching using purely electric field has not been achieved. Furthermore, the speed of current MRAM devices are limited by the storage layer's FMR. The field of magnetic memory is extremely promising, but improvements in both energy efficiency and speed could be made by utilizing novel magnetic properties that have only recently found application in the memory space, such as DMI and AFMR.

1.2 Non-Boolean Computing

Non-boolean computing refers to computing paradigms that utilize devices and processes that fall outside traditional von Neumann, CMOS-based computing architectures. Some examples of non-boolean computing models include neural networks [80]–[82], cellular automata [83], various non-CMOS implementations of logic circuits [84], [85], and energy-minimizing processors [86]. While the applications and operational principles of these cases are diverse, there are a few central tenets that set non-boolean (NB) computing architectures apart from their sequential, transistor-based counterparts. Parallelism is essential to the function of many NB architectures. Von Neumann (VN) architectures operate in a step-by-step manner, executing a given set of instructions. This type of processing has served us well to date, but now with applications in systems like self-driving cars and artificial intelligence, we are asking our computers to perform tasks like pattern recognition and image processing. These types of tasks would be very power and memory-intensive to implement using VN architectures [81]. NB architectures are designed to work in parallel, executing multiple operations on multiple inputs at the same time. Another concept that is integral in the field of NB computing is analog behavior. VN architectures are based on transistors which are inherently digital (on or off, true or false, 0 or 1). This may work well for storing data and performing arithmetic, but problems like image processing require much more sophistication. Many images, and problems in general, are not black and white, meaning that a device designed to work with a spectrum of signals is required to analyze and solve these problems.

Magnetism possesses several beneficial properties that make it an ideal tool in NB computing applications. In a phenomenon known as dipole coupling, FM elements produce a stray field that couples their response to other nearby FM elements. This property has been utilized in various neural nets and nanomagnet-based processors [80], [81], [86] to couple different nanomagnetic elements and achieve parallelism. As the computation progresses, each coupling between a nanomagnet and each of its neighbors represents an operation, all of which are being executed simultaneously. Furthermore, magnetic devices can easily be utilized to achieve analog behavior. While the previous section focused on the binary, non-volatile behavior of magnetic memory, the potential to use non-binary magnetic behavior has also been demonstrated in stochastic STT-based MTJs [82], and by varying the dimensions and shape of nanomagnetic elements, multiple states (beyond 0 and 1) can be engineered [87]. These properties make magnetism a promising candidate for widespread application in NB computing platforms. In this section, two areas in the field of NB computing, computer vision and neuromorphic synapses, will be focused on. Research in these areas is in a relatively early phase, and magnetism represents a useful tool in moving these areas forward.

a. Magnetic Energy Minimizing Co-Processor

Computer vision is a growing field in which the goal is development of computational platforms that can “understand” images, meaning that they can take an image as input, and extract useful data from that image. One aspect of this is object recognition, being able to identify an object that is present in an image. In this process, there are typically three steps, shown in Figure 1-11: feature extraction, in which salient aspects of the image (i.e. edges, colors, etc.) are found, perceptual organization, in which features that are related to each other are grouped, and object matching, in which the grouped features are matched to an object stored in memory. For humans, this process happens in an instant with no effort on our part. For computers, on the other hand, achieving object recognition is more challenging. A significant amount of research has gone into each step of the process [88]–[91], but currently, the perceptual organization step still occurs via software or traditional boolean computing. Here, an approach to perceptual organization using a nanomagnetic

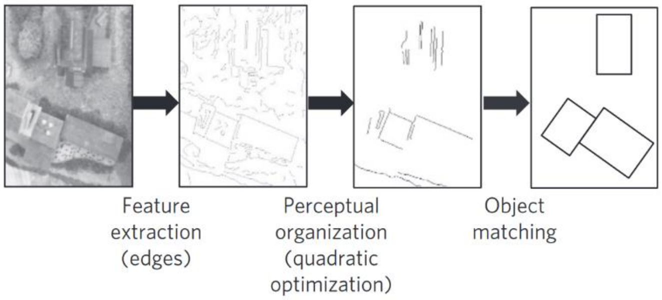

Figure 1-11. The steps associated with object recognition: feature extraction, perceptual organization, and object matching.

computational platform is discussed. This method is beneficial over boolean implementations as it computes solutions directly through a single

energy minimization process, regardless of problem size. Increasing problem size in boolean implementations, on the other hand, would mean concurrently increasing the number of computational iterations [86].

Proposed in 2015, the magnetic energy minimizing co-processor (MEMCoP) is designed to perform the task of perceptual organization via energy minimization in an array of nanomagnetic disks [86]. First, the important features in the image are extracted. In this case, the MEMCoP focuses on edges. Given a set of edges, an affinity function that takes into account edge location, angle, length, and other factors calculates the affinity between each edge. Then, through a quadratic optimization process, the grouping of edges that produces the maximum total affinity is found. This grouping of edges is then compared to an object database in the final, object matching step. The MEMCoP performs the edge grouping stage by analyzing the ground states of nanomagnetic disks under the influence of dipole coupling from identical nearby disks.

b. Ground States

A given magnetic element can exist in a number of different magnetic states, each corresponding to a certain configuration of the element’s magnetic spins. The state that the element exists in is determined by the energies associated with the following magnetic phenomena: the exchange interaction, E_{ex}, the demagnetization field, E_{demag}, magnetocrystalline anisotropy (MCA), E_{MCA}, and Zeeman energy due to an external applied magnetic field, E_Z. The sum of each of these energies is the magnetic element's total energy, E_T, and an element's ground state is defined as the state that results in the smallest total energy. In the case of the MEMCoP, amorphous (as opposed to single-crystal) elements are used, making the MCA energy contribution negligible, and no external fields are applied, meaning we can ignore the E_Z term. This means that our element's ground state is determined by minimizing the sum of E_{ex} and E_{demag}. In FMs, the exchange interaction works to align spins so that they are parallel to each other. When all the spins in an element are parallel, E_{ex} is minimized. Demagnetization (demag) energy, on the other hand, depends on the shape of the magnetic element, and is the origin of shape anisotropy. If a magnet is magnetized along a certain axis, there exists a demag field inside the magnet directed in the opposite direction to the magnetization, shown by $\vec{H}$ in Figure 1-12. This field arises from uncompensated spins at the edges of the magnet. Each spin is a magnetic dipole with a north and south pole. Within the magnet, one north pole is compensated, or canceled out, by the south pole of a nearest neighbor spin. At the edges of the magnet, there are no more neighboring spins to compensate these poles. At one end, there will be uncompensated north poles and at the other, uncompensated south poles. These uncompensated north and south poles form their own magnetic dipole and generate the demag field in a direction opposite to the direction of the magnetization.

The demag energy in a magnetic element is proportional to this demag field. This field opposes the current magnetization state, so demag energy is minimized in a magnetization state that minimizes the demag field. In order to do this, the number of uncompensated spins at the edges of the magnet must be minimized. This occurs via the formation of magnetic domains, regions in a magnetic material in which each spin is parallel. For a magnetic element of any shape, there exists a magnetic domain structure which eliminates uncompensated spins at its edges.

The states minimizing demag energy and minimzing exchange energy are not the same. The formation of domains to minimize demag energy produces domain walls where spins are no longer parallel, increasing exchange energy. The states favored by exchange energy and demag energy are shown in Figure 1-13. Which of these states is the element's ground state is determined by which energy makes a bigger contribution to the total energy, and therefore produces the smallest total energy when minimized. The magnitudes of the exchange and demag energies are determined by the magnet's size. Exchange is a short-range interaction, and at small

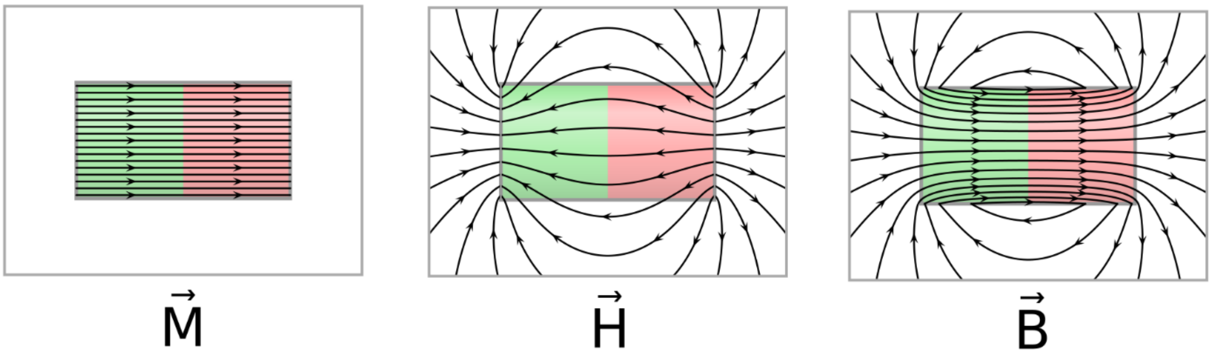

Figure 1-12. A diagram illustrating the direction of the demag field produced in a uniformly magnetized magnetic element.

sizes, exchange dominates. As magnets get larger, more surface area exists for uncompensated spins and demag begins to dominate [92].

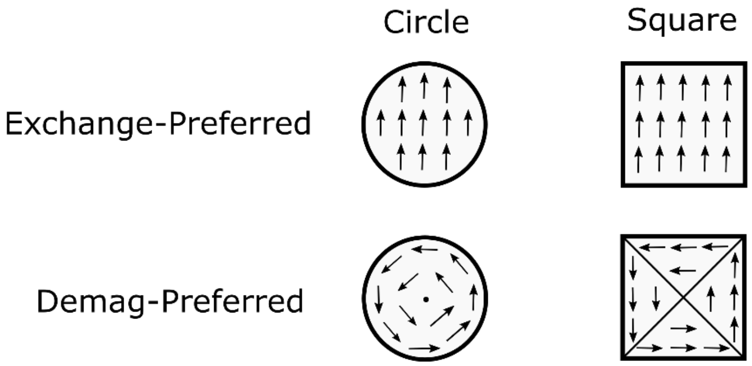

Figure 1-13. The magnetization states preferred by exchange energy and demagnetization energy for circular and square nanomagnets.

c. Dipole Coupling

The previous section explained how the ground state of a single, isolated nanomagnetic element is determined. When these elements are placed in close proximity to one another, they begin to interact with each other through dipole coupling. This coupling refers to the effect that one element's stray field has on another adjacent element. When a magnet is uniformly magnetized in a certain direction, it produces a stray field in the air surrounding it. An example of a stray field $\vec{B}$ corresponding to a uniformly magnetized element is shown in Figure 1-12. This stray field works to align the magnetizations of nearby nanomagnets with itself, influencing their ground state. When nanomagnets are placed in close proximity, they influence each other in this

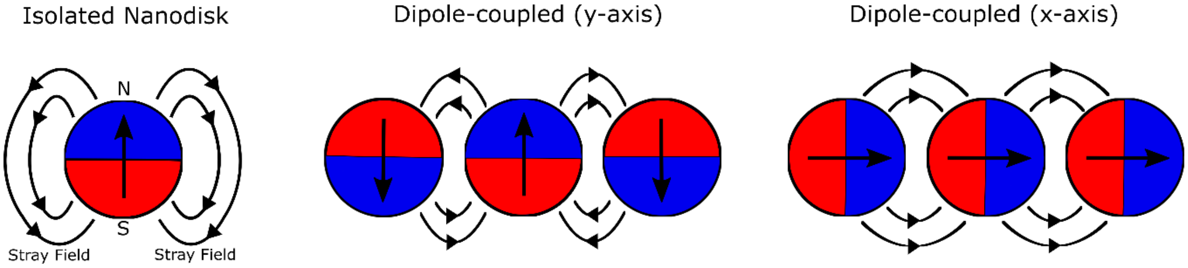

Figure 1-14. The stray field associated with an isolated, single-domain nanodisk, and two stable configurations of a three disk, dipole-coupled system.

way and are considered dipole-coupled. Figure 1-14 illustrates the stray field associated with an isolated magnetic nanodisk in a single-domain state, along with two stable magnetization configurations for a three-disk, dipole-coupled system.

Along with exchange and demag energy, dipole coupling influences the ground state of a nanomagnetic element. As the spacing between magnetic elements decreases, the strength of the dipole coupling between them increases. This effect was demonstrated both numerically and experimentally in 2013, when it was shown that as the spacing between two permalloy nanodisks decreases, the ground state switches from a vortex state (demag-preferred) to a single-domain in-plane state (exchange and dipole preferred), shown in Figure 1-15 [93]. The MEMCoP utilizes the interplay between these three phenomena, exchange, demag, and dipole coupling, to conduct the perceptual organization step of computer vision.

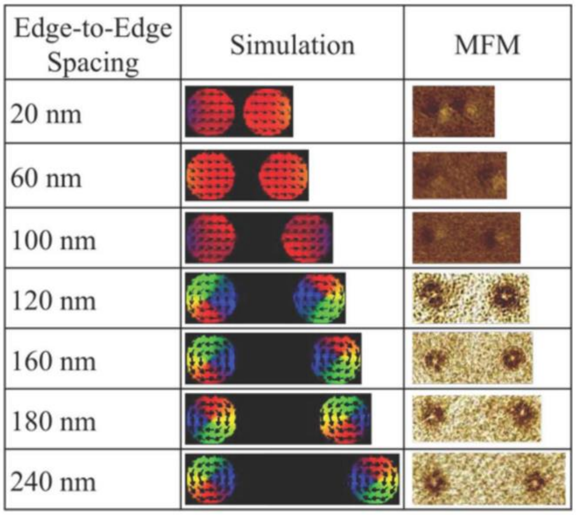

Figure 1-15. The dependence of nanodisk ground state on disk spacing in a two-disk system.

d. Energy Minimization

To calculate the affinity between a given set of edges, a magnetic Hamiltonian formula to calculate the coupling strength between set of magnetic nanodisks was developed. This function is of similar form to the previously discussed affinity function, but instead of measuring the affinity between two edges based on edge location and angle, this function calculates the strength of the coupling between two nanodisks as a function of the spacing between them. By exploiting the similarity between these two functions, a specific arrangement of nanodisks representing the given set of edges can be produced, in which each nanodisk corresponds to one of the edges in the given set. Then, to perform the computation, an external magnetic field first switches every nanodisk to their hard axis (in this case, the z-axis) in a procedure known as clocking. Following clocking, the magnetic field is removed and the system is allowed to relax to its minimum energy state. By analyzing the resulting ground states of the disks, the important edges of the provided image can be extracted. The edges corresponding to disks in single-domain states (i.e. strongly dipole-coupled) are kept, while the edges corresponding to disks in vortex states (weakly dipole-coupled) are discarded. Thus, the MEMCoP conducts the perceptual organization step of computer vision.

While the accuracy of this method has been demonstrated [86], it is extremely inefficient to fabricate a new, customized array of nanodisks for each image that the MEMCoP will analyze. To remedy this, a uniform 2D array of nanodisks that can be programmed on an image-by-image basis can be used. Once the Hamiltonian function determines the necessary magnetic layout, the corresponding disks in the uniform array will be activated (termed “computing” disks) and the remaining disks will remain inactive (or “non-computing”). The array is clocked, and the states of the computing disks are analyzed, then the array is re-programmed for the next image. For this to work, a method of ensuring that the non-computing disks do not interfere with the calculation is required. These disks must be held in a state such that their stray field does not influence the relaxation of the computing disks. One method which could be used to accomplish this in a selective, disk-by-disk way is SOT. Already discussed in the context of magnetic memory, SOT represents a method of magnetization control that has benefits in energy efficiency over both an external magnetic field and STT [94], [95], and can be selectively applied on a disk-by-disk basis. There are two applications in which SOT has been utilized in conjunction with dipole coupling previously, as a method of implementing phase-locked spin-torque nano oscillators [96], and as a method of clocking in Bennett clocking architectures [97]. While both applications creatively utilize both SOT and dipole coupling, both focus only on SOT's steady state behavior and only consider the dipole coupling between two elements. Further study is needed to understand the interaction between spin orbit torques and dipole coupling in large nanomagnet arrays.

e. Antiferromagnetic Neuromorphic Synapses

The MEMCoP is designed specifically to solve quadratic optimization problems, like those present in the perceptual organization step of computer vision. This section will now focus on another sub-field of NB computing known as neuromorphic computing. This field attempts to develop computational platforms that imitate the function of a biological brain. The reason for doing this is to enable computers to solve problems like learning, pattern recognition, speech recognition, and classification. For humans and other animals, these tasks come naturally, but for traditional computers they are very challenging. The difference lies in the structure of the brain. Brains are comprised of many neurons, small cells that transmit electrical signals to one another, and synapses, the junctions between these neurons. This design allows for an extreme level of parallelism when solving problems. Additionally, the brain has a property known as plasticity, in which physical changes occur in the brain as a person learns and adapts, making certain neural pathways better transmitters than others. In the field of neuromorphic computing, or neural networks, this plasticity is achieved via synaptic weighting.

The goal of a synapse within a neural network is to provide weighting of signals, thereby increasing the influence of some signals over others. This could be achieved on the software-side, by using algorithms to monitor weights, but hardware implementations of neural networks have been shown to have benefits over software in both speed and cost, as hardware implementations typically reduce the number of iterations required in a certain operation, and reduce the number of electronic components needed [98]. Over time, various hardware implementations of synapses have been developed, including the storage of weights on floating gate transistors [99], and capacitors [100], and the use of nonlinear MOSFETs [101]. These approaches are not ideal, as the capacitors are inherently volatile, and the use of transistors at small scales guarantees degraded efficiency through Joule heating and leakage current.

Recently, a class of devices known as memristors have gained a significant amount of research attention for synaptic weighting applications. These are devices whose resistance can be altered in some way, and through this change in resistance, the current or voltage signal passing through it can be weighted. Memristors can take various forms, whether it be a Si pillar within a dielectric whose resistance is dependent on the formation of conductive filaments [102], a titanium oxide bilayer whose conductance increases or decreases depending on the voltage applied to it [103], or most recently, a STT MTJ, in which the inherently stochastic nature of switching under different magnitudes of electric current is utilized [104]. In each case, the effective electrical resistance of the device is altered depending on the current passing through it, exactly the behavior that is required for synaptic weighting. But while these memristive devices are promising, these implementations are each dependent on electric current to modify the state of the device, which wastes a significant amount of energy. Additionally in the case of the stochastic STT MTJ, the speed is limited by the device’s FMR. Antiferromagnetic materials represent a solution to both of these issues. As previously discussed, AFMs have resonance values on the order of THz, meaning that their states can be altered at ultra-high speeds. Additionally, multiferroic control of AFM states has been demonstrated, meaning that an AFM device could be switched between various resistance states in an extremely energy efficient manner. In recent years, AFMs have almost solely been studied in the memory space, but these characteristics make AFMs very promising for synaptic applications in neuromorphic computing.

1.3 Micromagnetic Modeling

It is extremely useful to be able to test hypotheses numerically prior to experimental testing, saving both the time and money associated with fabrication. Numerical models can provide useful information while designing a device and can serve as a proof of concept for a new idea. When it comes to modeling micromagnetic systems like those discussed above, modeling efforts typically focus on simulating a magnetic material’s dynamic response to various anisotropies or fields, whether they be in the form of a simple external magnetic field, or a more complex voltage-induced strain. This section focuses on describing the fundamentals of micromagnetic modeling and some of the important work done using these models.

a. Landau-Lifshitz-Gilbert Equations

Micromagnetic modeling consists of simulating the temporal response of a magnetic moment, $\boldsymbol{m}$**,** to an effective magnetic field, $\boldsymbol{H_{eff}}$. This is done by solving an equation known as the Landau-Lifshitz-Gilbert (LLG) equation, shown here:

$$\frac{\partial \boldsymbol{m}}{\partial t} = -\mu_0 \gamma\left(\boldsymbol{m} \times \boldsymbol{H_{eff}}\right) + \alpha\left(\boldsymbol{m} \times \frac{\partial \boldsymbol{m}}{\partial t}\right)$$

where $\boldsymbol{m}$ is the normalized magnetization, $\boldsymbol{H_{eff}}$ is the effective magnetic field, μ_0 is the vacuum permeability, γ is the gyromagnetic ratio, and α is the Gilbert damping factor. This equation consists of two torques, a field-like torque represented by the $\boldsymbol{m} \times \boldsymbol{H_{eff}}$ term and a damping-like torque represented by the $\boldsymbol{m} \times \frac{\partial \boldsymbol{m}}{\partial t}$ term. The field-like torque is orthogonal to both $\boldsymbol{m}$ and $\boldsymbol{H_{eff}}$, and results in the precession of the magnetic moment around the effective field. The damping-like torque is orthogonal to both $\boldsymbol{m}$ and the direction of the moment's motion $\frac{\partial \boldsymbol{m}}{\partial t}$, and gradually aligns the magnetic moment with the effective field. The trajectory induced by each of these torques is illustrated in Figure 1-16.

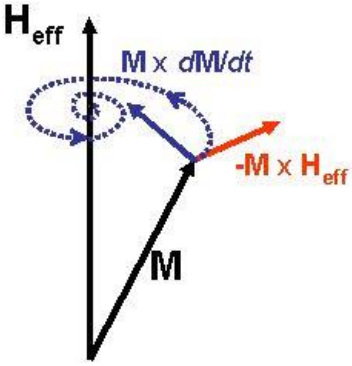

Figure 1-16. The direction of the two LLG torques on the magnetic moment.

b. Effective Field

The term $\boldsymbol{H_{eff}}$ in the LLG equation encompasses all of the driving forces that influence the behavior of a magnetic moment, and is typically represented as:

$$\boldsymbol{H_{eff}} = \boldsymbol{H_{ex}} + \boldsymbol{H_{demag}} + \boldsymbol{H_{MCA}} + \boldsymbol{H_{ext}} + \boldsymbol{H_{ME}}$$

where each term represents the exchange field, demagnetization field, magnetocrystalline anisotropy field, external applied field, and magnetoelastic field, respectively. The exchange field is represented by:

$$\boldsymbol{H_{ex}} = -\frac{1}{\mu_0 M_s}\frac{\partial E_{ex}}{\partial \boldsymbol{m}}$$

where M_s is the material's saturation magnetization, and E_{ex} is exchange energy, defined by:

$$E_{ex} = A_{ex}(\nabla \boldsymbol{m})^2$$

where A_{ex} is the exchange stiffness. Thus, the characteristics of $\boldsymbol{H_{ex}}$ are determined by the saturation magnetization and exchange stiffness of the chosen material.

The demagnetization field is represented by:

$$\boldsymbol{H_{demag}} = -\nabla\phi$$

where ϕ is the magnetic potential, such that $\nabla^2\phi = M_s \boldsymbol{\nabla} \times \mathbf{m}$. This term takes into account both the internal demagnetization effects in a magnetic element and the magnetostatic interaction between discrete magnetic elements. The demagnetization effects within a single element are determined by the shape of the element, as quantified by the demagnetization factor N_d. The role of this term is seen in the demagnetization energy:

$$E_{demag} = -\frac{1}{2}\mu_0 M_s^2 N_d$$

The demagnetization factor quantifies a magnet's resistance to being magnetized along each principle axis.

The effective field due to magnetocrystalline anisotropy is defined by:

$$\boldsymbol{H_{MCA}} = -\frac{1}{\mu_0 M_s}\frac{\partial E_{mca}}{\partial \boldsymbol{m}}$$

with the MCA energy E_{MCA} being defined by:

$$E_{MCA} = K_0 + K_1(m_1^2 m_2^2 + m_2^2 m_3^3 + m_3^2 m_1^2) + K_2(m_1^2 m_2^2 m_3^3) + \cdots$$

where K_i (i = 0, 1, 2, …) are anisotropy constants that are material-dependent, and m_i (i = 1, 2, 3) are the components of the magnetization along each anisotropy axis. In single-crystal samples, $\boldsymbol{H_{MCA}}$ can be significant, but in amorphous or polycrystalline samples, $\boldsymbol{H_{MCA}}$ is assumed to be negligible.

Finally, the magnetoelastic field, which accounts for the magnetic response to external stresses in magnetostrictive materials, is defined by:

$$\boldsymbol{H_{ME}} = -\frac{1}{\mu_0 M_s}\frac{\partial E_{ME}}{\partial \boldsymbol{m}}$$

with the magnetoelastic energy defined by:

$$E_{ME} = B_1\left[\epsilon_{xx}\left(m_x^2 - \frac{1}{3}\right) + \epsilon_{yy}\left(m_y^2 - \frac{1}{3}\right) + \epsilon_{zz}\left(m_z^2 - \frac{1}{3}\right)\right] \\ + 2B_2\left(\epsilon_{xy} m_x m_y + \epsilon_{yz} m_y m_z + \epsilon_{zx} m_z m_x\right)$$

where B_1 and B_2 are the first and second order magnetoelastic coupling coefficients, m_x, m_y, and m_z are the x, y, and z components of the magnetization, respectively, and ϵ_i (i = xx, yy, zz, xy, yz, zx) are the components of the strain tensor. B_1 and B_2 depend on the materials young's modulus E, and saturation magnetostriction λ_s. In some cases, when the strain in an element can be considered uniform, the effective magnetoelastic field is represented by a simple uniaxial effective field, defined by:

$$\boldsymbol{H_{ME}} = \frac{3\lambda_s E \boldsymbol{\epsilon}}{M_s}$$

where $\boldsymbol{\epsilon}$ is the applied strain. The energy associated with this uniaxial effective field is:

$$E_u = K_u \sin^2(\theta)$$

where K_u is the uniaxial anisotropy constant defined by $K_u = \frac{3}{2}\lambda_s E\epsilon$. Other uniaxial anisotropies, like PMA, are represented in the same way with material-dependent K_u values.

c. Spin-Orbit Torque

It is also important to represent the effects of spin polarized current on a magnetic moment when simulating SOT devices. The torque on the magnetization due to a spin polarized current is represented as an additional term added onto the above-mentioned LLG equation. This torque is defined by:

$$\tau_{SOT} = \frac{j_c \hbar \theta_{\mathrm{SH}}}{2eM_s t}\left[\left(\boldsymbol{m} \times (\hat{\boldsymbol{\sigma}} \times \boldsymbol{m})\right) - \beta(\boldsymbol{m} \times \hat{\boldsymbol{\sigma}})\right]$$

where j_c is the electrical current passing through the heavy metal layer, $\hbar$ is the reduced Planck's constant, θ_{SH} is the spin hall angle, e is the elementary charge, d is the thickness of the magnetic layer, β is a constant quantifying the relative magnitude difference between field-like ($\boldsymbol{m} \times \hat{\boldsymbol{\sigma}}$) and damping-like ($\boldsymbol{m} \times (\hat{\boldsymbol{\sigma}} \times \boldsymbol{m})$) torques, and $\hat{\boldsymbol{\sigma}}$ is the direction in which the spins are polarized. The spin hall angle quantifies the amount of spin current generated from the electrical current j_c via the spin hall effect. Therefore heavy metals with larger spin hall angles produce larger torques for the same applied SOT current.

d. Accuracy

The LLG equation represents the basis of micromagnetic modeling and can be solved with varying levels of accuracy. The most basic of these is the single-spin model. In this case, the system being modeling is treated as a single magnetic moment. This means that the exchange interaction is ignored, and any demagnetization effects are represented by uniform anisotropies. Similarly, any strain-induced effective fields are treated as uniform, uniaxial anisotropies. The central benefit of this method is its speed, as it can provide approximations of magnetic behavior in a matter of seconds. In 2012, this model was used to simulate extremely energy efficient magnetization switching in a multiferroic nanomagnet [105].

While the macrospin model is extremely fast, it is limited to single-domains and therefore cannot represent complex domain structures, like vortex states or domain walls, or incoherent magnetization dynamics. For cases that require more sophistication, modeling frameworks exist that solve the LLG equation over a mesh, or a series of cells. Each cell is assumed to be a single spin, and if the cell size is made smaller than the material's exchange length (usually ~3-5 nm), these frameworks can accurately simulate magnetic domain behavior. Recently, this type of model has been used to simulate the effects of voltage-induced strain on dipole-coupled nanomagnets [106], [107].

In models that solve only the LLG equation, like those described above, magnetoelastic effects are assumed to be uniform throughout the magnetic layer. This can lead to inaccuracies when modeling multiferroic heterostructures, as this assumption is not always true [108]. In magnetostrictive materials, non-uniform strain distributions can noticeably influence the magnetic response. To address this, a model was developed in 2014 that not only solves the LLG equation, but couples it with the partial differential equations governing elastodynamics and electrostatics, solving all three simultaneously in a fully-coupled manner [108]. This model allows one to simulate all aspects of multiferroic heterostructures, including the electrodes and piezoelectric substrate as well as the magnetic element. In 2018, this model was expanded to enable simulation of antiferromagnetic materials by adding a second magnetic sublattice, and coupling each sublattice via an antiferromagnetic exchange term [79]. Using this fully-coupled model, extremely accurate simulations of multiferroic devices in various fields have been conducted [41], [47], [51], [79], [109].

1.4 Summary

The more we know about magnetism, the better we can leverage it to solve our problems. The compass has evolved from a large metal spoon into a microscopic electronic device. The space needed to store one bit of information in the 1950s now fits 62.5 kilobytes. These developments can only be attributed to the study of magnetism and our continued discovery and understanding of its various properties. In this work, novel magnetic properties are used to develop improvements in the energy efficiency and speed of magnetic devices that fall into two categories: MRAM, and NB computational platforms.

Right now, the goal in the field of MRAM is to achieve external magnetic field-free deterministic switching in magnetic bits with PMA. SOT currently represents the most promising method to achieve this because it enables electrical magnetization control without passing a current directly through the MTJ stack. That said, SOT requires a method of symmetry breaking in order to switch elements with PMA, and this requirement can greatly complicate fabrication processes, as either an external magnetic field, additional layers, or structural gradients must be incorporated into the device. Recently, a simpler method of symmetry breaking, interfacial DMI, has been utilized to achieve deterministic PMA switching using SOT [29]. This represents a significant step towards developing a high-density MRAM, but the reliance on SOT puts a limit on device efficiency. Extremely efficient magnetization switching has been demonstrated using voltage in multiferroics, but as of now, deterministic PMA switching using purely voltage has not been achieved in a system fit for industrial manufacture. Here, the potential to achieve voltage-mediated PMA switching in magnetic elements with PMA is investigated.

In the field of non-boolean computing, magnetism has received a significant amount of research attention because it can provide parallelism and analog behavior, two pillars of this field that set it apart from traditional CMOS-based computing. In fact, magnetism has already been implemented in the core functionality of various NB computing architectures. The MEMCoP relies on the dipole coupling within an array of magnetic nanodisks to perform the perceptual organization step of computer vision. In neural net architectures, STT MTJs have been implemented to enable synaptic weighting. In both cases, improvements in the architecture can be realized by leveraging magnetic properties that have not yet seen application in these fields. The interaction between SOT and dipole coupling in large magnetic arrays is not well understood but represents a path toward solving the problem of programmability in the MEMCoP. Furthermore, it is known that AFM materials can be efficiently controlled in the picosecond-regime, but this benefit has yet to be utilized for synaptic weighting. In this work, these concepts will be investigated with the goal of moving the field of NB computing a step closer to maturity.

2 Magnetization Dynamics in a Dipole-Coupled Array

This chapter focuses on numerical modeling conducted to support the development of the magnet-based non-boolean computing platform MEMCoP [86], which specializes in quadratic optimization problems such as those associated with computer vision. While this platform is still in early stages of development, the work presented here addresses the crucial challenge of nanoscale magnetic array programmability faced by the MEMCoP, by improving our understanding of the interaction between dipole coupling and SOT within an array of nanoscale magnetic elements.

2.1 Nanomagnetic Array Programmability

Recent efforts in the field of spintronic devices have demonstrated a wide range of nanomagnetic computing architectures based on spin physics, with some examples being associative computing by spin torque nano-oscillator (STNO) [80], [81], spiking neural network by magnetic tunnel junction (MTJs) [82], majority gate logic by magnetic quantum-dot cellular automata (MQCA) [83] magnetic energy minimizing co-processor (MEMCoP) [86] by coupled nanomagnets, and probabilistic spin logic (PSL) [84] by low energy barrier nanomagnets. To achieve high density and avoid the complications of physical interconnects, many of these architectures rely on dipole coupling between nanomagnets to perform logic operations [110]. It has been demonstrated in previous works that the main roadblocks to developing dipole-coupled Boolean computing frameworks lie in the need for a directional clocking mechanism and the presence of defects. In the case of MQCA, the lack of an effective clocking mechanism and the presence of defects can inhibit or altogether stop the flow of information through the logic network [110]. The MEMCoP framework represents a promising alternative to this type of directional system, in which computation is driven through the collective interaction of neighboring nanomagnets with no directional flow of information. Additionally, each MEMCoP cell has an integrated access transistor, meaning it can be accessed, clocked, and read separately, removing the bottleneck of clocking seen in other dipole coupling-based frameworks. Regarding the impact of defects, there are no driver cells in the MEMCoP architecture, and each cell interacts with at most 8 neighboring cells in *N x N* fashion, meaning the impact of defects is not significant and does not limit read-distinguishability [111][112].

Bhanja *et al.* experimentally demonstrated that MEMCoP can solve computationally expensive quadratic optimization problems, like those that arise in computer vision applications. MEMCoP solves these problems by mapping energy functions onto a grid of dipole-coupled nanomagnets. The relaxation physics governing the behavior of the nanomagnets follow a similar quadratic form to that of the optimization problem, such that the solution to the optimization problem is represented by two possible ground states in the dipole-coupled array: an in-plane single domain state (representing a ‘1’) or a vortex domain state (representing a ‘0’). A detailed explanation can be found in the original paper [86]. Recent advances of this co-processor have resolved challenges of readability [2], but a limitation related to programmability remains. Currently, the co-processor requires fabrication of a specific magnetic layout tailored to each new optimization problem. To achieve parallelism in the layout, and to allow for repeated uses of this hardware in different applications, a programmable 2D grid of nanomagnets is needed.

Programming different magnetic layouts into this 2D grid requires the capability to select which nanomagnets will participate in the computation process (computing elements) and which will not (non-computing elements). The computing elements in the array will interact with each other through dipole coupling, while the non-computing elements must not influence this interaction [86]. A selective method to control the magnetization and switch between computing and non-computing states is needed to achieve a programmable array. One approach is to use spin-orbit torque (SOT), a current-based method of magnetization control discussed in depth in earlier sections. SOT can be used to target individual nanomagnetic elements within the array while simultaneously providing the previously discussed benefits in energy efficiency and endurance over external Oersted field and STT. As a simple, low energy method of magnetization control, SOT has received a great deal of research attention in the field of magnetic memory and logic. Deterministic switching of magnetic bits using SOT has been achieved experimentally in various systems [113], [26], [114], and SOT has been used to counterbalance damping in spin torque nano-oscillators [115]. Dipole coupling between adjacent nanomagnets has also been utilized in conjunction with SOT previously, however, these applications focused on SOT mediated bennet clocking [97] rather than programmable computational arrays. Lastly, almost all previous SOT applications focus on the steady-state magnetic response to SOT current rather than the dynamic response of dipole-coupled magnetic elements. Therefore, studies are needed to better understand the behavior of nanomagnets dynamically excited by SOT in the presence of dipole coupling fields.

In this work, we investigate selective switching of nanomagnetic elements in a dipole-coupled array from computing to non-computing states using SOT-induced magnetic dynamics. A dipole-coupled array of nanomagnets is characterized, and the dynamic response of these nanomagnets to an applied SOT current with varying ramp rates is analyzed, with the goal of achieving programmability of individual elements within the array.

2.2 Simulation Setup

In this work, a micromagnetic finite-difference model is used to simulate circular magnetic nanodisks under the influence of both SOT and dipole coupling. The material modeled is pseudo-amorphous CoFeB, in which the exchange length (3-4 nm) is larger than the as-deposited grain size [51], [116]. As such, it is assumed that the exchange interaction overrides the magnetocrystalline anisotropy (MCA) yielding a magnetic element without significant long-range MCA. Additionally, the absence of an external magnetic field is assumed and thermal noise is neglected. Circular nanodisks are focused on to avoid any shape anisotropy effects. The micromagnetic model is represented by the Landau Lifshitz Gilbert (LLG) equations with an SOT term added:

$$\frac{\partial \boldsymbol{m}}{\partial t} = -\mu_0\gamma\left(\boldsymbol{m}\times\boldsymbol{H_{eff}}\right) + \alpha\left(\boldsymbol{m}\times\frac{\partial \boldsymbol{m}}{\partial t}\right) + \frac{j_c\hbar\theta_{\mathrm{SH}}}{2eM_sd}\left(\boldsymbol{m}\times(\boldsymbol{\hat{\sigma}}\times\boldsymbol{m})\right)$$

as described above in the modeling section (please refer to section 1.3 for term definitions). The field-like component of SOT is neglected in this study as its impact on magnetization dynamics is not well understood [117], and it has been shown to be substantially smaller than the damping-like term in some systems [22]. Additionally, it is assumed that the spin-orbit torque is applied uniformly throughout the thickness of the nanodisk. $\boldsymbol{H_{eff}}$ is the effective field, consisting of the exchange field H_{ex}, and the demagnetization field H_d, obtained by differentiating the total energy density with respect to magnetization. The total energy density is defined as:

$$\epsilon_T = \epsilon_{ex} + \epsilon_d \qquad (2)$$

where

$$\epsilon_{ex} = A_{ex}(\nabla\boldsymbol{m})^{\mathbf{2}} \qquad (3)$$

and

$$\epsilon_d = -\frac{1}{2}\mu_0(M_s\boldsymbol{m}\ \cdot \boldsymbol{H}_d) \qquad (4)$$

Differentiation of the total energy density with respect to magnetization results in:

$$\boldsymbol{H}_{eff} = -\frac{1}{\mu_0 M_s}\frac{\partial \epsilon_{total}}{\partial \boldsymbol{m}} = \boldsymbol{H}_{ex} + \boldsymbol{H}_d \quad (5)$$

where

$$\boldsymbol{H}_{ex} = \frac{2A_{ex}}{\mu_0 M_s}\Delta\boldsymbol{m} \qquad (6)$$

and

$$\boldsymbol{H}_d = -\nabla\phi \qquad (7)$$

such that

$$\nabla^2\phi = M_s\boldsymbol{\nabla}\ \cdot \mathbf{m} \qquad (8)$$

The demagnetization field H_d includes the magnetostatic interaction between discrete magnetic elements and is calculated for each finite difference cell based on the magnetizations and distances between every other cell within the simulation volume [118]. This includes the magnetic interaction between the cells in neighboring magnetic circular nanodisks, and thus includes the dipole interaction between these magnetic nanodisks. The above equations are solved using a commercially available finite-difference solver which utilizes Neumann boundary conditions ($\frac{\partial \boldsymbol{m}}{\partial \hat{\boldsymbol{n}}} = 0$) at the magnetic material's edges [118]. The material used in all studies is pseudo-amorphous CoFeB, with a room temperature exchange stiffness of 2.0 x 10^{11} J/m, saturation magnetization of 1.2 x 10^6 A/m, and a gilbert damping of 0.01.

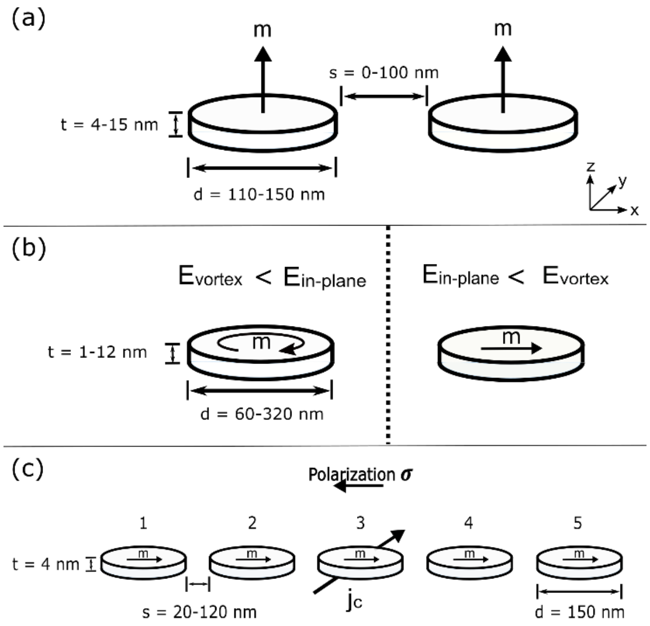

Figure 2-1. The disk dimensions and layouts associated with the following studies.

The first study illustrated in Figure 2-1a evaluates the dipole coupling energy of a pair of neighboring disks as a function of spacing and disk size. Coupling energy is defined as the difference between the total energy of the two-disk system (Figure 2-1a), and the total energy of two isolated disks of the same dimensions and in the same magnetic states. This is mathematically represented as:

$$E_c = E_T^{pair} - 2E_T^{isolated} \qquad (9)$$

where the superscript "pair" denotes the two neighboring disks, "isolated" denotes a single disk, and the total energy E_T is the integral of total energy density (2) over the entire volume. Equation (9) represents the amount of dipole coupling energy between two neighboring disks as a function of the spacing between the disks [93]. In this study, disk diameters are varied from 110 nm to 150 nm, thicknesses from 4 nm to 15 nm, and disk spacings from 0 nm to 100 nm using a finite-difference cell size of 3 x 3 x 1 nm^3.

A second parametric study conducted on isolated disks and a pair of disks spaced 30 nm apart is illustrated in Figure 2-1b. This study is used to determine the dimensions at which the difference between the energy E_T of in-plane single domain states and vortex states is minimized, such that both are potentially stable states [119]. The disk thicknesses are varied from 1 nm to 12 nm and diameters ranged from 60 nm to 320 nm. In these studies, each disk is initialized with an out-of-plane magnetization then allowed to relax for 0.7 ns to determine its stable state.

A third study illustrated in Figure 2-1c is used to determine the critical switching current density of a single disk within an array of disks. In this study, critical current density is defined as the minimum SOT current density required to switch the x-component of magnetization from positive to negative. Three different layouts are simulated, 1) a single isolated disk (i.e. only disk 3), 2) three aligned disks (i.e. only disks 2 – 4), and 3) five aligned disks (i.e. all disks 1 – 5). For the three disk and five disk cases, SOT is applied to only disk 3. Each disk has a diameter of 150 nm, a thickness of 4 nm, and the disk spacing is varied from 20 to 120 nm, dimensions chosen based on the first two studies. A smaller finite-difference cell size of 2 x 2 x 1 nm^3 is used in this study to increase accuracy. Each disk is initialized into an in-plane single domain state pointing in the +x direction, then allowed to relax for 1 ns into a stable state. Once relaxed, a SOT current density ramp with slope 1.67 x 10^8 $\text{A/cm}^2\text{ns}$ is applied to disk 3 until the current density reaches 6.67 x 10^8 A/cm^2. The direction of the polarized spins due to this current is in the negative x-direction, opposite the direction of the effective dipole field as represented in Figure 2-1c. The system is then allowed to relax for 15 ns to reach a stable state while the SOT current density of 6.67 x 10^8 A/cm^2 is held constant. The procedure described above is repeated, and the SOT current density amplitude is increased in intervals of 6.67 x 10^6 A/cm^2 until the critical current density for each disk arrangement is found.

Finally, a study is conducted to evaluate the influence of varying the slope of the SOT current ramp applied to disk 3 of the five disk system (see Figure 2-1c). This study evaluates the magnetic states induced in the second and fourth disks by the SOT current in disk 3 with 20 nm spacing between all nanodisks. The states of the second and fourth disks are quantified by their net magnetization, defined as:

$$Net\ Magnetization = \sqrt{m_x^2 + m_y^2 + m_z^2}_{2nd} + \sqrt{m_x^2 + m_y^2 + m_z^2}_{4th} \quad (10)$$

Each disk is initialized into an in-plane state in the +x direction, then allowed to relax for 0.3 ns. Next, disks 2 and 4 are clocked to the z-direction, while an SOT current density ramp is applied to disk 3. Disks 2 and 4 are then allowed to relax, and once the SOT current density reaches its maximum value, it remains at that value for 5 ns. The slopes of the SOT current ramps used in this study include: {0.67, 1.33, 2.00, 4.00, 5.00, 6.67, 10.00, 20.00, 40.00} x 10^8 A/cm^{2}ns, and the amplitudes of SOT current densities applied include {0.53, 0.60, 0.67, 4.00} x 10^8 A/cm^2.

2.3 Results and Discussion

Figure 2-2a shows a plot of coupling energy E_c (9) as a function of disk spacing for two aligned CoFeB disks of thickness 4 nm, for four different disk diameters from 110 nm to 150 nm. The coupling energy decreases as spacing increases, for all diameters, and approaches zero as spacing increases to 100 nm. At smaller spacings, the effect of disk diameter becomes more apparent as larger diameters result in larger coupling energy. Figure 2-2b shows a plot of E_c as a function of disk thickness for two aligned disks with 30 nm spacing and four different diameters from 110 nm to 150 nm. The coupling energy increases with disk thickness for all diameters, and larger disk diameter results in larger coupling energy. These plots provide information regarding the relationship between dipole coupling energy and disk dimension and spacing that is used in choosing a disk size and spacing for subsequent studies and future computational platforms.

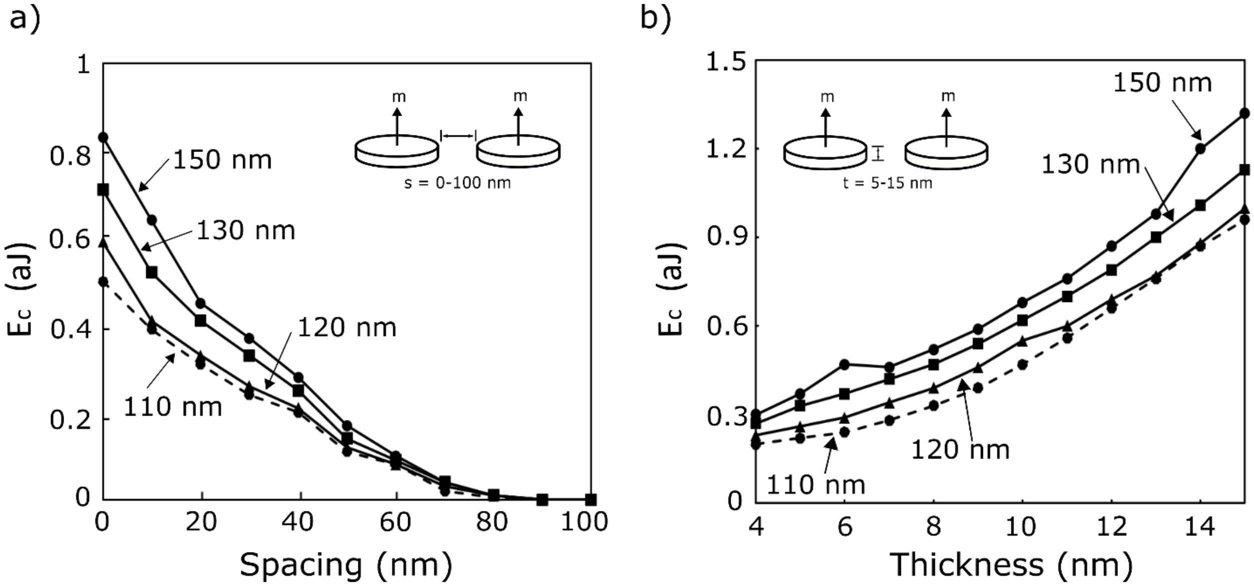

Figure 2-2. CoFeB dipole coupling energy (9) as a function of disk spacing (a) for two aligned disks with a fixed disk thickness of 5 nm, and four different disk diameters; and as a function of disk thickness (b) for two aligned disks spaced 30 nm apart, for four different disk diameters.

Figure 2-3 shows a phase plot for single domain and vortex states as a function of disk diameter and thickness for an isolated disk, as well as two aligned disks spaced 30 nm apart. The solid line represents the phase boundary between single domain and vortex states for the isolated disk, and the dashed line shows the same for the aligned disk pair. The region to the left of these lines is the single domain region, meaning that total energy E_T is minimized for disks in a single domain state, and the region to the right is the vortex region. The phase boundary represents the disk dimensions at which the E_T of a single domain state is approximately equal to the E_T of a vortex state. The phase boundary for the aligned disk pair is shifted to the right when compared to the isolated disk due to the influence of dipole coupling, which increases the stability of the in-plane state. In the MEMCoP device, computing elements that are close to other computing elements (dipole-coupled) are expected to relax into in-plane single domain states, while computing elements that are surrounded by non-computing elements (negligible dipole coupling) are expected to relax into vortex states [119]. To maximize the influence of SOT in the MEMCoP device, disk dimensions along the phase boundary between these states are focused on. Based on the results in Figure 2-2 and Figure 2-3, in subsequent studies we focus on disk diameters of 150 nm and thicknesses of 4 nm. A geometric variation-tolerant study around this dimension reveals that the MEMCoP computing architecture functions properly with variations in diameter and thickness of up to +/- 4 nm and +/- 0.75 nm, respectively.

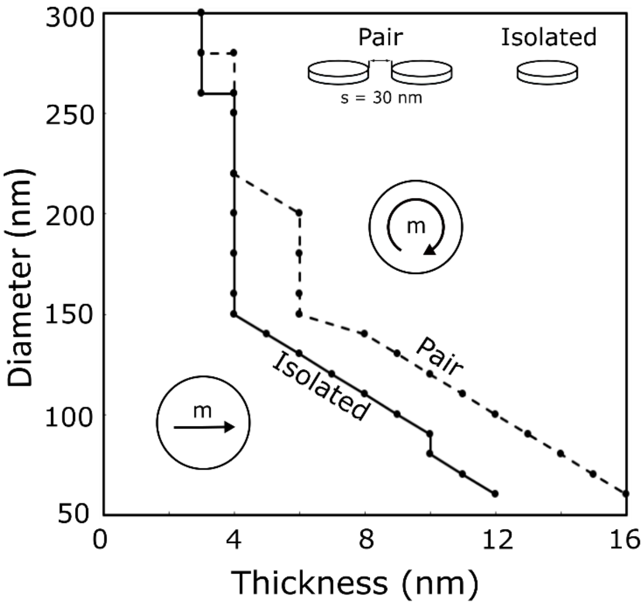

Figure 2-3. The phase boundary between single domain and vortex states as a function of disk diameter and thickness for both an isolated CoFeB disk, and for neighboring CoFeB disks is shown.

Figure 2-4 plots the critical switching current density as a function of disk spacing for a disk in three different arrangements, one isolated disk, three aligned disks, and five aligned disks.

Each disk has a diameter of 150 nm and a thickness of 4 nm with SOT current applied only to the center-most disk in the arrangement (Figure 2-1c). The SOT current ramp is relatively slow to avoid SOT induced magnetization dynamics. For currents below the critical SOT current density threshold, the x-component of disk 3's magnetization remains positive, as it was initialized (see bottom right insert image). Above the critical current density value, the x-component of the magnetization switches to the negative direction as seen in the top right insert image. For both the five-disk and three-disk cases, the critical current density decreases as the disk spacing increases. This is due to the decrease in the dipole coupling energy with increasing disk spacing (Figure 2-2a). The effective dipole field represents an anisotropy keeping disk 3 aligned in the positive x-direction, so the current required to switch it is smaller as spacing increases. These results also show that as disk spacing increases, the five disk and three disk critical current densities approach the isolated disk's critical current density, confirming that the influence of dipole coupling becomes negligible at large disk spacings. The critical switching current density in the five-disk case is larger than in the three-disk case for all disk spacings. This is due to the additional dipole coupling provided by the two end disks in the five-disk system, which, though small, results in a larger effective dipole field. The critical current densities shown here represent the minimum current density required to overcome the effective dipole field for each disk arrangement and spacing. The final study uses this minimum current density to evaluate switching from computing to non-computing states. These results suggest that to produce the largest dipole coupling between the center control disk and the array, a closely spaced five-disk arrangement is needed, and that a minimum SOT current density of 4 x 10^8 A/cm^2 is required to manipulate the center control disk.

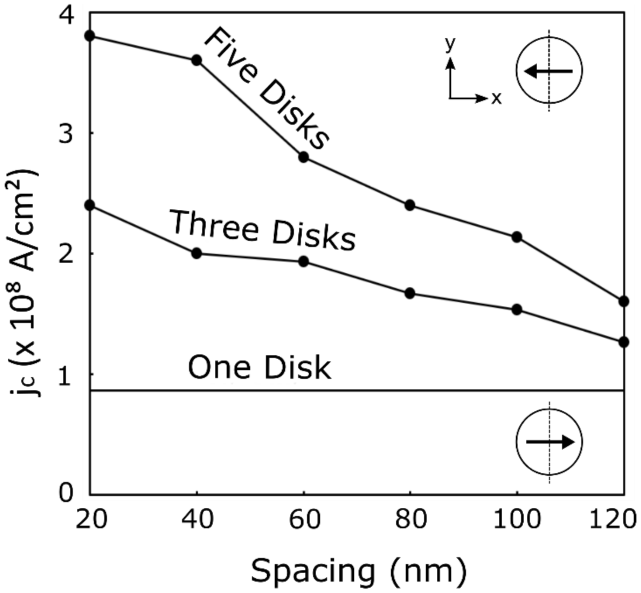

Figure 2-4. The critical SOT current j_c for the center disk in one disk, three disk, and five disk arrangements plotted as a function of disk spacing.

Figure 2-5 compares the outcomes of applying two different SOT current density ramps to disk 3 in a five-disk arrangement while simultaneously clocking disks 2 and 4. Figure 2-5a and Figure 2-5b plot the SOT current density over time for two cases, a 1.33 x 10^8 A/cm^{2}ns (low) slope case to reach 4.00 x 10^8 A/cm^2 at 3.3 ns in Figure 2-5a, and a 40.00 x 10^8 A/cm^{2}ns (high) slope case to reach 4.00 x 10^8 A/cm^2 at 0.4 ns in Figure 2-5b.

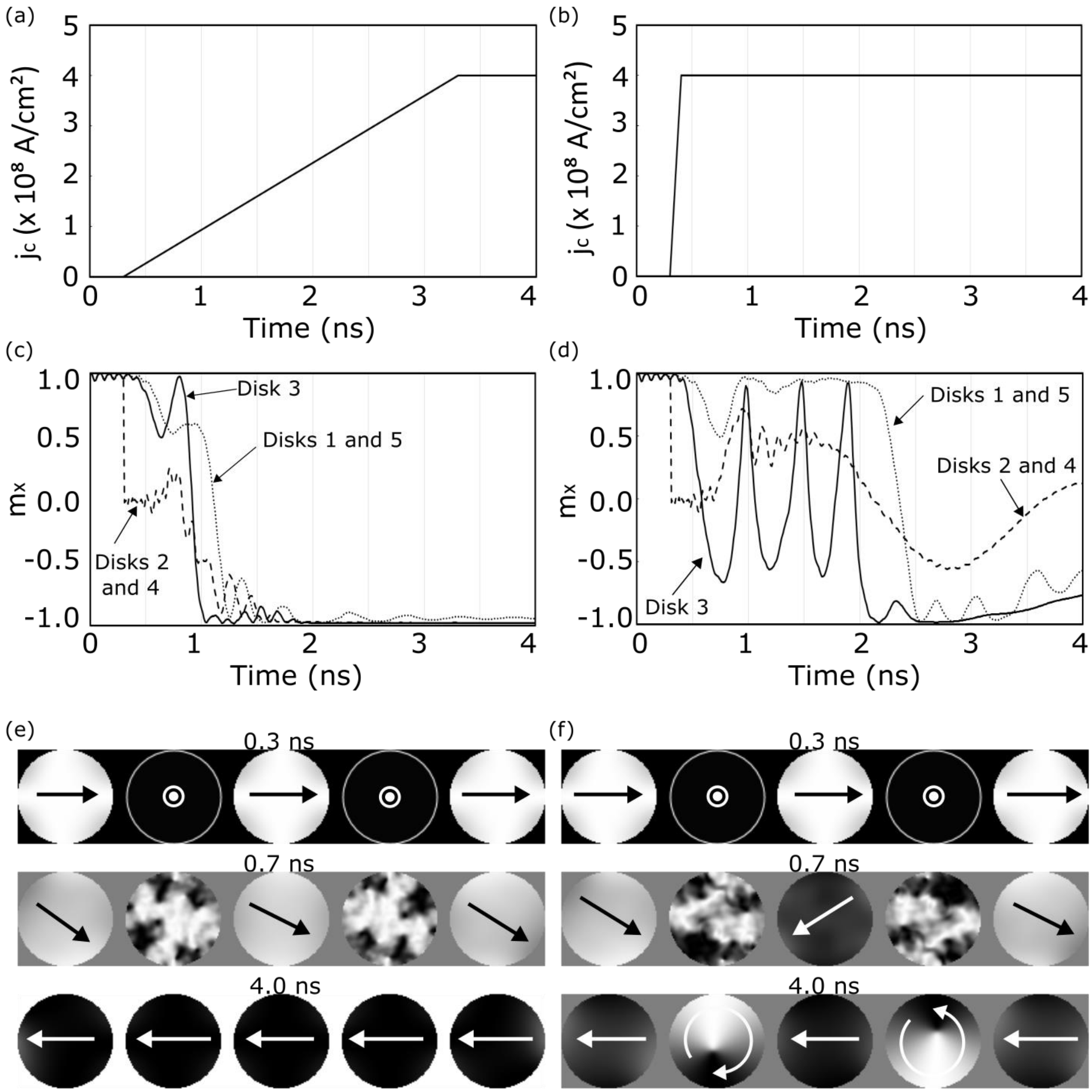

Figure 2-5. SOT current density applied to disk 3 is plotted over time for the low slope case (a) and the high slope case (b). The x-component of magnetization for each disk in the five-disk arrangement is plotted for the low slope case (c) and high slope case (d). Snapshots of magnetization at 0.3, 0.7, and 4.0 ns are shown for the low slope case (e) and high slope case (f).

Figure 2-5c and Figure 2-5d plot the x-component of magnetization for each disk in the five-disk arrangement as a function of time, for the low slope (Figure 2-5a) and high slope (Figure 2-5b) cases respectively. The solid line represents disk 3, the dashed line represents disks

2 and 4, and the dotted line represents disks 1 and 5. In Figure 2-5c, each disk is initialized in a single domain state pointing in the positive x-direction. At 0.3 ns, the x-component of disks 2 and disk 4's magnetizations drop to zero as they are clocked to the z-direction. Following the clocking of disks 2 and 4, all five disks switch to a single domain state pointing in the negative x-direction by t = 1.5 ns, representing their stable state. In Figure 2-5d, each disk is initialized in the same manner as described for the previous case. However, following clocking, disk 3 enters an oscillating state while disks 1 and 5 remain in the positive x-direction. Then, from t = 2.0 to t = 2.5 ns, disks 1, 3, and 5 switch to the negative x-direction and remain in this direction while the x-components of disks 2 and 4 oscillate around zero. The difference between Figure 2-5c and Figure 2-5d cannot be related to current density amplitude since both are the same. The differences between the two cases must be related to the high SOT current density slope used, inducing a dynamic magnetic response. In the high slope case, the current density reaches 4 x 10^8 A/cm^2 quickly, which brings disk 3 into an oscillating state because the SOT counteracts the effective dipole field from the other disks. In this state, disk 3 is "decoupled" and moves relatively independently of the other disks. On the other hand, in the low slope case, the slowly increasing SOT current density switches disk 3 to the negative x-direction and disks 1, 2, 4, and 5 follow shortly after due to dipole coupling in the system.

Figure 2-5e and Figure 2-5f show snapshots of the x-component of magnetization of each disk at times 0.3 ns, 0.7 ns, and 4.0 ns for the low slope and high slopes cases respectively. In these snapshots, the color white represents a magnetization in the positive x-direction, and black represents a magnetization in the negative x-direction. The arrows correspond to the average magnetization direction in each disk, where a straight arrow indicates a single domain in-plane state, and a circular arrow represents a vortex state. At 0.3 ns for both the low slope and high slope cases, disks 1, 3, and 5 are pointed in the positive x-direction, and disks 2 and 4 are pointed in the positive z-direction. The snapshot at 0.7 ns in Figure 2-5e (low slope) shows that disks 1, 3, and 5 are all pointing in the same direction. On the other hand, Figure 2-5f shows the decoupling of disk 3 from disks 1 and 5 at 0.7 ns, as they are pointing in opposite directions. Finally, the snapshots at 4.0 ns show that in the low slope case, disks 2 and 4 end up in single domain in-plane states, whereas in the high slope case, disks 2 and 4 end up in vortex states. In the low slope case, disks 1, 3, and 5 are pointing the same direction and move together, such that in-plane states pointing in that same direction are stable for disks 2 and 4. Vortex states are more stable in the high slope case because while disk 3 is oscillating independently of disks 1 and 5, its dipole field is continuously changing direction such that an in-plane state in any single direction is not stable. These results show that the final states following clocking in a dipole-coupled array depend not only on the amplitude of SOT applied, but also the slope with which it is applied. By varying the slope of the applied SOT current, one can choose whether the center control disk behaves as a computing or non-computing element.

Figure 2-6 plots the net magnetization (10) as a function of SOT current density slope for four SOT current density amplitudes in the five-disk arrangement. SOT current density slope is plotted on a logarithmic axis covering a large range of current slopes from 0.67 x 10^8 to 40.00 x 10^8 A/cm^{2}ns. The graph is divided into three columns and three rows. The rows represent different final states of disks 2 and 4, with the top row corresponding to two in-plane states, the middle row corresponding to one in-plane and one vortex state, and the bottom row corresponding to two vortex states. The columns in the graph represent different current slope regions. The left column represents low current slope values at which disks 2 and 4 ended up in in-plane states, no matter what magnitude of current was applied. The right column represents high current slope values at which both disks 2 and 4 ended up in vortex states. At current amplitudes of 4.00 x 10^8 A/cm^2 and 6.67 x 10^7 A/cm^2, vortex states were consistently achieved in this region, while at lower current amplitudes (6.00 x 10^7 and 5.33 x 10^7 A/cm^2) this is not the case. The middle column represents a transition region in which the outcome is stochastic on current slope and amplitude.

The stable states of disks 2 and 4 can be consistently selected using a current density amplitude above the critical current density for the five-disk arrangement observed in Fig. 4 (4.00 x 10^8 A/cm^2), but also by a current density an order of magnitude lower (6.67 x 10^7 A/cm^2), simply by changing the slope of the applied current ramp. These results reveal how the stable states of disks 2 and 4 depend more on the slope of the SOT current applied to disk 3 than the amplitude of the current, which is true over a wide range of slopes and current amplitudes. This strongly suggests that the slope of the SOT current ramp is a dominant factor in dictating final states, contrary to the intuition that SOT current amplitude is most important. This could have significant implications in future designs where write efficiency is important and can be increased by applying the current more quickly.

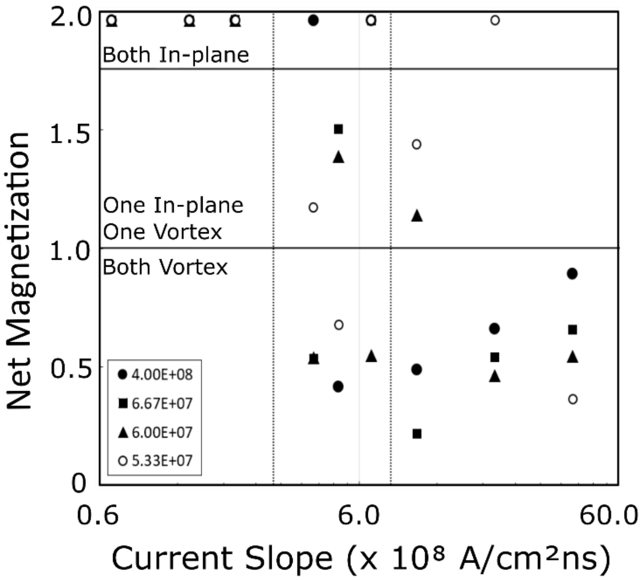

Figure 2-6. The net magnetization of the 2nd and 4th disks in the five disk arrangement following application of SOT current as a function of current amplitudes and slopes. Note the x-axis is presented on a logarithmic scale and covers a large range of applied currents.

Though this work focuses on SOT-based programmability in a 1D array of nanomagnets, as a proof of concept, the same mechanism is valid in 2D grids. This is because the non-computing cells relax from the z-axis in the presence of SOT, while the computation is done in the xy-plane. Therefore, the neighbors of non-computing cells are not influenced by those cells. This is true whether the array extends in 1D or 2D. A 2D nanomagnetic grid representing the magnetic energy minimizing co-processor (MEMCoP) device [86] with spin-orbit torque (SOT) programmability is shown in Figure 2-7. On the left, a top view of a nanomagnetic grid with a hypothetical magnetic layout is shown. Disks marked with an X represent computing elements, while the rest are non-computing elements. The expanded image on the right shows the wiring scheme corresponding to this array. Each element of the array has an n-type metal-oxidesemiconductor (NMOS) access transistor and is wired to a word line (WL), source line (SL), and bit line (BL) for reading and writing as in a traditional random-access memory (RAM) array. These wires are made of a heavy metal such as platinum or tantalum for application of SOT. A procedure to achieve the layout shown on the left is outlined here. Initially, each element in the array is in an in-plane state due to dipole coupling. Once the desired magnetic layout is determined, the computing elements (i.e. those marked with an X in Fig. 7) are clocked to the out of plane direction using polarized current applied through their access transistors. Then, once the clocking current is removed, SOT current is simultaneously applied to the non-computing cells through the BL. Figure 2-6 provides guidance for the necessary amplitude and slope of this applied SOT current ramp to achieve a non-computing state in each of these disks. Finally, the entire array is allowed to relax, and the magnetic states of the computing elements represent the solution to the quadratic optimization problem. As stated earlier, this framework targets QUBO problems that can be mapped onto a 2D grid of nanomagnets in the xy-plane, while the z-direction is used to interface with peripheral circuits. Expanding this architecture to harness dipole coupling in a 3D arrangement could allow for more complex optimization problems to be studied. However, interfacing with peripherals and accessing the magnetic ground states would be challenging. The interested reader is referred to these articles [120]–[122] to see a detailed description of problem mapping and extraction of results from the 2D magnetic layout.

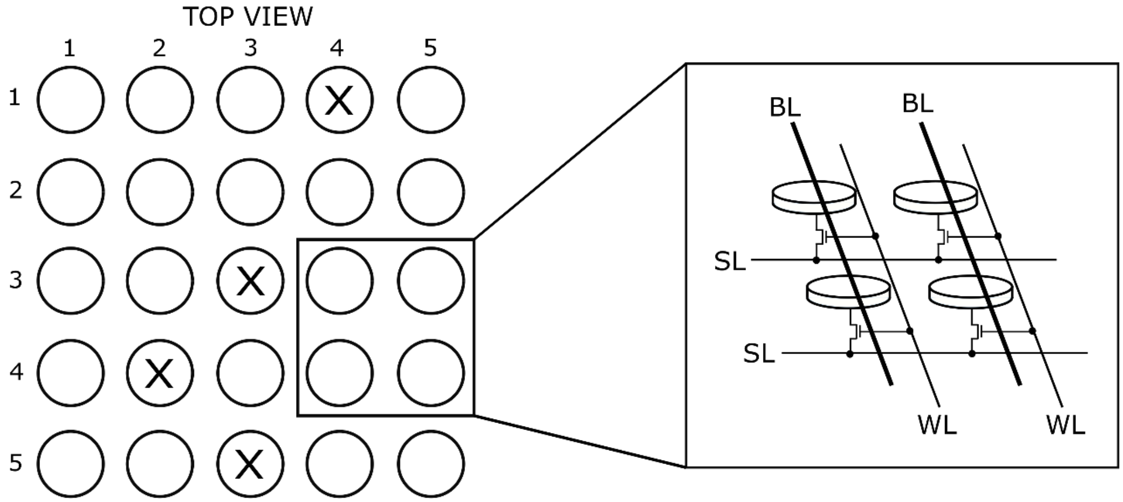

Figure 2-7. A hypothetical magnetic layout in a nanomagnetic array is pictured, where disks marked with an X represent computing elements. The expanded image on the right shows the wiring scheme corresponding to this array in which each element has an NMOS access transistor.

2.4 Conclusion

In conclusion, it was found that dipole coupling energy between adjacent CoFeB nanodisks decreases as disk spacing increases and increases with disk thickness. This relationship governs the critical SOT current density required to switch disks within a dipole-coupled array, as it was observed that critical SOT current density decreases as disk spacing increases in both three disk and five disk arrangements, approaching the isolated disk's critical current density at large disk spacings. Additionally, a phase plot showing the dimensions at which the difference between the energies of in-plane states and vortex states is minimized was produced. For disks with dimensions chosen along this phase boundary, it was found that by varying the slope of a SOT current ramp applied to a control disk, the stable states of adjacent disks could be chosen. At very high current slopes, the adjacent disks prefer vortex states, but at low current slopes, they prefer in-plane states. This phenomenon was observed at a SOT current density an order of magnitude below the previously determined critical current density, which suggests that by utilizing SOT current dynamics, the amplitude of current necessary to switch these disks between computing and non-computing states is much lower than expected. Thus, selective programmability of disks within a dipole-coupled array was demonstrated using SOT current slope as the control method.

3 Magnetization Dynamics in Magnetostrictive Antiferromagnets

In the previous chapter, the importance of considering not only the amplitude of excitation but also the rate at which it is applied was highlighted in the context of dipole-coupled arrays. The ground state of ferromagnetic elements within the array is strongly influenced by the magnetization dynamics of neighboring elements. This chapter now departs from dipole-coupled systems to focus on another material system, magnetostrictive antiferromagnets. These materials possess several qualities that make them promising candidates for non-boolean computing applications, and in this chapter, the influence of dynamic excitation in these systems is investigated.

3.1 Antiferromagnetic Synapse for Neuromorphic Computing

Artificial intelligence (AI) and machine learning represent exciting fields in next generation computing and are currently the focus of an enormous research effort. Typically, these systems are designed with the goal of mimicking the human brain, which excels at tasks like image and pattern recognition that are impossible for traditional computers. This is done using a system of nodes and synapses, modeled after the neurons and synapses in the human brain. Synapses enable learning through a feedback process by adjusting the weight of different signals during the computation to minimize error in the output signal. Devices using this architecture promise groundbreaking advancements in the form of predictive analyses, with a broad swath of applications ranging from healthcare to transportation to entertainment. However, there exists a roadblock to the development of this technology in the form of labeled training data. Many modern AI systems rely on vast amounts of labeled data (data containing labels identifying its content) to serve as references for the learning process, and this labeled data is an expensive resource.

This requirement for labeled training data can be avoided in a class of AI known as Hierarchical Temporal Memory (HTM), a bio-mimetic, neuro-cognitive AI framework. These systems differ from the previously discussed AI frameworks in that rather than going offline to consult training data and adjust synaptic weights, they operate under a continuous influx of data and make real-time adjustments in an unsupervised manner. Examples of this type of framework include [123][124][125][126], consisting of software-based algorithms that show comparable or improved performance over supervised AI frameworks at similar learning and event segmentation tasks. While these software implementations do serve as convincing proofs of concept, the type of calculations involved in the HTM (large number of simple calculations repeated over large number of nodes) lends itself to a hardware implementation. By enabling computation in parallel, hardware implementations can provide a significant reduction in the time-cost associated with this type of neuro-cognitive framework [127]–[131]. The first proposed hardware implementation of the HTM consisted of field programmable gate arrays (FPGAs) [130], and recently, hardware-based platforms using memristors and resistive RAM as reconfigurable synapses have been studied [127]–[129], [131]. These works represent significant advancements towards a high-speed hardware-based HTM implementation, but at best exhibit write-delays on the order of microseconds [132]. This delay is unsuitable for this continuously predictive framework in the environment of constant influx of large amounts of data. Thus, further advancement of the promising HTM framework requires a new, high-speed hardware solution for reconfigurable synapses.

In this work, a hardware solution utilizing a multiferroic antiferromagnet as a reconfigurable synapse in the HTM is considered. To be of use in the HTM, this AFM synapse must exhibit a few key characteristics. The first is stability of intermediate magnetization states (non-volatile states in which the AFM Neel vector is not uniformly aligned in a single direction throughout the AFM synapse). This is an essential characteristic for the AFM synapse in that it makes available a larger number of states beyond 0 and 1, and greater than two states are required for synaptic weighting (two states can only represent fully-ON or fully-OFF). The next key characteristic is an energy efficient write method. It must be possible to program the synapse into its spectrum of states in an energy efficient manner, as the HTM will be making many synaptic adjustments in continuously predictive applications. Finally, the last key characteristic is that the different synaptic states (AFM Neel vector states) must have an observable effect on the output signal, denoted here as read-capability. This third characteristic can be achieved via magnetoresistance. Different AFM states will exhibit different resistances, as discussed earlier in the Chapter 1.1, and this differentiation is how various signals can be weighted using the AFM synapse. This work will focus on investigating the first two characteristics, non-volatile intermediate states and energy efficient writing.

This work focuses on a multiferroic AFM nanowire as a high-speed programmable synapse for HTM applications. Multiferroic AFMs have been the subject of recent research interest both theoretically and experimentally [71]–[77], but remain unexplored in the context of neuromorphic computing applications. Here, an AFM nanowire will be numerically simulated under the influence of dynamic strain pulses with the goal of investigating the stability of strain-induced intermediate AFM states and determining a realistic programming time for switching between these states.

3.2 Simulation Setup

In this work, a finite-element model that combines micromagnetics and elastodynamics is utilized to simulate the response of a multiferroic antiferromagnetic nanowire to dynamic strain pulses. This model uses two oppositely oriented, antiferromagnetically coupled magnetic sublattices to represent the AFM material's magnetization, each of which is governed by its own LLG equation:

$$\frac{\partial \boldsymbol{m}^i}{\partial t} = -\mu_0 \gamma \left(\boldsymbol{m}^i \times \boldsymbol{H}_{\boldsymbol{eff}}^i \right) + \alpha \left(\boldsymbol{m}^i \times \frac{\partial \boldsymbol{m}^i}{\partial t} \right)$$

where i denotes the magnetic sublattice (i = 1, 2) and the remaining terms are defined above in Chapter 1.3. The overall effective field $\boldsymbol{H}_{\boldsymbol{eff}}^i$ for each sublattice consists of contributions from exchange, MCA, magnetoelastic, and AFM effective field terms. The AFM effective field term for each sublattice is defined as:

$$H_{AFM}^{i=1,2} = \frac{J m^{2,1}}{\mu_0 M_s^{1,2}}$$

where J is the antiferromagnetic exchange coupling constant. A factor of 0.5 is multiplied by both the magnetoelastic and MCA effective field terms for each sublattice under the assumption that both terms affect each sublattice equally. The magnetostrictive coupling between magnetization and strain is represented by the magnetoelastic effective field, which relies on calculation of the strain tensor in the simulated material via the elastodynamic and strain-displacement equations:

$$\rho \frac{\partial^2 \boldsymbol{u}}{\partial t^2} - \nabla \boldsymbol{\sigma} = 0$$

$$\boldsymbol{\varepsilon} = \frac{1}{2}[\nabla \boldsymbol{u} + (\nabla \boldsymbol{u})^T]$$

where ρ is the density, $\boldsymbol{u}$ is displacement, and $\boldsymbol{\sigma}$ is elastic stress.

The material properties are chosen to represent an antiferromagnetic material with a likeness to magnetostrictive alloy FeMn. Research on magnetostrictive AFMs is still in early stages and some material properties are unavailable in literature. When this is the case, the corresponding values for the individual ferromagnetic sublattices are used: $A_{ex(Fe)}$ = 2.48 x 10^{-12} J/m [133], $M_{s(Fe)}$ = 5.66 x 10^5 A/m, $J_{(Fe)}$ = 3.97 x 10^6 J/m^3, λ_s = 750 ppm [134], [135], cubic anisotropy constants K_1 = -4.5 x 10^3 J/m^3 and K_2 = 2.3 x 10^3 J/m^3, Young's modulus E = 77 GPa [136], ρ = 7700 kg/m^3, Gilbert damping α = 0.02, and Poisson's ratio ν = 0.3. The geometry of the AFM nanowire consists of a 300 x 50 x 5 nm^3 rectangular volume meshed with a cuboidal finite element mesh with elements of length 2.5 nm. Mechanical boundary conditions are enforced on faces 1 (prescribed displacement) and 6 (fixed constraint) of the AFM nanowire as shown in Figure 3-1a. The nanowire is initialized with its Neel vector aligned along the x-axis, which due to the saturation magnetostriction of 750 ppm, results in an initial nanowire length of 300.225 nm (ε_{xx} = 750 με). To accommodate this initialization state, face 6 of the nanowire is constrained at a displacement of +1.125 Å, while face 1 is initialized with an initial displacement x_1 = -1.125 Å. In the studies described next, dynamic strain is applied to the nanowire through displacement of face 1, to simulate the effect of an elastic wave incoming from the -x direction.

The first study, illustrated in Figure 3-1b, investigates the stability of intermediate AFM states in the AFM nanowire. The nanowire is initialized with its Neel vector uniformly aligned along the x-axis (100%X) and with a displacement on face 1 of x_1 = -1.125 Å. Following a 1 ns relaxation in this state, x_1 is ramped from -1.125 to 0.000 Å over a period of 0.500 ns, corresponding to a strain of ~375 με. This strain amplitude was chosen to result in an AFM state in which the Neel vector in 1/3 of the nanowire is oriented along the z-axis, and 2/3 is oriented along the x-axis (66%X). Following the strain ramp, the displacement is held constant at 0.000 Å for 0.250 ns to allow the AFM state to stabilize, then the prescribed displacement constraint on face 1 is removed and the nanowire is allowed to relax in an unconstrained state for 0.500 ns. Following this relaxation, this strain ramp-hold-release procedure is repeated twice more with 1.125 Å displacements in the +x-direction, to drive the nanowire into 33%X and 0%X states. Throughout this study, the displacement on face 1, the magnetization of one sublattice (m^1) averaged over the volume of the nanowire, and the ε_{xx}, ε_{yy}, and ε_{zz} components of the strain tensor averaged over the volume of the nanowire are recorded.

In the second study, shown in Figure 3-1c, the speed at which strain-induced switching between the desired intermediate states can be achieved is investigated by varying the ramp time of the applied displacement on face 1, during the switch from the 100%X to 66%X state. Successful switching between 100%X and 66%X states is quantified through both the magnetization of one sublattice m^1 averaged over the nanowire volume, and the net magnetic moment in the nanowire, defined as :

$$Net\ Moment = \sqrt{(m_x^1 + m_x^2)^2 + \left(m_y^1 + m_y^2\right)^2 + (m_z^1 + m_z^2)^2}$$

Following initialization and 1.000 ns relaxation in the 100%X state, x_1 is ramped from -1.125 Å to 0.000 Å over a period t_{ramp}. t_{ramp} is varied across five orders of magnitude, taking values of 2.432E-5, 0.001, 0.010, 0.125, and 0.500 ns. At the lower end, the 2.432E-5 ns ramp time corresponds to the mechanical pressure-wave speed in the simulated material, and is thus an upper limit on the strain rate [79]. On the other hand, the 0.500 ns ramp time corresponds to a resonant frequency of 2 GHz, similar to the FMR frequencies of FM materials. As such, this range of t_{ramp} covers the broad range-of-interest for AFM materials with THz resonances.

Following the strain ramp, the displacement x_1 is held constant at $x_1 = 0.000$ Å for 0.250 ns, then the constraint is removed and the nanowire is allowed to relax for 0.500 ns.

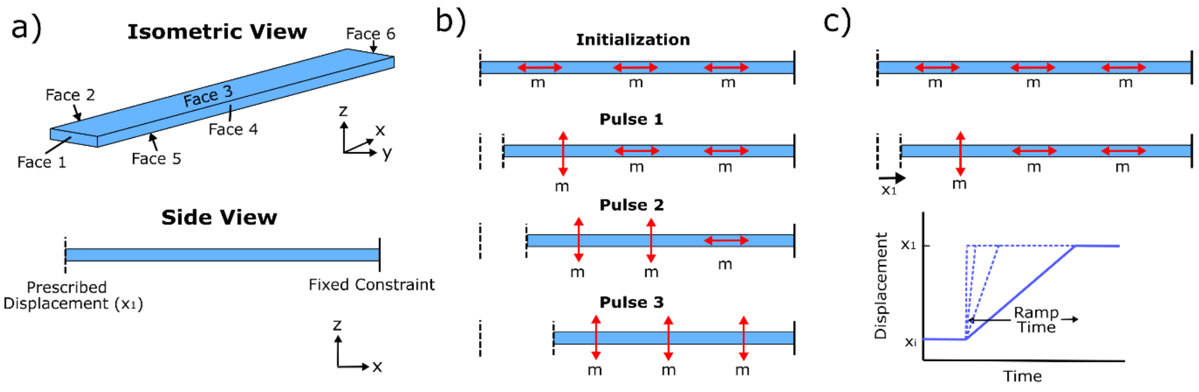

Figure 3-1. Simulation geometry and setup for AFM modeling studies.

3.3 Results and Discussion

Figure 3-2a plots the displacement of face 1 of the AFM nanowire over time. During the 1 ns initialization period, this displacement is constrained to a value of -1.125 Å. At time t = 1 ns, the displacement is ramped up from -1.125 to 0.000 Å over a period of 0.500 ns, followed by a 0.250 ns hold at 0.000 Å. Following this hold, the constraint on face 1 is removed and the nanowire relaxes for a period of 0.500 ns, shown by the highlighted grey region on the plot. This ramp-hold-release sequence constitutes one strain pulse. At time t = 2.260 ns, another strain pulse is initiated, and again at time t = 3.510 ns. Figure 3-2b plots the volume-averaged magnetization of one AFM sublattice (m^1) over time. From time t = 0 to t = 1 ns, the AFM nanowire is in the 100%X state, with mx = 1 and my = mz = 0. As the displacement is ramped up over the first strain pulse, the x-component of magnetization drops to a value close to 0.7, while the z-component of magnetization increases to ~0.35, indicating a switch into the 66%X case. When the constraint is released, the magnetization shows some small oscillation but remains in the 66%X state. Similarly for the second and third strain pulses, the x-component of the magnetization drops from 0.7 to 0.35 from the second pulse, and from 0.35 to 0 from the third pulse indicating switches from 66%X to 33%X, and from 33%X to 0%X states. During these pulses, the z-component of magnetization increases from ~0.35 to 0.7, then from 0.7 to 1.0, while the y-component of magnetization remains at 0 throughout the entire study.

Figure 3-2c shows the volume-averaged strain in the AFM nanowire over time. During the first strain pulse, ε_{xx} drops from 750E-6 to 375E-6, while ε_{zz} increases from -375E-6 to 0. The remaining two strain pulses result in changes in ε_{xx} from 375E-6 to 0, then from 0 to -375E-6, and in ε_{zz} from 0 to 375E-6, and then from 375E-6 to 750E-6, respectively. Finally, Figure 3-2d shows snapshots of the magnetization state in the AFM nanowire at four points in time, t = 0, 2.26, 3.51, and 4.76 ns. At time t = 2.26 after the first strain pulse, the magnetization in the front ~1/3 of the nanowire has switched from the x-axis to the z-axis (66%X state). At t = 3.51 after the second strain pulse, the fraction of the nanowire orientated along the z-axis increases to ~2/3 (33%X). After the final strain pulse at t = 4.76 ns, the nanowire has been fully reoriented to the z-axis (0%X).

These results confirm that the AFM nanowire can be driven into non-uniform, intermediate states via strain, and that these states are stabilized by the nanowire’s magnetocrystalline anisotropy. The magnitude of the applied strain (375 $\mu\varepsilon$) corresponds to a 90° switch of 1/3 of the nanowire’s magnetization away from its initial axis. If the nanowire lacked MCA, this applied strain would instead cause coherent canting of the magnetization away its initial state, rather than a full 90° switch from x to z in only 1/3 of the nanowire. This is because in the absence of MCA, the magnetization state in the nanowire is fully determined by the exchange interaction, which holds the spins in each sublattice in a coherent, parallel orientation.

In addition to enabling 90° switching in small segments of the nanowire, the nanowire's MCA facilitates the non-volatility of these intermediate states. In the absence of MCA, there is nothing holding the AFM's spin state in place upon removal of the applied strain and the magnetization will likely return to its initial state as dictated by any residual stresses in the material. In the system with MCA, this anisotropy works to hold the intermediate spin state in place upon removal of strain. It is predicted that for this MCA-mediated synapse mechanism to work, the anisotropy energy density associated with the MCA must be greater than that of the intra-lattice exchange, which acts to realign the magnetization in a uniform orientation. In addition to highlighting the importance of MCA in the AFM synapse, these results provide baseline magnetization values which can be used to quantify the presence of each intermediate state (i.e. 66%X corresponds to $m_x = 0.7$).

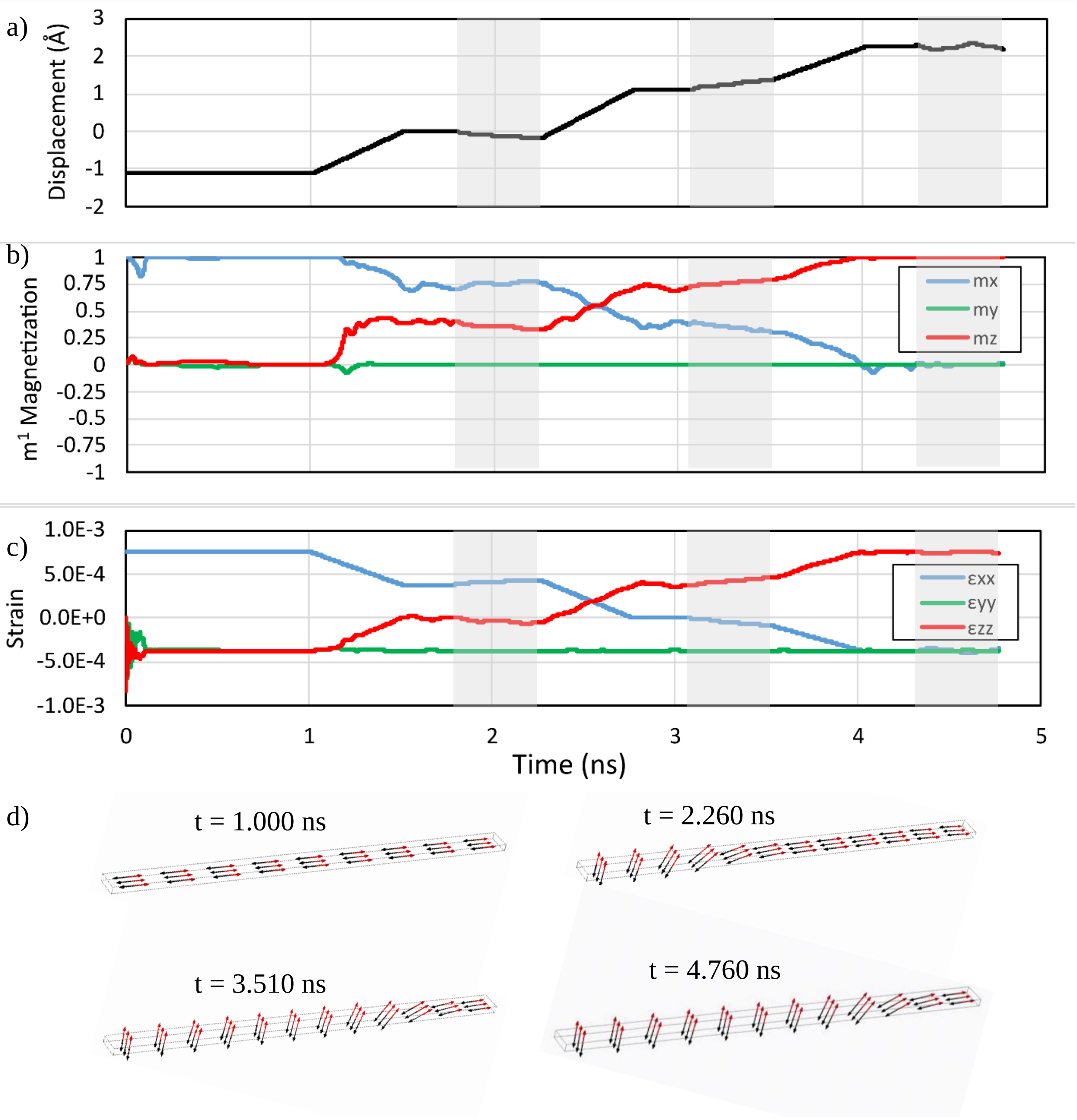

Figure 3-2. a) Displacement of face 1 over time (grey regions indicate times when constraint on face 1 was removed). b) Volume-averaged magnetization of one AFM sublattice vs. time. c) Volume averaged strain in the AFM nanowire vs. time. d) Snapshots of the AFM magnetization states at times t = 0, 2.26, 3.51, and 4.76 ns.

Figure 3-3a plots the displacement of face 1 over time, for the five different strain ramp times studied here (0.500, 0.125, 0.010, 0.001, and 2.432E-5 ns). Following each displacement ramp, the displacement is held constant at $x_1 = 0$ Å for a period of 0.25 ns. Figure 3-3b plots the volume-averaged x-component of magnetization for one sublattice (m^1) over time, for each strain ramp time. The black dashed line indicates the $m_x = 0.7$ mark, which signifies that the nanowire has entered the desired 66%X state. For the longer ramp times (0.500 and 0.125 ns), m_x changes slowly during the ramp, and reaches the $m_x = 0.7$ state by the end of the ramp. On the other hand, the faster ramp times (2.432E-5, 0.001, and 0.010 ns) each consistently drive the nanowire's magnetization towards the $m_x = -1$ state over a period of 0.100 ns before turning back to a $m_x = 0$ state. Figure 3-3c plots the volume-averaged net magnet moment (defined in chapter 3.2) over time for each strain ramp. Each of the faster ramp times (2.432E-5, 0.001, and 0.010 ns) show sharp peaks in net moment immediately following the initiation of the strain pulse. The magnitude of these peaks vary inversely with the strain ramp time. The shortest ramp time (2.432E-5 ns) corresponds to a peak in net moment of ~1.75%, whereas a longer ramp time of 0.010 ns results in a smaller peak net moment of ~0.50%. On the other end of the spectrum, the two slower ramp times, 0.500 and 0.125 ns, do not exhibit the sharp peak following initiation of the strain pulse, but rather increase gradually throughout the entire ramp time, with peaks in net moment that are much lower than those of the faster ramp times, 0.10% and 0.20% respectively.

These results show a strong difference in magnetic response between the ramp times slower than 0.125 ns, and the ramp times faster than 0.010 ns. While the two slower ramp times drive the nanowire into the desired 66%X state, ramp times of 0.010 ns and faster have an entirely different effect on the nanowire's magnetization and net moment. The small, gradual changes in net moment observed for the 0.500 and 0.125 ns ramp times indicate that this rate of excitation induces a quasi-static response. On the other hand, the sharp peak in net moment and dramatic magnetization changes observed for the 0.010, 0.001, and 2.432E-5 ns ramp times indicate that these strain rates excite a dynamic response in the AFM nanowire. In previous work, the AFM resonance of this system was determined to be 354 GHz [79]. This frequency corresponds to a an excitation period of 1/354GHz = ~0.003 ns, close in magnitude to the faster strain ramp times tested here. This indicates that the dynamic response observed for the faster ramp times arises as the ramp time approaches the resonant excitation period of the system. In terms of design of the AFM synapse, these results provide useful information on the lower bound of switching speeds that can reliably program the synapse.

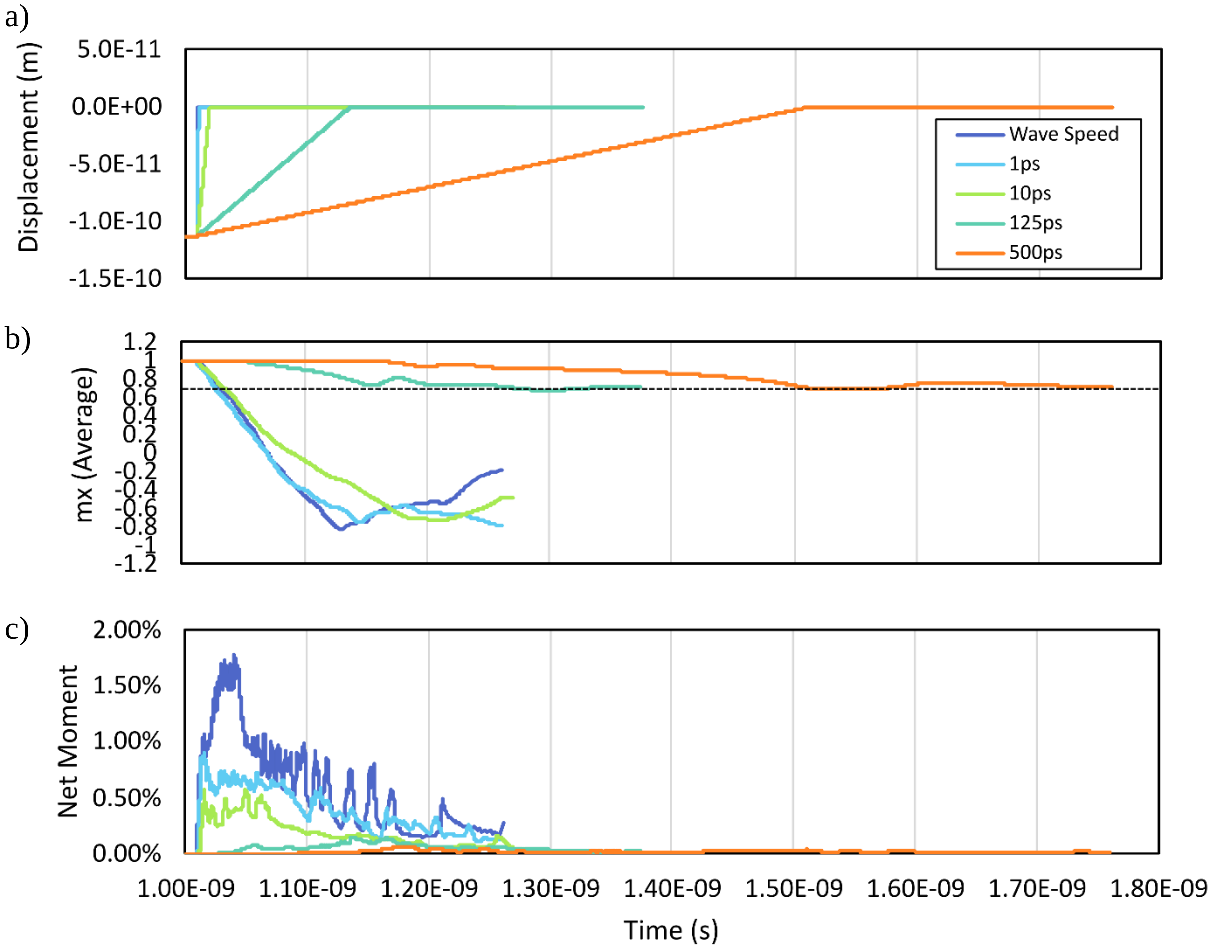

Figure 3-3. a) The displacement time profiles associated with the range of strain rates studied here (corresponding to resonant frequencies ranging from ~100 THz to 2 GHz). b) Volume-averaged x-component of magnetization over time for each strain rate. c) Volume-averaged net magnetic moment in the AFM nanowire.

Figure 3-4 plots the x-component of the principle strain (ε_{xx}) at three different locations in the AFM nanowire, the front (25 nm from face 1), the center (150 nm from face 1), and back (275 nm from face 1). Figure 3-4a plots ε_{xx} at each of these points for the 0.010 ns strain ramp case, and Figure 3-4b plots ε_{xx} at each of these points for the 0.125 ns strain ramp case. In the 0.010 ns case, there is a sharp peak in compressive strain of magnitude ~3500 με at t = 1.022 ns at the front, followed by a smaller peak with width of 0.085 ns (from t = 1.062 to t = 1.147 ns) with a maximum of ~2000 με in the center, and finally a third peak at the back with a maximum of ~900 με and a width of 0.189 ns (from t = 1.128 to t = 1.317 ns). In the 0.125 ns strain ramp case, the strain at the front of the nanowire gradually changes from +750 με to -375 με during the strain ramp and remains at this value for the remainder of the study. The strain at the center and back of the nanowire exhibit small oscillations at the onset of the strain ramp, but remain at 750 με for the entirety of the study. The onset of the changes in the strain signal at the front, center, and back of the nanowire are offset in time with similar spacing as the onset of the compressive strain peaks in the 0.010 ns case, but do not show the decreases in magnitude and increases in width.

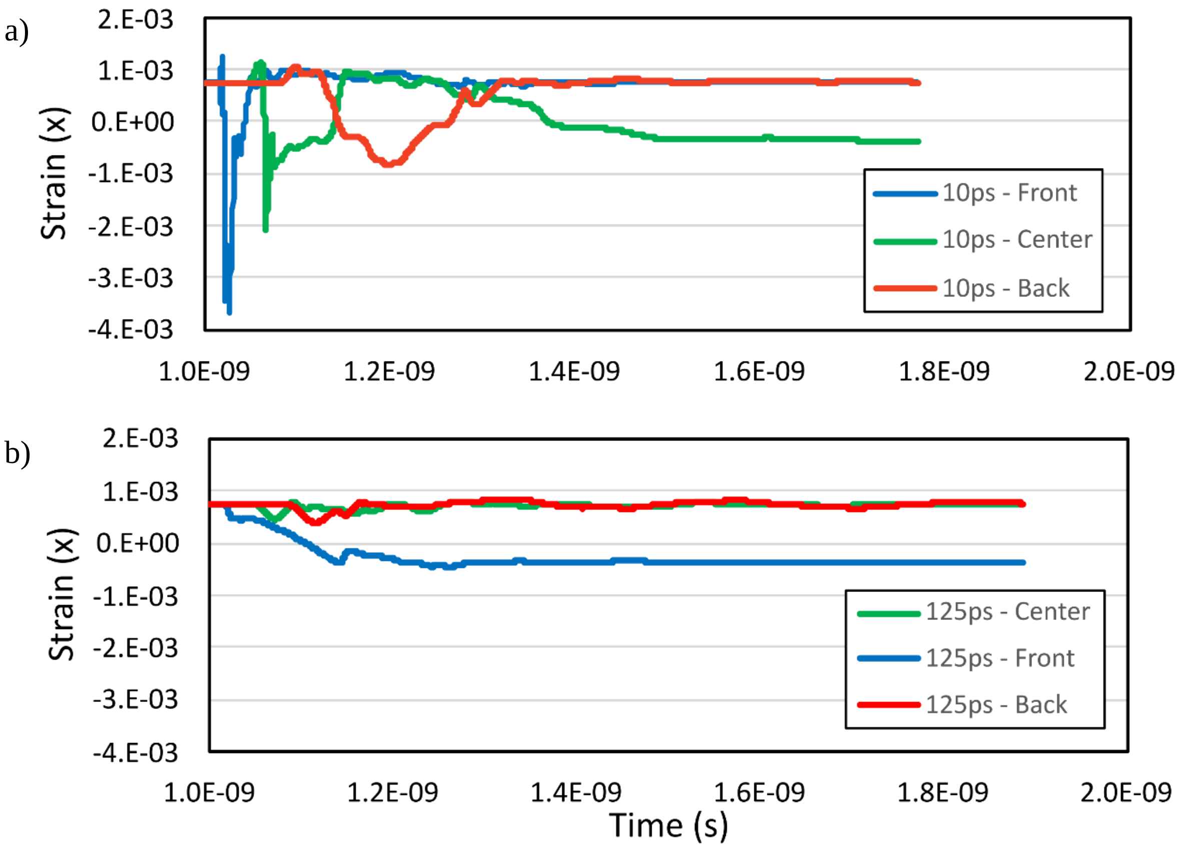

Figure 3-4. a) ε_{xx} measured at three locations in the AFM nanowire (front, center, and back) during the 0.010 ns strain ramp. b) ε_{xx} measured at three locations in the AFM nanowire (front, center, and back) during the 0.125 ns strain ramp.

These results provide evidence showing the difference in the type of mechanical and magnetic states that are excited by the fast (0.010 ns) strain ramp and slow (0.125 ns) strain ramp cases. In the fast ramp case, the successive peaks in compressive strain indicate that the applied strain launches a compressive elastic wave in the nanowire. As it travels down the length of the nanowire, this wave loses energy to changes in the magnetization due to the magnetoelastic coupling. This loss of energy is apparent in the progressively decreasing peak magnitude as the wave travels from the front, to the center, then to the back of the nanowire. In the 0.125 ns strain ramp case, a similar time-offset is seen in the onset of changes in strain between the front, center, and back of the nanowire. This indicates a similar traveling strain wave through the length of the nanowire but with much smaller magnitude and no apparent reduction in magnitude between the front, center, and back. After the initial change in strain that is seen in all three locations, both the center and back return to the initial +750 με state while the front switches to the -375 με state. These observations indicate that in the slower ramp case, an elastic wave is excited but with small enough magnitude that it does not induce significant change in the magnetization and thus, does not show the same loss in energy across the nanowire's length. Along with this small elastic wave, the slowly increasing strain causes a quasi-static change in the magnetization in which the front 1/3 of the nanowire switches from the x-axis to the z-axis while the remainder of the nanowire remains aligned along the x-axis (66%X state) as discussed in the previous results.

3.4 Conclusion

In conclusion, this work demonstrates the ability to use energy-efficient strain to program intermediate, non-volatile states into an AFM nanowire, and identifies an upper bound for the speed at which these states can be programmed. It was shown that using the following strain pulse sequence (0.500 ns ramp, 0.250 ns hold, release), the nanowire's Neel vector can be switched from the initialized x-axis to the z-axis in segments of 1/3 of the nanowire's length, and that these intermediate states are stabilized by the AFM's MCA. By varying the rate at which the strain is applied, it was observed that at faster ramp rates (those approaching the AFM resonance of the system) a high energy elastic wave is launched through the nanowire resulting in dynamic changes in magnetization, but not producing the desired, non-volatile intermediate state. At ramp rates on the order of 0.125 ns and slower, these dynamic magnetization changes are avoided and the nanowire exhibits gradual, quasi-static magnetization change into the desired intermediate state. Thus, this work demonstrates the potential for an AFM nanowire to function as a high-speed- energy efficient synapse for continuously predictive AI frameworks.

4 Low-Energy Control of Magnetization Dynamics for Magnetic Memory

In previous chapters, the influence of varying the rate of excitation on the ground state of FM elements in a dipole coupled array, and on the stability of intermediate AFM states in an AFM nanowire was demonstrated. These works have application in non-boolean computing, and given the early stage of development in this field, serve mainly as proofs of concept. On the other hand, this chapter focuses on magnetic memory, a relatively mature field. The goal of this work is to provide information helpful to the implementation of low-energy SOT-mediated magnetic memory bits, as well as to explore the capability of various strain-clocking mechanisms, which may have application in both magnetic memory as well as logic and non-boolean computing applications as an extremely low energy method of perpendicular magnetization control.

4.1 Strain-Assisted DMI Switching

Magnetic memory architectures that utilize the spin-orbit torque writing method to control perpendicular magnetization remain the goal of a significant research effort, due to the benefits in energy efficiency and endurance afforded by SOT. The main hurdle facing integration of this writing method in industry-applicable memory systems is symmetry breaking. SOT can stabilize in-plane states in magnetic memory bits with PMA, but upon removal of the SOT current, the magnetization enters an unstable equilibrium under the influence of the uniaxial perpendicular anisotropy. Various methods of OOP symmetry breaking have been investigated, including external field, structural gradients, and additional FM or AFM layers in the MTJ stack

[20], [21], [23]–[28]. These methods succeed in enabling deterministic PMA switching, but none are suitable for large scale industrial application due to fabrication complexities involved in structural gradients and additional biased layers. Very recently, a mechanism of symmetry breaking that utilizes the inherent DMI present in heavy metal/FM interfaces, along with various types of lateral and OOP magnetic gradients, achieved field free PMA switching [29]. The field free switching achieved in the CoFeB/CoFe stack with OOP M_s gradient represents a symmetry breaking mechanism that can be directly integrated into wafer-scale MTJ manufacture.

That work demonstrated that the combination of DMI and magnetic gradient can produce deterministic field-free SOT switching in systems with PMA. While this is a huge step towards industrial application of energy efficient magnetic memory, this method still relies 100% on electric current which is inherently inefficient at the nanoscale (due to Joule heating). In addition to this, it has been shown that decreasing magnetic bit size, which is the entire goal of developing high-density memory, results in significant increases in critical SOT switching current. In a Ta/CoFeB/MgO system, reducing magnetic bit size from micron-scale hall bar structure to 80 nm diameter nanodot results in an order of magnitude increase in critical SOT current [137]. In the interest of energy efficiency, it is critical to reduce the threshold SOT switching current in magnetic memory systems, as well as investigate mechanisms by which electric current can be abandoned altogether. Voltage-induced strain represents a promising method of energy efficient magnetization control, with the ability to control perpendicular magnetization at energies on the order of attojoules [51], as opposed to the femtojoules associated with STT and SOT. The addition of in-plane strain to MTJ structures via piezoelectric substrates has been shown experimentally to result in 30% reduction of coercive field in Co/Ni multilayers with PMA [48], and shown through macrospin calculations to significantly reduce

SOT switching current in MTJ structures with synthetic AFM free layer through timed combination of strain and SOT current [49]. These works demonstrate the capability of in-plane strain to reduce the energy barrier to PMA switching. Regarding material systems exhibiting DMI, strain has been shown to influence DMI magnitude, as well as enable control over creation, deletion, and propagation of skyrmions [138]–[140]. However, the interaction between strain and DMI in the context of PMA symmetry breaking for deterministic switching is unexplored, and merits further investigation due to its strong potential for extremely energy efficient, field-free deterministic switching in industrial applications.

In this work, the potential for reduction in DMI-mediated critical SOT switching current is investigated in two ways. First, the addition of in-plane strain to the DMI + magnetic gradient SOT switching scheme is studied via current-induced hysteresis loops, with the goal of reducing the critical SOT current needed to induce deterministic switching. Second, a mechanism for direction-controlled strain clocking via a perpendicular effective field is studied, with the goal of enabling pure-strain mediated PMA switching for ultra-low magnetic memory and clocking applications.

4.2 Simulation Setup

In this work, a micromagnetic finite-difference model is used to simulate the steady-state response of circular magnetic bits with interfacial DMI and lateral PMA gradient to the combined influence of SOT and voltage-induced strain. This model is represented by the Landau-Lifshitz-Gilbert (LLG) equations withs SOT terms added:

$$\frac{\partial \boldsymbol{m}}{\partial t} = -\mu_0 \gamma \left(\boldsymbol{m} \times \boldsymbol{H_{eff}}\right) + \alpha \left(\boldsymbol{m} \times \frac{\partial \boldsymbol{m}}{\partial t}\right) + \frac{j_c \hbar \theta_{\mathrm{SH}}}{2eM_s t}\left[\left(\boldsymbol{m} \times (\boldsymbol{\hat{\sigma}} \times \boldsymbol{m})\right) - \beta(\boldsymbol{m} \times \boldsymbol{\hat{\sigma}})\right] \qquad (1)$$

with term definitions outlined in Chapter 1.3. $\boldsymbol{H_{eff}}$ is the effective field with contributions from the exchange field ($\boldsymbol{H_{ex}}$), demagnetization field ($\boldsymbol{H_{d}}$), PMA ($\boldsymbol{H_{PMA}}$), DMI ($\boldsymbol{H_{DMI}}$), and the magnetoelastic field ($\boldsymbol{H_{me}}$). It is assumed that SOT is applied uniformly throughout the magnetic bit. This work focuses on circular magnetic elements to avoid shape anisotropy effects, and thermal fluctuations are neglected. The material being modeled is pseudo-amorphous CoFeB. Under the assumption that exchange length (3-4 nm) is larger than as-deposited grain size, magnetocrystalline anisotropy (MCA) is neglected. Thus, the overall effective field is represented by:

$$\boldsymbol{H}_{eff} = \boldsymbol{H}_{ex} + \boldsymbol{H}_{d} + \boldsymbol{H}_{PMA} + \boldsymbol{H}_{DMI} + \boldsymbol{H}_{me} \qquad (2)$$

Small elastic deformation and uniform strain throughout the CoFeB bits are assumed. The above equations are solved using a commercially available finite-difference solver that utilizes Neumann boundary conditions ($\frac{\partial \boldsymbol{m}}{\partial \hat{n}} = 0$) at the magnetic material's edges [118].

The CoFeB bits studied here are represented by circular geometries with 2 nm thickness and varying diameters, shown in Figure 4-1. Each bit is discretized in 1 nm cubic elements, with material parameters A_{ex} = 2 x 10^{-11} J/m, M_s = 9.55 x 10^5 A/m, α = 0.02, λ_s = 50 ppm, and E = 160 GPa. The DMI coefficient D = 50 μJ/m^2 corresponds to that measured for Ta/CoFeB/MgO stacks [29]. Regarding the relative magnitudes of field and damping-like torques, a value of β = 2 is chosen based on hall resistance measurements of transverse and longitudinal SOT-induced effective fields in Ta/CoFeB/MgO stacks [141]. The lateral PMA gradient in our system is represented by a base anisotropy constant $K_{u-base} = 6 \times 10^5 \frac{J}{m^3}$ and a position-dependent anisotropy term $K_{u-grad} = 5.05\ \frac{J}{m^3} \cdot nm^{-1}$, such that $K_u(y) = K_{u-base} + K_{u-grad} * y$. The

PMA increases from the bottom (y = 0) to the top (y = bit diameter) of the magnetic bit, corresponding to a CoFeB thickness gradient $\frac{\partial t}{\partial y} = -0.018 \frac{nm}{mm}$ [29].

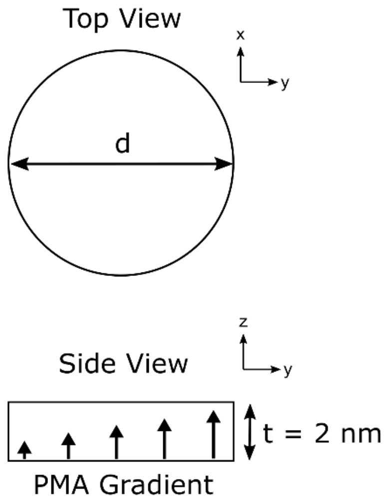

Figure 4-1. Finite difference geometry and direction of PMA gradient in CoFeB element.

This work consists of three studies in which the influence of magnetic bit size and voltage-induced strain on critical SOT switching current density are determined. Here, the critical SOT switching current density, j_{crit}, is defined as the minimum SOT current density that, when applied along the $\hat{x}$ axis, successfully induces switching between positive and negative m_z states. The first study shown in Figure 4-2a evaluates the dependence of j_{crit} on magnetic bit size. A bit with diameter d is initialized in either a $+m_z$ or $-m_z$ state. Then, an SOT current of magnitude j_c is applied along the x-axis. This SOT current remains applied until the magnetization reaches a stable state, then the SOT current is removed and the bit relaxes to its final state. This procedure is repeated for SOT current magnitudes ranging from +8 x 10^7 A/cm^2 to -8 x 10^7 A/cm^2 in steps of 1.5 x 10^5 A/m^2 to generate SOT switching hysteresis curves for bit diameters ranging from 50 to 250 nm in steps of 50 nm.

The second study, shown in Figure 4-2b, focuses on identifying the relative angle θ_ε between PMA gradient ($\hat{y}$) and applied strain axis ($\hat{\varepsilon}$) at which the energy barrier to switching (and thus the critical SOT switching current) is minimized. Focusing on a bit diameter of 100 nm, the above procedure for determining SOT current-induced hysteresis loops is repeated with the addition of a +1000 με strain pulse applied along in-plane axis $\hat{\boldsymbol{\varepsilon}}$**.** This strain pulse is applied and removed simultaneously with the SOT current pulse applied along the x-axis. This process is repeated varying the angle between the strain axis $\hat{\boldsymbol{\varepsilon}}$ and the PMA gradient **(**$\hat{\boldsymbol{y}}$**)** for angles θ_ε = 0°, 45°, 90°, and 135° by varying the axis along which strain is applied.

The third and final study shown in Figure 4-2c is used to compare three mechanisms of strain symmetry breaking, with the goal of demonstrating low-energy, direction-controllable strain clocking. A bit of diameter 100 nm (without PMA gradient and interfacial DMI) is initialized into one of five $+m_z$ states, one aligned directly along the z-axis, and four with a slight cant from the z-axis (+0.06° x, -0.06° x, +0.06° y, and -0.06° y). Following this initialization, strain of magnitude +0.8% is applied along the y-axis to bring the magnetization in-plane. This 90° strain switching is repeated under four different conditions. First, in the absence of any additional applied or effective field. Second, in the presence of a small external field applied along the x-axis. Third, in the presence of a small SOT current applied along x-axis, and fourth, in the material system including both interfacial DMI and PMA gradient that was focused on in previous studies. For each respective symmetry breaking mechanism (external field, SOT, DMI + gradient), the corresponding magnitude (magnitude of external field, current density of SOT, and D_{ij} of DMI) is increased until the magnetization consistently switches in the same direction, to determine the minimum magnitude for each mechanism at which controllable strain clocking occurs.

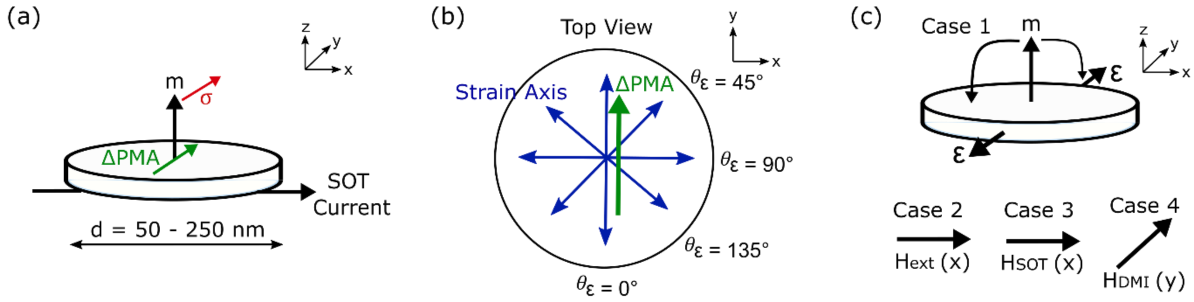

Figure 4-2. Simulation setup for strain-assisted SOT switching studies.

4.3 Results and Discussion

Figure 4-3a shows the current induced hysteresis loops calculated for five different magnetic bit diameters (50, 100, 150, 200, 250 nm). The z-component of magnetization is plotted on the y-axis and SOT current density on the x-axis. For each hysteresis loop, the curve represents the final magnetization state after application and removal of an SOT writing current pulse. For the magnetic bit with 50 nm diameter, above the critical switching current (highlighted in the red box), the final state oscillates with applied current and this behavior is independent of applied current polarity (occurs at same critical current for both positive and negative SOT currents). For the bit with 100 nm diameter, deterministic switching occurs with polarity such that positive SOT currents induce switching to the $+m_z$ direction, and negative SOT currents induce switching to the $-m_z$ direction. At each magnetic bit size above 100 nm, deterministic switching occurs, but with reversed polarity (+ SOT current switches to $-m_z$ direction and vice versa). Figure 4-3b plots both critical switching current Jc, and demagnetization energy density as a function of magnetic bit diameter. The critical switching current decreases from ~8 x 10^7 A/cm^2 at 50 nm diameter to ~ 4 x 10^7 A/cm^2 at 250 nm diameter. Conversely, the demagnetization energy increases as magnetic bit size increases, due to the larger in-plane dimension associated with the larger bit diameters.

These results quantify the size dependence of the critical SOT switching current, Jc, in the DMI-mediated field free switching system. By comparing the observed trend in increasing Jc with reduced bit size to the observed trend in decreasing demagnetization energy, it is apparent that demagnetization energy plays a significant role in the elevated critical current seen at smaller bit diameters. This dependence lies in the fact that the demagnetization energy in this geometry prefers an in-plane magnetization, opposing the OOP magnetization preferred by the system's PMA. As the demagnetization energy increases, it becomes easier for the SOT current to rotate the magnetization away from the OOP direction. At small diameters, since the demagnetization energy is small, a greater SOT current is needed to induce this rotation away from the OOP direction. These results serve to highlight the necessity of investigating more energy efficient write methods beyond SOT, as the critical switching current doubles approaching the bit size desirable for high density memory.

Another observation to be noted is the dependence of switching polarity on magnetic bit size. At the smallest bit diameter (50 nm), deterministic switching is not achieved, but rather magnetization clocking occurs at SOT currents above Jc. In the 100 nm bit, deterministic switching is achieved with a "positive" polarity (+ SOT current switches to $+m_z$ direction). At larger bit diameters, this polarity reverses. Bits with diameters from 150 to 250 nm exhibit "negative" switching polarity. In this material system, it has been observed that the switching polarity depends on the direction of the PMA gradient [29], but in this study, the direction of the PMA gradient was not changed. The observed clocking at 50 nm diameter and reversed polarity at 100 nm diameter are likely due to an interplay between the size-dependent demagnetization energy and the DMI + PMA gradient symmetry breaking mechanism. In the case of clocking at the 50 nm diameter size, this behavior is attributed to the relative magnitude difference between the overall anisotropy in the system (K_{PMA} - K_{demag} = 6 x 10^5 J/m^3 – 5.1 x 10^5 J/m^3 = 9 x 10^4 J/m^3), and the PMA gradient (5.05 J/m^3 per nm). It is posited that this relative magnitude difference between overall anisotropy and PMA gradient (5.05 / 9E4 = 0.0056%) results in a case where the gradient is not large enough to enable deterministic switching, leading to the observed clocking. For comparison, the relative magnitude of the PMA gradient in the 250 nm bit is 0.0112% (5.05 / 6E5 – 5.55E5 = 5.05 / 4.5E4 = 0.0112%), which is double that seen in the 50 nm bit.

Regarding the reversed polarity seen between the 100 nm and > 150 nm bits, this behavior is attributed to the relative magnitude and direction difference between PMA energy density and demagnetization energy density. We have seen in [29] that the switching polarity is strongly influenced by direction of the PMA gradient. In the 100 nm bit, the PMA energy density is ~6 x 10^5 J/m^3 larger than demagnetization energy density. In this regime, OOP PMA dominates over IP demag, such that the deterministic switching polarity is determined by the relative orientations between the PMA gradient and OOP PMA axis. On the other hand, in the larger magnetic bits, the difference between PMA and demag energy is smaller such that it is both the relative orientation between PMA gradient and OOP PMA axis, as well as the relative

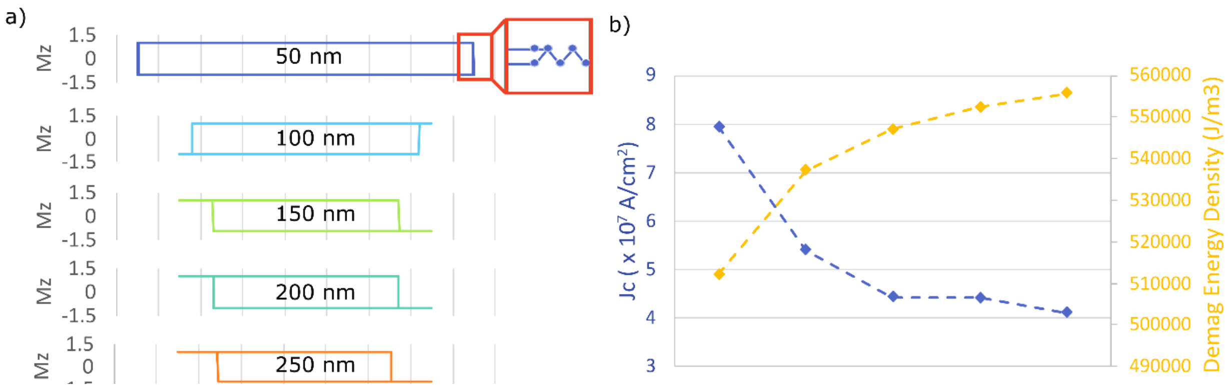

Figure 4-3. a) Size-dependent current induced hysteresis loops. b) Dependence of critical switching current Jc and Demagnetization energy density on magnetic bit size.

orientation between PMA gradient and IP demagnetization field, that determines switching polarity.

Figure 4-4 plots SOT switching results for the DMI-mediated field free switching system with 100 nm diameter and the addition of in-plane strain. These results are broken down by the relative angle between the applied strain and the PMA gradient. Figure 4-4a shows current-induced hysteresis loops for pure SOT switching, and SOT switching in the presence of 1000 με applied along the y-axis (parallel to PMA gradient). The addition of 1000 με strain parallel to the PMA gradient reduces Jc from 5.4 x 10^7 A/cm^2 in the pure-SOT case, to 4.5 x 10^7 A/cm^2, a 17% reduction. When the strain is applied along the x-axis (90° from the PMA gradient), shown in Figure 4-4b, there is no effect on Jc, the critical switching current is the same with or without the applied strain. In Figure 4-4c and d, m_z is plotted as a function of time for four different SOT current densities (+/- 3.15 x 10^7 and +/- 6.00 x 10^7 A/cm^2) and two different initialization states (+m_z and - m_z). For strain applied at 45° from the PMA gradient, no matter what current polarity is applied, or what state the magnetization is initialized in, the final state is +m_z. Conversely with the strain applied at 135° from the PMA gradient, the opposite behavior is exhibited. No matter what polarity of current is applied or what state the magnetization is initialized in, the final state is in the -m_z direction. For both the 45° and 135° cases, the critical current needed to induce switching was 3.15 x 10^7 A/cm^2, a 42% reduction compared to the pure-SOT case.

These results highlight several key factors involved with strain-assisted SOT switching in this DMI-mediated system. Firstly, the effect of strain on the critical switching current is highly anisotropic. Strain applied parallel to the PMA gradient assists the switching results in reduced critical current while strain applied perpendicular to the PMA gradient does not have any effect. This shows that there is more at play than simply the balance between PMA and in-plane (demag) anisotropy, as suggested in above paragraphs. If this were the case, strain applied perpendicular to the PMA gradient should show a similar effect as strain applied parallel. The DMI mediated symmetry breaking that allows deterministic switching depends on the formation of a magnetization gradient in the y-direction, as this produces the DMI effective field H_{DMI} in both the in-plane and OOP directions. Strain along the y-direction assists this process, while strain along the x-direction only produces two oppositely oriented effective fields that cancel each other out. In the case of strain applied at 45° and 135° from the PMA gradient axis, switching in these cases becomes deterministic with strain, as opposed to SOT (SOT polarity does not determine switching direction). This behavior, along with the significantly reduced Jc value, is attributed to the term in the z-component of the DMI effective field, $-\frac{\partial m_y}{\partial y} - \frac{\partial m_x}{\partial x}$. With contributions from magnetization gradients in both the x and y directions, the magnitude of this z-component is larger than compared to a gradient in the y-direction alone, resulting in a smaller critical switching current needed to induce switching between +/- m_z states. Regarding the polarity of switching, the observed results indicate that with strain applied at the 45° angle, magnetization textures in which both $\frac{\partial m_y}{\partial y}$ and $\frac{\partial m_x}{\partial x}$ are negative are preferentially produced, whereas with strain applied at 135°, textures with positive $\frac{\partial m_y}{\partial y}$ and $\frac{\partial m_x}{\partial x}$ are preferentially produced. Overall, these results show the potential for significant reduction in critical switching current by addition of in-plane strain, as well as the critical importance of considering the directionality of each component in the DMI-mediated SOT switching system.

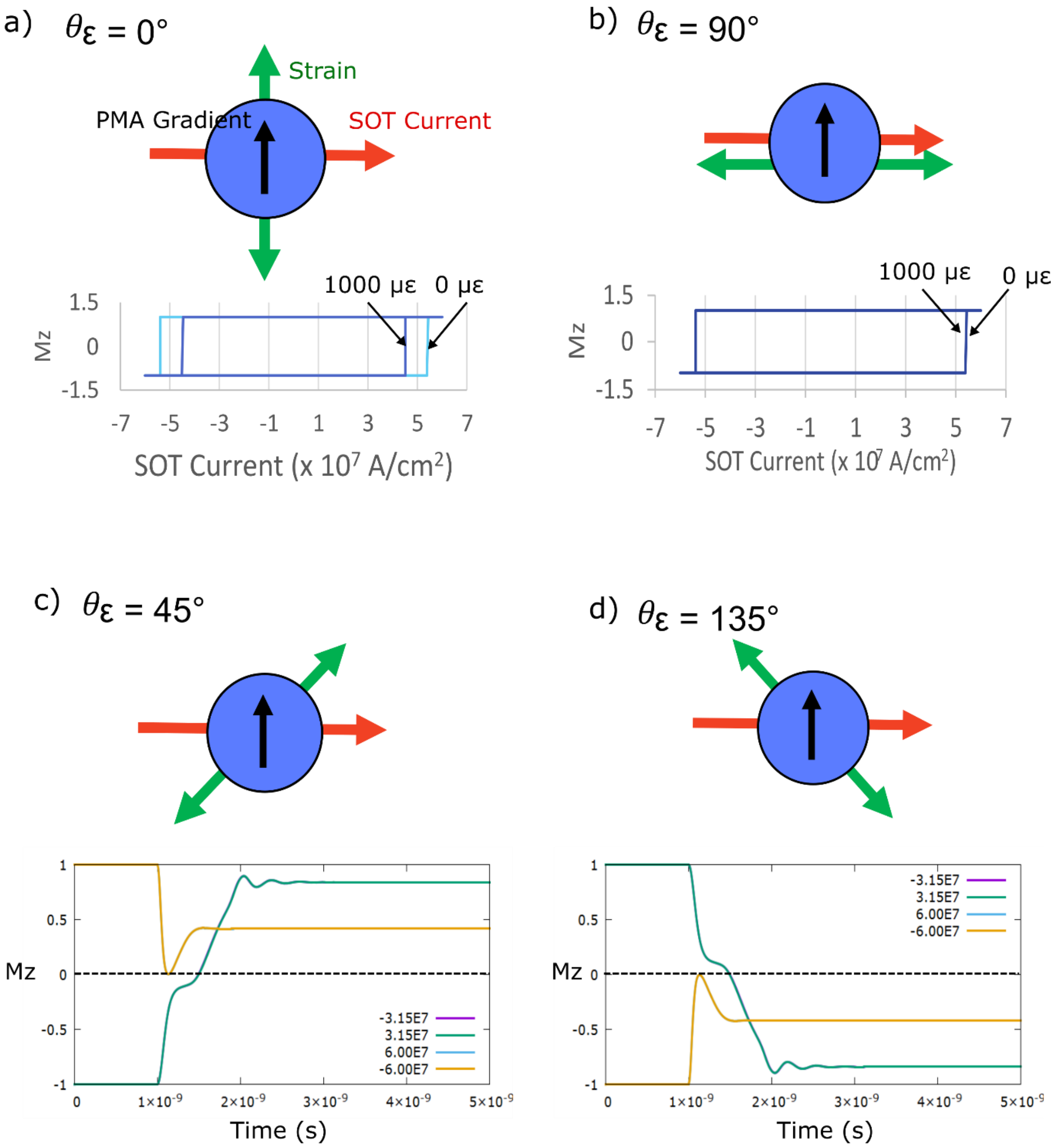

Figure 4-4. a, b) Current induced hysteresis loops for both 0 strain, and 1000 microstrain applied at 0 and 90 degree angles relative to the PMA gradient. c,d) z-component of magnetization plotted vs. time for 1000 microstrain applied at 45 and 135 degree angles to PMA gradient.

Figure 4-5 plots the y-component of magnetization as a function of time from five different initial states (0°, +0.06° x, -0.06° x, +0.06° y, -0.06° y), under four different conditions: a) in the absence of any external or effective field other than strain and PMA, b) in the presence of a 5 Oe external field applied along the x-axis, c) in the presence of a 9 x 10^5 A/cm^2 SOT current applied along the y-axis, and d) in the DMI + PMA gradient material system, with D_{ij} = 1 x 10^{-3} J/m^2 and with a PMA gradient of 20 J/m^3 per nm in the y-direction. In Figure 4-5a, the cases with +0.06° x and +0.06° y initializations flip to the +m_y direction, while the remaining three flip to the -m_y direction. In Figure 4-5b and c, the magnetization flips to the -m_y for each initialization case, and in Figure 4-5d, the magnetization flips to the +m_y direction for each initialization case.

These results show that in the same way an in-plane external field can break PMA symmetry for deterministic SOT switching, an in-plane external or effective field can break the symmetry of an applied strain anisotropy. For the case with no external or effective field, the uniaxial anisotropy associated with the applied strain has equal chance to flip the magnetization to +my or -my states, and upon removal of the strain, the magnetization has equal chance to return to +mz or flip to -mz states, due to the symmetry of PMA. In this scenario, strain-induced clocking is impossible. By addition of a small external or effective field (such as those induced by SOT or DMI), control over the direction of strain-induced switching becomes possible, enabling controllable strain clocking. In the case of external field, when the magnetization is aligned along +mz, the external field in the x-direction applies torque on the magnetization towards the -my direction, as evidenced by Figure 4-5b. Similarly with a small SOT current (2 orders of magnitude lower than is required for SOT-mediated switching), the field-like torque pushes the magnetization to the -my state. With this SOT current, the chirality of clocking can be controlled by the polarity of the current, enabling directional clocking as well as deterministic switching (with a pre-read required). Finally, in the case of DMI + PMA gradient, the DMI coefficient and gradient used in previous studies (based on material system here [29]) did not produce large enough effective field to enable consistent clocking. The DMI coefficient was increased from 5 x 10^{-5} to 1 x 10^{-3} J/m^2 (close in magnitude to that of a Pt/Co system), and the PMA gradient was increased from 5.05 J/m^3 per nm to 20 J/m^3 per nm. With these parameters, ultra-low energy clocking in the absence of external field or electric current can be achieved.

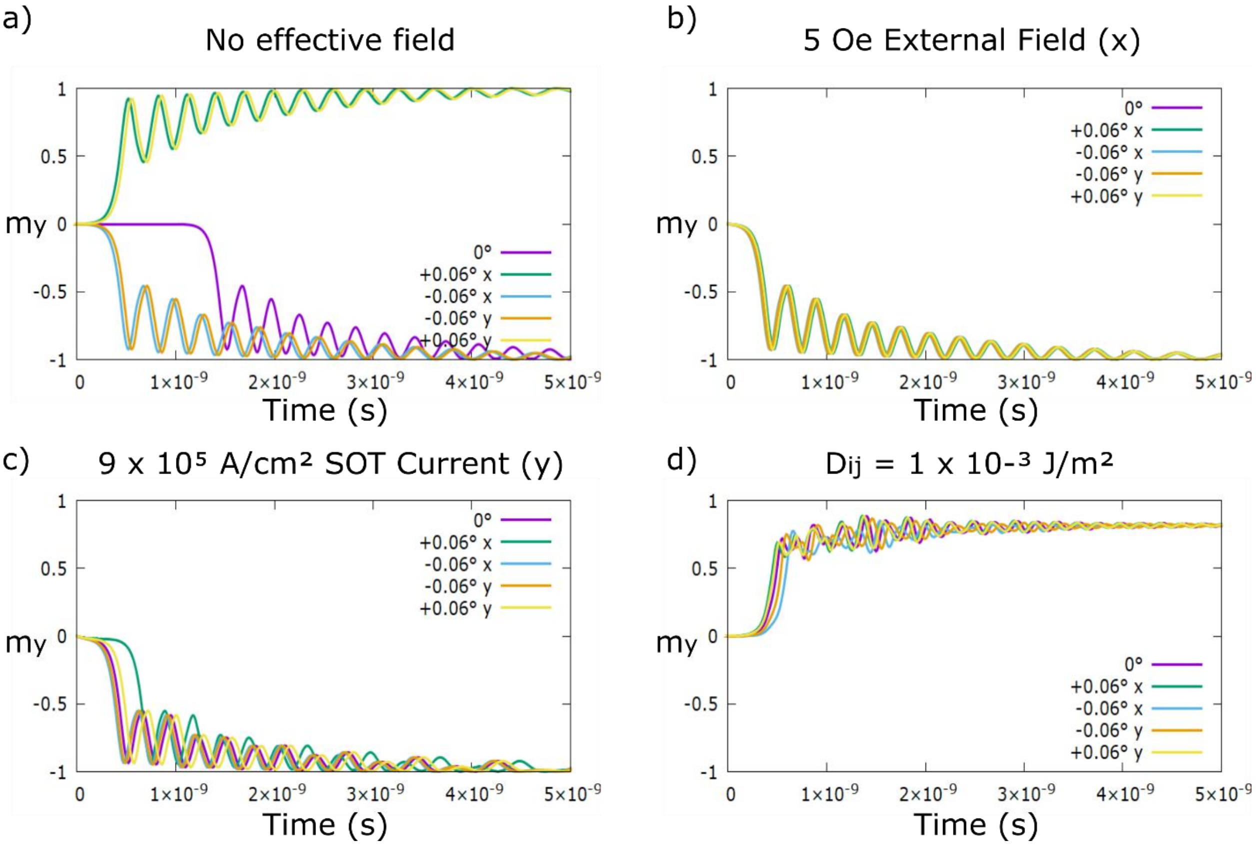

Figure 4-5. Y-component of magnetization in magnetic elements with PMA under influence of strain anisotropy applied in the y-axis. Comparison of strain-symmetry breaking mechanisms a) no symmetry breaking, b) external field in x-direction, c) SOT current in y-direction, and d) intrinsic DMI + PMA gradient

4.4 Conclusion

In conclusion, the dependence of critical SOT switching current in DMI-mediated SOT switching systems on magnetic bit size as well as applied strain direction was studied with the goal of reducing critical SOT switching current. It was found that switching current Jc increases significantly with decreasing bit size (Jc for 50 nm bit is double that for 250 nm bit), and that bit size can influence switching polarity. Regarding the application of strain for strain-assisted SOT switching, the direction of applied strain is critical. Strain applied perpendicular to the PMA gradient produced no effect on Jc, while strain parallel to the gradient reduced Jc by 17%. At intermediate angles of applied strain (45° and 135°), the critical current is further reduced (42%) and the switching becomes deterministic with applied strain direction rather than with SOT current polarity. Finally, three different mechanisms were studied to enable low-energy strain symmetry breaking for strain-mediated clocking. The presence of a small effective field perpendicular to the applied anisotropy (whether it be strain or PMA) breaks the symmetry of the uniaxial anisotropy to enable direction controllable clocking. These results demonstrate the ability to improve energy efficiency of SOT-based switching devices through the addition of strain, as well as demonstrate the potential for ultra-low energy, strain-only control of perpendicular magnetization.

5 Dissertation Conclusion

The work outlined in this dissertation covers three broad fields, computer image recognition, neuromorphic computing, and magnetic memory. In each of these fields, challenges faced by the current state of the art are addressed by investigation of new magnetic materials, new magnetic actuation methods, and new dynamic excitation schemes. The contributions to each field that are discussed in this dissertation are outlined below:

Image Recognition: The dependence of dipole coupling strength on nanomagnetic array dimensions was determined, as well the effect of element dimensions and dipole coupling on magnetic ground states. By varying the rate at which SOT was applied to a nanodisk within a dipole coupled array, the influence of that disk's stray field on the relaxation process of neighboring disks was negated.

Neuromorphic Computing: A proof of concept for a four-state AFM synapse was demonstrated, in which strain pulses successfully programmed non-volatile intermediate AFM magnetization states into an AFM nanowire. By varying the rate at which the strain pulses were applied, the upper bound for programming speed and its dependence on AFM resonance was determined.

Magnetic Memory: The dependence of critical SOT switching current on magnetic bit size was determined, and the potential for strain-assisted reduction in critical switching current was investigated, with results showing a significant improvement in switching current that is direction-dependent. In addition, a concept for ultra-low energy, direction controllable strain clocking was demonstrated.

While each of these fields are fairly disparate, the core concepts studied here represent promising steps forward, not just in these particular applications, but in any application utilizing magnetic phenomena. Antiferromagnetics have the potential to speed up magnetic systems by orders of magnitude, while multiferroic structures hold the potential to improve energy efficiency by the same amount. And finally, investigating and utilizing the dynamics involved in magnetic excitation can lead to improvements in both speed and energy.

6 References

[1] K. L. Wang, J. G. Alzate, and P. Khalili Amiri, “Low-power non-volatile spintronic memory: STT-RAM and beyond,” *J. Phys. D. Appl. Phys.*, vol. 46, no. 8, 2013, doi: 10.1088/0022-3727/46/7/074003.

[2] K. A. Roxy and S. Bhanja, “Reading nanomagnetic energy minimizing coprocessor,” *IEEE Trans. Nanotechnol.*, vol. 17, no. 2, pp. 368–372, 2018, doi: 10.1109/TNANO.2018.2795480.

[3] “HDD areal density reaches 1 terabit/sq. in.,” *Computer History Museum*. https://www.computerhistory.org/storageengine/hdd-areal-density-reaches-1-terabit-sq-in/ (accessed Sep. 10, 2020).

[4] A. Marashi, “Improving Data Center Power Consumption & Energy Efficiency.” https://www.vxchnge.com/blog/growing-energy-demands-of-data-centers (accessed Sep. 11, 2020).

[5] C. Chappert, A. Fert, and F. N. Van Dau, “The emergence of spin electronics in data storage,” *Nat. Mater.*, vol. 6, no. 11, pp. 813–823, 2007, doi: 10.1038/nmat2024.

[6] S. Bhatti, R. Sbiaa, A. Hirohata, H. Ohno, S. Fukami, and S. N. Piramanayagam, “Spintronics based random access memory: a review,” *Mater. Today*, vol. 20, no. 9, pp. 530–548, 2017, doi: 10.1016/j.mattod.2017.07.007.

[7] U. Gradmann and J. Müller, “Flat Ferromagnetic, Epitaxial 48Ni/52Fe(111) Films of few Atomic Layers,” *Phys. Status Solidi*, vol. 27, no. 1, pp. 313–324, 1968, doi: 10.1002/pssb.19680270133.

[8] S. Ikeda *et al.*, “Tunnel magnetoresistance of 604% at 300 K by suppression of Ta diffusion in CoFeBMgOCoFeB pseudo-spin-valves annealed at high temperature,” *Appl. Phys. Lett.*, vol. 93, no. 8, pp. 1–4, 2008, doi: 10.1063/1.2976435.

[9] M. Endo, S. Kanai, S. Ikeda, F. Matsukura, and H. Ohno, “Electric-field effects on thickness dependent magnetic anisotropy of sputtered MgO/Co40Fe40B20/Ta structures,” *Appl. Phys. Lett.*, vol. 96, no. 21, pp. 10–13, 2010, doi: 10.1063/1.3429592.

[10] S. Ikeda *et al.*, “A perpendicular-anisotropy CoFeB-MgO magnetic tunnel junction,” *Nat. Mater.*, vol. 9, no. 9, pp. 721–724, 2010, doi: 10.1038/nmat2804.

[11] A. P. Guimarães, *Principles of Nanomagnetism*. 2009.

[12] J. C. Slonczewski, “Current-driven excitation of magnetic multilayers,” *J. Magn. Magn. Mater.*, vol. 159, no. 1–2, 1996, doi: 10.1016/0304-8853(96)00062-5.

[13] “Spin Transfer Torque | QuantumATK R-2020.09 Documentation.” http://docs.quantumatk.com/tutorials/spin_transfer_torque/spin_transfer_torque.html (accessed Sep. 14, 2020).

[14] F. J. Albert, J. A. Katine, R. A. Buhrman, and D. C. Ralph, “Spin-polarized current switching of a Co thin film nanomagnet,” *Appl. Phys. Lett.*, vol. 77, no. 23, pp. 3809–3811, 2000, doi: 10.1063/1.1330562.

[15] H. Meng *et al.*, “Low current density induced spin-transfer torque switching in CoFeB-MgO magnetic tunnel junctions with perpendicular anisotropy,” *J. Phys. D. Appl. Phys.*, vol. 44, no. 40, 2011, doi: 10.1088/0022-3727/44/40/405001.

[16] G. Panagopoulos, C. Augustine, and K. Roy, “Modeling of dielectric breakdown-induced time-dependent STT-MRAM performance degradation,” *Device Res. Conf. - Conf. Dig. DRC*, pp. 125–126, 2011, doi: 10.1109/DRC.2011.5994447.

[17] M. I. Dyakonov and V. I. Perel, “Current-induced spin orientation of electrons in semiconductors,” *Phys. Lett. A*, vol. 35, no. 6, pp. 459–460, 1971, doi: 10.1016/0375-9601(71)90196-4.

[18] J. E. Hirsch, “Spin Hall Effect,” *Phys. Rev. Lett.*, vol. 83, no. 9, pp. 1834–1837, 1999, doi: 10.1016/B978-0-44-453153-7.00061-4.

[19] Y. Kajiwara *et al.*, “Transmission of electrical signals by spin-wave interconversion in a magnetic insulator,” *Nature*, vol. 464, no. 7286, pp. 262–266, 2010, doi: 10.1038/nature08876.

[20] L. Liu, O. J. Lee, T. J. Gudmundsen, D. C. Ralph, and R. A. Buhrman, “Magnetic switching by spin torque from the spin Hall effect,” 2011, doi: 10.1103/PhysRevLett.109.096602.

[21] L. Liu, C. F. Pai, Y. Li, H. W. Tseng, D. C. Ralph, and R. A. Buhrman, “Spin-torque switching with the giant spin hall effect of tantalum,” *Science (80-.).*, vol. 336, no. 6081, pp. 555–558, 2012, doi: 10.1126/science.1218197.

[22] Y. Fan *et al.*, “Magnetization switching through giant spin-orbit torque in a magnetically doped topological insulator heterostructure,” *Nat. Mater.*, vol. 13, no. 7, pp. 699–704, 2014, doi: 10.1038/nmat3973.

[23] A. Van Den Brink *et al.*, “Field-free magnetization reversal by spin-Hall effect and exchange bias,” *Nat. Commun.*, vol. 7, pp. 1–6, 2016, doi: 10.1038/ncomms10854.

[24] Y. W. Oh *et al.*, “Field-free switching of perpendicular magnetization through spin-orbit torque in antiferromagnet/ferromagnet/oxide structures,” *Nat. Nanotechnol.*, vol. 11, no. 10, pp. 878–884, 2016, doi: 10.1038/nnano.2016.109.

[25] Z. Zhao, A. K. Smith, M. Jamali, and J. P. Wang, “External-Field-Free Spin Hall Switching of Perpendicular Magnetic Nanopillar with a Dipole-Coupled Composite Structure,” *Adv. Electron. Mater.*, no. 612, 2020, doi: 10.1002/aelm.201901368.

[26] L. You *et al.*, “Switching of perpendicularly polarized nanomagnets with spin orbit torque without an external magnetic field by engineering a tilted anisotropy,” *Proc. Natl. Acad. Sci. U. S. A.*, vol. 112, no. 33, pp. 10310–10315, 2015, doi: 10.1073/pnas.1507474112.

[27] G. Yu *et al.*, “Switching of perpendicular magnetization by spin-orbit torques in the absence of external magnetic fields,” *Nat. Nanotechnol.*, vol. 9, no. 7, pp. 548–554, 2014, doi: 10.1038/nnano.2014.94.

[28] G. Yu *et al.*, “Current-driven perpendicular magnetization switching in Ta/CoFeB/[TaOxor MgO/TaOx] films with lateral structural asymmetry,” *Appl. Phys. Lett.*, vol. 105, no. 10, 2014, doi: 10.1063/1.4895735.

[29] H. Wu *et al.*, “Chiral Symmetry Breaking for Deterministic Switching of Perpendicular Magnetization by Spin-Orbit Torque,” *Prepr. à Ref.*, vol. 21, no. 1, pp. 515–521, 2021, doi: 10.1021/acs.nanolett.0c03972.

[30] I. Dzyaloshinsky, “A Thermodynamic Theory of ‘Weak’ Ferromagnetism of Antiferromagnetics,” *J. Phys. Chem. Solids*, vol. 4, no. 2, pp. 241–255, 1958, doi: 10.1002/pssb.2220460236.

[31] T. Moriya, “Anisotropic superexchange interaction and weak ferromagnetism,” *Phys. Rev.*, vol. 120, no. 1, pp. 91–98, 1960, doi: 10.1103/PhysRev.120.91.

[32] S. Mühlbauer *et al.*, “Skyrmion lattice in a chiral magnet,” *Science (80-.).*, vol. 323, no. 5916, pp. 915–919, 2009, doi: 10.1126/science.1166767.

[33] X. Z. Yu *et al.*, “Real-space observation of a two-dimensional skyrmion crystal,” *Nature*, vol. 465, no. 7300, pp. 901–904, 2010, doi: 10.1038/nature09124.

[34] A. Fert, N. Reyren, and V. Cros, "Magnetic skyrmions: Advances in physics and potential applications," *Nat. Rev. Mater.*, vol. 2, 2017, doi: 10.1038/natrevmats.2017.31.

[35] Z. Luo *et al.*, "Chirally coupled nanomagnets," *Science (80-.).*, vol. 363, no. 6434, pp. 1435–1439, 2019, doi: 10.1126/science.aau7913.

[36] A. Fernández-Pacheco, E. Vedmedenko, F. Ummelen, R. Mansell, D. Petit, and R. P. Cowburn, "Symmetry-breaking interlayer Dzyaloshinskii–Moriya interactions in synthetic antiferromagnets," *Nat. Mater.*, vol. 18, no. 7, pp. 679–684, 2019, doi: 10.1038/s41563-019-0386-4.

[37] X. Ma *et al.*, "Interfacial control of Dzyaloshinskii-Moriya interaction in heavy metal/ferromagnetic metal thin film heterostructures," *Phys. Rev. B*, vol. 94, no. 18, 2016, doi: 10.1103/PhysRevB.94.180408.

[38] M. Fiebig, "Revival of the magnetoelectric effect," *J. Phys. D. Appl. Phys.*, vol. 38, no. 8, 2005, doi: 10.1088/0022-3727/38/8/R01.

[39] J. D. Schneider *et al.*, "Experimental demonstration and operating principles of a multiferroic antenna," *J. Appl. Phys.*, vol. 126, no. 22, 2019, doi: 10.1063/1.5126047.

[40] J. P. Domann, C. Chen, A. E. Sepulveda, R. N. Candler, and G. P. Carman, "Multiferroic Micro-Motors with Deterministic Single Input Control," pp. 1–25, 2018, [Online]. Available: http://arxiv.org/abs/1802.09420.

[41] C. Chen *et al.*, "Voltage manipulation of magnetic particles using multiferroics," *J. Phys. D. Appl. Phys.*, vol. 53, no. 17, 2020, doi: 10.1088/1361-6463/ab7038.

[42] M. Liu *et al.*, "Giant electric field tuning of magnetic properties in multiferroic ferrite/ferroelectric heterostructures," *Adv. Funct. Mater.*, vol. 19, no. 11, pp. 1826–1831, 2009, doi: 10.1002/adfm.200801907.

[43] T. Wu *et al.*, "Giant electric-field-induced reversible and permanent magnetization reorientation on magnetoelectric Ni/(011) [Pb (Mg1/3 Nb 2/3) O3](1-x) - [PbTiO3] x heterostructure," *Appl. Phys. Lett.*, vol. 98, no. 1, pp. 2009–2012, 2011, doi: 10.1063/1.3534788.

[44] S. Zhang *et al.*, "Electric-field control of nonvolatile magnetization in Co 40Fe 40B 20/Pb(Mg 1/3Nb 2/3) 0.7Ti 0.3O 3 structure at room temperature," *Phys. Rev. Lett.*, vol. 108, no. 13, pp. 1–5, 2012, doi: 10.1103/PhysRevLett.108.137203.

[45] M. Buzzi *et al.*, "Single domain spin manipulation by electric fields in strain coupled artificial multiferroic nanostructures," *Phys. Rev. Lett.*, vol. 111, no. 2, pp. 1–5, 2013, doi: 10.1103/PhysRevLett.111.027204.

[46] K. Cai *et al.*, "Electric field control of deterministic current-induced magnetization switching in a hybrid ferromagnetic/ferroelectric structure," *Nat. Mater.*, vol. 16, no. 7, pp. 712–716, 2017, doi: 10.1038/nmat4886.

[47] Q. Wang, J. Domann, G. Yu, A. Barra, K. L. Wang, and G. P. Carman, "Strain-Mediated Spin-Orbit-Torque Switching for Magnetic Memory," *Phys. Rev. Appl.*, vol. 10, no. 3, pp. 1–29, 2018, doi: 10.1103/PhysRevApplied.10.034052.

[48] D. B. Gopman *et al.*, "Strain-assisted magnetization reversal in Co/Ni multilayers with perpendicular magnetic anisotropy," *Sci. Rep.*, vol. 6, no. June, pp. 1–8, 2016, doi: 10.1038/srep27774.

[49] S. Noh, D. H. Kang, and M. Shin, "Simulation of Strain-Assisted Switching in Synthetic Antiferromagnetic Free Layer-Based Magnetic Tunnel Junction," *IEEE Trans. Magn.*, vol. 55, no. 4, 2019.

[50] A. Khan, D. E. Nikonov, S. Manipatruni, T. Ghani, and I. A. Young, "Voltage induced

magnetostrictive switching of nanomagnets: Strain assisted strain transfer torque random access memory," *Appl. Phys. Lett.*, vol. 104, no. 26, 2014, doi: 10.1063/1.4884419.

[51] Q. Wang *et al.*, "Strain-mediated 180° switching in CoFeB and Terfenol-D nanodots with perpendicular magnetic anisotropy," *Appl. Phys. Lett.*, vol. 110, no. 10, pp. 1–6, 2017, doi: 10.1063/1.4978270.

[52] X. Li *et al.*, "Strain-mediated 180° perpendicular magnetization switching of a single domain multiferroic structure," *J. Appl. Phys.*, vol. 118, no. 1, 2015, doi: 10.1063/1.4923350.

[53] J. G. Alzate *et al.*, "Voltage-induced switching of nanoscale magnetic tunnel junctions," *Tech. Dig. - Int. Electron Devices Meet. IEDM*, pp. 681–684, 2012, doi: 10.1109/IEDM.2012.6479130.

[54] J. Larmor, "On the theory of the magnetic influence on spectra; and on the radiation from moving ions," *London, Edinburgh, Dublin Philos. Mag. J. Sci.*, vol. 44, no. 271, 1897.

[55] J. H. E. Griffiths, "Anomalous high-frequency resistance of ferromagnetic metals," *Nature*, vol. 158, no. 4019, pp. 670–671, 1946, doi: 10.1038/158670a0.

[56] C. Kittel, "On the theory of ferromagnetic resonance absorption," *Phys. Rev.*, vol. 73, no. 2, pp. 155–161, 1948, doi: 10.1103/PhysRev.73.155.

[57] K. Mizunuma *et al.*, "Size dependence of magnetic properties of nanoscale CoFeB-MgO magnetic tunnel junctions with perpendicular magnetic easy axis observed by ferromagnetic resonance," *Appl. Phys. Express*, vol. 6, no. 6, 2013, doi: 10.7567/APEX.6.063002.

[58] M. L. Néel, "Propriétés magnétiques des ferrites ; ferrimagnétisme et antiferromagnétisme," *Ann. Phys. (Paris).*, vol. 12, no. 3, pp. 137–198, 1948, doi: 10.1051/anphys/194812030137.

[59] F. Keffer and C. Kittel, "Theory of antiferromagnetic resonance," *Phys. Rev.*, vol. 85, no. 2, pp. 329–337, 1952, doi: 10.1103/PhysRev.85.329.

[60] F. M. Johnson and A. H. Nethercot, "Antiferromagnetic resonance in MnF2," *Phys. Rev.*, vol. 114, no. 3, pp. 705–716, 1959, doi: 10.1103/PhysRev.114.705.

[61] A. Sievers and M. Tinkham, "Far infrared antiferromagnetic resonance in MnO and NiO," *Phys. Rev.*, vol. 129, no. 4, pp. 1566–1571, 1963, doi: 10.1103/PhysRev.129.1566.

[62] A. V. Kimel, A. Kirilyuk, A. Tsvetkov, R. V. Pisarev, and T. Rasing, "Laser-induced ultrafast spin reorientation in the antiferromagnet TmFeO3," *Nature*, vol. 429, no. 6994, pp. 850–853, 2004, doi: 10.1038/nature02659.

[63] Y. Hamakawa *et al.*, "Spin-valve heads utilizing antiferromagnetic NiO layers," *IEEE Trans. Magn.*, vol. 32, no. 1, pp. 149–155, 1996, doi: 10.1109/20.477565.

[64] Y. Sugita, Y. Kawawake, M. Satomi, and H. Sakakima, "Giant magnetoresistanc of dual spin-valves using antiferromagnetic α-Fe2O3 as a pinning layer," *Japanese J. Appl. Physics, Part 1 Regul. Pap. Short Notes Rev. Pap.*, vol. 37, no. 11, pp. 5984–5985, 1998, doi: 10.1143/jjap.37.5984.

[65] B. Dieny, M. Li, S. H. Liao, C. Horng, and K. Ju, "Quantitative interpretation of the magnetoresistive response (amplitude and shape) of spin valves with synthetic antiferromagnetic pinned layers," *J. Appl. Phys.*, vol. 87, no. 7, pp. 3415–3420, 2000, doi: 10.1063/1.372360.

[66] Z. Wei *et al.*, "Changing exchange bias in spin valves with an electric current," *Phys. Rev. Lett.*, vol. 98, no. 11, pp. 1–4, 2007, doi: 10.1103/PhysRevLett.98.116603.

[67] S. Urazhdin and N. Anthony, "Effect of polarized current on the magnetic state of an

antiferromagnet," *Phys. Rev. Lett.*, vol. 99, no. 4, pp. 3–6, 2007, doi: 10.1103/PhysRevLett.99.046602.

[68] P. Wadley *et al.*, "Spintronics: Electrical switching of an antiferromagnet," *Science (80-.).*, vol. 351, no. 6273, pp. 587–590, 2016, doi: 10.1126/science.aab1031.

[69] B. G. Park *et al.*, "A spin-valve-like magnetoresistance of an antiferromagnet-based tunnel junction," *Nat. Mater.*, vol. 10, no. 5, pp. 347–351, 2011, doi: 10.1038/nmat2983.

[70] X. Marti *et al.*, "Room-temperature antiferromagnetic memory resistor," *Nat. Mater.*, vol. 13, no. 4, pp. 367–374, 2014, doi: 10.1038/nmat3861.

[71] A. B. Shick, S. Khmelevskyi, O. N. Mryasov, J. Wunderlich, and T. Jungwirth, "Spin-orbit coupling induced anisotropy effects in bimetallic antiferromagnets: A route towards antiferromagnetic spintronics," *Phys. Rev. B - Condens. Matter Mater. Phys.*, vol. 81, no. 21, pp. 1–4, 2010, doi: 10.1103/PhysRevB.81.212409.

[72] E. Plekhanov, A. Stroppa, and S. Picozzi, "Magneto-electric coupling in antiferromagnet/ferroelectric Mn2Au/BaTiO3 interface," *J. Appl. Phys.*, vol. 120, no. 7, 2016, doi: 10.1063/1.4961213.

[73] A. A. Sapozhnik *et al.*, "Manipulation of antiferromagnetic domain distribution in Mn2Au by ultrahigh magnetic fields and by strain," *Phys. Status Solidi - Rapid Res. Lett.*, vol. 11, no. 4, pp. 9–12, 2017, doi: 10.1002/pssr.201600438.

[74] S. Polisetty, W. Echtenkamp, K. Jones, X. He, S. Sahoo, and C. Binek, "Piezoelectric tuning of exchange bias in a BaTiO3/CoCoO heterostructure," *Phys. Rev. B - Condens. Matter Mater. Phys.*, vol. 82, no. 13, pp. 1–7, 2010, doi: 10.1103/PhysRevB.82.134419.

[75] S. Z. Wu *et al.*, "Strain-mediated electric-field control of exchange bias in a Co90Fe10/BiFeO3/SrRuO3/PMN-PT heterostructure," *Sci. Rep.*, vol. 5, pp. 1–5, 2015, doi: 10.1038/srep08905.

[76] P. Li, C. Zhou, C. Cao, W. Wang, and C. Jiang, "Electric-field control of non-volatile 180° switching of the unidirectional anisotropy field in a multiferroic heterostructure," *Phys. Chem. Chem. Phys.*, vol. 20, no. 40, pp. 25854–25860, 2018, doi: 10.1039/c8cp05106b.

[77] X. Chen *et al.*, "Electric field switching of the uniaxial magnetic anisotropy of an antiferromagnet," pp. 1–13, 2018, [Online]. Available: http://arxiv.org/abs/1812.11868.

[78] H. Yan *et al.*, "A piezoelectric, strain-controlled antiferromagnetic memory insensitive to magnetic fields," *Nat. Nanotechnol.*, vol. 14, no. 2, pp. 131–136, 2019, doi: 10.1038/s41565-018-0339-0.

[79] A. Barra, J. Domann, K. W. Kim, and G. Carman, "Voltage Control of Antiferromagnetic Phases at Near-Terahertz Frequencies," *Phys. Rev. Appl.*, vol. 9, no. 3, p. 34017, 2018, doi: 10.1103/PhysRevApplied.9.034017.

[80] G. Csaba, M. Pufall, W. Rippard, and W. Porod, "Modeling of coupled spin torque oscillators for applications in associative memories," *Proc. IEEE Conf. Nanotechnol.*, pp. 23–26, 2012, doi: 10.1109/NANO.2012.6322201.

[81] V. Calayir and L. Pileggi, "Fully-digital oscillatory associative memories enabled by non-volatile logic," *Proc. Int. Jt. Conf. Neural Networks*, 2013, doi: 10.1109/IJCNN.2013.6706925.

[82] G. Srinivasan, A. Sengupta, and K. Roy, "Magnetic Tunnel Junction Based Long-Term Short-Term Stochastic Synapse for a Spiking Neural Network with On-Chip STDP Learning," *Sci. Rep.*, vol. 6, no. February, pp. 1–13, 2016, doi: 10.1038/srep29545.

[83] A. Imre, G. Csaba, L. Ji, A. Orlov, G. H. Bernstein, and W. Porod, "Majority Logic Gate

for Magnetic Quantum-Dot Cellular Automata," *Science (80-.).*, vol. 311, no. January, pp. 205–209, 2006, doi: 10.7551/mitpress/8053.003.0075.

[84] R. Faria, K. Y. Camsari, and S. Datta, "Low-Barrier Nanomagnets as p-Bits for Spin Logic," *IEEE Magn. Lett.*, vol. 8, 2017, doi: 10.1109/LMAG.2017.2685358.

[85] M. Becherer, G. Csaba, R. Emling, W. Porod, P. Lugli, and D. Schmitt-Landsiedel, "Field-Coupled Nanomagnets for Interconnect-Free Nonvolatile Computing," in *IEEE International Solid-State Circuits Conference*, 2009, pp. 474–475.

[86] S. Bhanja, D. K. Karunaratne, R. Panchumarthy, S. Rajaram, and S. Sarkar, "Non-Boolean computing with nanomagnets for computer vision applications," *Nat. Nanotechnol.*, vol. 11, no. 2, pp. 177–183, 2016, doi: 10.1038/nnano.2015.245.

[87] R. P. Cowburn, "Property variation with shape in magnetic nanoelements," *J. Phys. D. Appl. Phys.*, vol. 33, no. 1, 2000, doi: 10.1088/0022-3727/33/1/201.

[88] Y. Liu, D. Zhang, G. Lu, and W. Y. Ma, "A survey of content-based image retrieval with high-level semantics," *Pattern Recognit.*, vol. 40, no. 1, pp. 262–282, 2007, doi: 10.1016/j.patcog.2006.04.045.

[89] Q. Iqbal and J. K. Aggarwal, "Retrieval by classification of images containing large manmade objects using perceptual grouping," *Pattern Recognit.*, vol. 35, no. 7, pp. 1463–1479, 2002, doi: 10.1016/S0031-3203(01)00139-X.

[90] P. A. Larsen, J. B. Rawlings, and N. J. Ferrier, "Model-based object recognition to measure crystal size and shape distributions from in situ video images," *Chem. Eng. Sci.*, vol. 62, no. 5, pp. 1430–1441, 2007, doi: 10.1016/j.ces.2006.11.018.

[91] E. Michaelsen, U. Soergel, and U. Thoennessen, "Perceptual grouping for automatic detection of man-made structures in high-resolution SAR data," *Pattern Recognit. Lett.*, vol. 27, no. 4, pp. 218–225, 2006, doi: 10.1016/j.patrec.2005.08.002.

[92] H. Hoffmann and F. Steinbauer, "Single domain and vortex state in ferromagnetic circular nanodots," *J. Appl. Phys.*, vol. 92, no. 9, pp. 5463–5467, 2002, doi: 10.1063/1.1510559.

[93] S. Rajaram, D. K. Karunaratne, S. Sarkar, and S. Bhanja, "Study of dipolar neighbor interaction on magnetization states of nano-magnetic disks," *IEEE Trans. Magn.*, vol. 49, no. 7, pp. 3129–3132, 2013, doi: 10.1109/TMAG.2013.2249051.

[94] I. M. Miron *et al.*, "Perpendicular switching of a single ferromagnetic layer induced by in-plane current injection," *Nature*, vol. 476, no. 7359, pp. 189–193, 2011, doi: 10.1038/nature10309.

[95] L. Liu, O. J. Lee, T. J. Gudmundsen, D. C. Ralph, and R. A. Buhrman, "Current-induced switching of perpendicularly magnetized magnetic layers using spin torque from the spin hall effect," *Phys. Rev. Lett.*, vol. 109, no. 9, pp. 1–5, 2012, doi: 10.1103/PhysRevLett.109.096602.

[96] S. Kaka, M. R. Pufall, W. H. Rippard, T. J. Silva, S. E. Russek, and J. A. Katine, "Mutual phase-locking of microwave spin torque nano-oscillators," *Nature*, vol. 437, no. 7057, pp. 389–392, 2005, doi: 10.1038/nature04035.

[97] D. Bhowmik, L. You, and S. Salahuddin, "Spin hall effect clocking of nanomagnetic logic without a magnetic field," *Nat. Nanotechnol.*, vol. 9, no. 1, pp. 59–63, 2014, doi: 10.1038/nnano.2013.241.

[98] J. Misra and I. Saha, "Artificial neural networks in hardware: A survey of two decades of progress," *Neurocomputing*, vol. 74, no. 1–3, pp. 239–255, 2010, doi: 10.1016/j.neucom.2010.03.021.

[99] M. Holler, S. Tam, H. Castro, and R. Benson, "Electrically trainable artificial neural

network (ETANN) with 10240 'floating gate' synapses," *IJCNN Int Jt Conf Neural Netw.*, pp. 191–196, 1989, doi: 10.1109/ijcnn.1989.118698.

[100] J. Liu, M. A. Brooke, and K. Hirotsu, "A CMOS Feedforward Neural-Network On-Chip Parallel Learning for Oscillation Cancellation," vol. 13, no. 5, pp. 1178–1186, 2002.

[101] M. Milev and M. Hristov, "Analog Implementation of ANN with Inherent Quadratic Nonlinearity of the Synapses," *IEEE Trans. Neural Networks*, vol. 14, no. 5, pp. 1187–1200, 2003, doi: 10.1109/TNN.2003.816369.

[102] S. H. Jo, K. H. Kim, and W. Lu, "Programmable resistance switching in nanoscale two-terminal devices," *Nano Lett.*, vol. 9, no. 1, pp. 496–500, 2009, doi: 10.1021/nl803669s.

[103] K. Seo *et al.*, "Analog memory and spike-timing-dependent plasticity characteristics of a nanoscale titanium oxide bilayer resistive switching device," *Nanotechnology*, vol. 22, no. 25, 2011, doi: 10.1088/0957-4484/22/25/254023.

[104] A. F. Vincent *et al.*, "Spin-transfer torque magnetic memory as a stochastic memristive synapse for neuromorphic systems," *IEEE Trans. Biomed. Circuits Syst.*, vol. 9, no. 2, pp. 166–174, 2015, doi: 10.1109/TBCAS.2015.2414423.

[105] K. Roy, S. Bandyopadhyay, and J. Atulasimha, "Energy dissipation and switching delay in stress-induced switching of multiferroic nanomagnets in the presence of thermal fluctuations," *J. Appl. Phys.*, vol. 112, no. 2, 2012, doi: 10.1063/1.4737792.

[106] A. C. Chavez, W. Y. Sun, J. Atulasimha, K. L. Wang, and G. P. Carman, "Voltage induced artificial ferromagnetic-antiferromagnetic ordering in synthetic multiferroics," *J. Appl. Phys.*, vol. 122, no. 22, 2017, doi: 10.1063/1.4997612.

[107] A. C. Chavez, J. D. Schneider, A. Barra, S. Tiwari, R. N. Candler, and G. P. Carman, "Voltage-Controlled Ferromagnetic Resonance of Dipole-Coupled Co40Fe40 B20 Nanoellipses," *Phys. Rev. Appl.*, vol. 12, no. 4, p. 1, 2019, doi: 10.1103/PhysRevApplied.12.044071.

[108] C. Y. Liang *et al.*, "Modeling of magnetoelastic nanostructures with a fully coupled mechanical-micromagnetic model," *Nanotechnology*, vol. 25, no. 43, 2014, doi: 10.1088/0957-4484/25/43/435701.

[109] J. Hu, J. P. Domann, C. Liang, S. Keller, G. P. Carman, and A. Sepulveda, "Incoherent Strain Mediated Multiferroic Bennett Clocking," pp. 1–11, 2020.

[110] D. Carlton *et al.*, "Investigation of defects and errors in nanomagnetic logic circuits," *IEEE Trans. Nanotechnol.*, vol. 11, no. 4, pp. 760–762, 2012, doi: 10.1109/TNANO.2012.2196445.

[111] D. Winters, M. A. Abeed, S. Sahoo, A. Barman, and S. Bandyopadhyay, "Reliability of Magnetoelastic Switching of Nonideal Nanomagnets with Defects: A Case Study for the Viability of Straintronic Logic and Memory," *Phys. Rev. Appl.*, vol. 12, no. 3, p. 1, 2019, doi: 10.1103/PhysRevApplied.12.034010.

[112] K. A. Roxy and S. Bhanja, "Variability tolerant reading of nanomagnetic energy minimizing co-processor," in *2017 IEEE 60th International Midwest Symposium on Circuits and Systems (MWSCAS)*, 2017.

[113] M. Cubukcu *et al.*, "Spin-orbit torque magnetization switching of a three-terminal perpendicular magnetic tunnel junction," *Appl. Phys. Lett.*, vol. 104, no. 4, 2014, doi: 10.1063/1.4863407.

[114] Y. C. Lau, D. Betto, K. Rode, J. M. D. Coey, and P. Stamenov, "Spin-orbit torque switching without an external field using interlayer exchange coupling," *Nat. Nanotechnol.*, vol. 11, no. 9, pp. 758–762, 2016, doi: 10.1038/nnano.2016.84.

[115] V. E. Demidov *et al.*, “Magnetic nano-oscillator driven by pure spin current,” *Nat. Mater.*, vol. 11, no. 12, pp. 1028–1031, 2012, doi: 10.1038/nmat3459.

[116] S. U. Jen *et al.*, “Magnetic and electrical properties of amorphous CoFeB films,” *J. Appl. Phys.*, vol. 99, no. 5, 2006, doi: 10.1063/1.2174113.

[117] S. Fukami, T. Anekawa, C. Zhang, and H. Ohno, “A spin-orbit torque switching scheme with collinear magnetic easy axis and current configuration,” *Nat. Nanotechnol.*, vol. 11, no. 7, pp. 621–625, 2016, doi: 10.1038/nnano.2016.29.

[118] A. Vansteenkiste, J. Leliaert, M. Dvornik, M. Helsen, F. Garcia-Sanchez, and B. Van Waeyenberge, “The design and verification of MuMax3,” *AIP Adv.*, vol. 4, no. 10, 2014, doi: 10.1063/1.4899186.

[119] R. P. Cowburn, D. K. Koltsov, A. O. Adeyeye, M. E. Welland, and D. M. Tricker, “Single-domain circular nanomagnets,” *Phys. Rev. Lett.*, vol. 83, no. 5, pp. 1042–1045, 1999, doi: 10.1103/PhysRevLett.83.1042.

[120] S. Sarkar and S. Bhanja, “Direct quadratic minimization using magnetic field-based computing,” *Proc. - IEEE Int. Work. Des. Test Nano Devices, Circuits Syst. NDCS 2008*, pp. 31–34, 2008, doi: 10.1109/NDCS.2008.13.

[121] J. Pulecio, S. Bhanja, and S. Sarkar, “An experimental demonstration of the viability of energy minimizing computing using nano-magnets,” *Proc. IEEE Conf. Nanotechnol.*, pp. 1038–1042, 2011, doi: 10.1109/NANO.2011.6144474.

[122] S. Sarkar and S. Bhanja, “Synthesizing energy minimizing quantum-dot cellular automata circuits for vision computing,” *2005 5th IEEE Conf. Nanotechnol.*, vol. 2, no. July, pp. 729–732, 2005, doi: 10.1109/NANO.2005.1500821.

[123] A. G. Del Molino, J. H. Lim, and A. H. Tan, “Predicting visual context for unsupervised event segmentation in continuous photo-streams,” *MM 2018 - Proc. 2018 ACM Multimed. Conf.*, pp. 10–17, 2018, doi: 10.1145/3240508.3240624.

[124] J. Hawkins and S. Ahmad, “Why Neurons Have Thousands of Synapses, a Theory of Sequence Memory in Neocortex,” *Front. Neural Circuits*, vol. 10, no. March, p. 23, 2016, doi: 10.3389/fncir.2016.00023.

[125] Y. Cui, S. Ahmad, and J. Hawkins, “Continuous online sequence learning with an unsupervised neural network model,” *Neural Comput.*, vol. 28, pp. 2474–2504, 2016, doi: 10.1162/NECO.

[126] S. N. Aakur and S. Sarkar, “A perceptual prediction framework for self supervised event segmentation,” *Proc. IEEE Comput. Soc. Conf. Comput. Vis. Pattern Recognit.*, vol. 2019-June, pp. 1197–1206, 2019, doi: 10.1109/CVPR.2019.00129.

[127] K. Van Pham and K. S. Min, “Non-ideal effects of memristor-CMOS hybrid circuits for realizing multiple-layer neural networks,” *Proc. - IEEE Int. Symp. Circuits Syst.*, vol. 2019-May, 2019, doi: 10.1109/ISCAS.2019.8702519.

[128] A. M. Zyarah and D. Kudithipudi, “Neuromorphic Architecture for the Hierarchical Temporal Memory,” *IEEE Trans. Emerg. Top. Comput. Intell.*, vol. 3, no. 1, pp. 4–14, 2019, doi: 10.1109/TETCI.2018.2850314.

[129] A. M. Zyarah and D. Kudithipudi, “Neuromemrisitive architecture of HTM with on-device learning and neurogenesis,” *ACM J. Emerg. Technol. Comput. Syst.*, vol. 15, no. 3, 2019, doi: 10.1145/3300971.

[130] K. L. Rice, T. M. Taha, and C. N. Vutsinas, “Hardware acceleration of image recognition through a visual cortex model,” *Opt. Laser Technol.*, vol. 40, no. 6, pp. 795–802, 2008, doi: 10.1016/j.optlastec.2007.12.007.

[131] W. Sun, S. Choi, B. Kim, and J. Park, “Three-dimensional (3D) Vertical Resistive Random-Access Memory (VRRAM) Synapses for Neural Network Systems,” *Materials (Basel).*, vol. 12, no. 3451, 2019, doi: 10.1002/9781119207153.app2.

[132] O. Krestinskaya and A. P. James, “Feature extraction without learning in an analog spatial pooler memristive-CMOS circuit design of hierarchical temporal memory,” *Analog Integr. Circuits Signal Process.*, vol. 95, no. 3, pp. 457–465, 2018, doi: 10.1007/s10470-018-1161-1.

[133] J. Du Shiming Zhou and L. Sun, *Handbook of Spintronics*. 2016.

[134] A. He, T. Ma, J. Zhang, W. Luo, and M. Yan, “Antiferromagnetic Mn50Fe50 wire with large magnetostriction,” *J. Magn. Magn. Mater.*, vol. 321, no. 22, pp. 3778–3781, 2009, doi: 10.1016/j.jmmm.2009.07.038.

[135] T. Ma, J. Zhang, A. He, and M. Yan, “Improved magnetostriction in cold-rolled and annealed Mn50Fe50 alloy,” *Scr. Mater.*, vol. 61, no. 4, pp. 427–430, 2009, doi: 10.1016/j.scriptamat.2009.04.036.

[136] J. T. Lenkkeri, “Measurements of elastic moduli of face-centred cubic alloys of transition metals,” *J. Phys. F Met. Phys.*, vol. 11, no. 10, pp. 1991–1996, 1981, doi: 10.1088/0305-4608/11/10/008.

[137] C. Zhang, S. Fukami, H. Sato, F. Matsukura, and H. Ohno, “Spin-orbit torque induced magnetization switching in nano-scale Ta/CoFeB/MgO,” *Appl. Phys. Lett.*, vol. 107, no. 1, pp. 1–5, 2015, doi: 10.1063/1.4926371.

[138] N. S. Gusev, A. V. Sadovnikov, S. A. Nikitov, M. V. Sapozhnikov, and O. G. Udalov, “Manipulation of the Dzyaloshinskii-Moriya Interaction in Co/Pt Multilayers with Strain,” *Phys. Rev. Lett.*, vol. 124, no. 15, p. 157202, 2020, doi: 10.1103/PhysRevLett.124.157202.

[139] Z. Li *et al.*, “Strain-controlled skyrmion creation and propagation in ferroelectric/ferromagnetic hybrid wires,” *J. Magn. Magn. Mater.*, vol. 455, pp. 19–24, 2018, doi: 10.1016/j.jmmm.2017.07.008.

[140] J. M. Hu, T. Yang, and L. Q. Chen, “Strain-mediated voltage-controlled switching of magnetic skyrmions in nanostructures,” *npj Comput. Mater.*, vol. 4, no. 1, pp. 1–7, 2018, doi: 10.1038/s41524-018-0119-2.

[141] C. Zhang *et al.*, “Magnetotransport measurements of current induced effective fields in Ta/CoFeB/MgO,” *Appl. Phys. Lett.*, vol. 103, no. 26, pp. 1–4, 2013, doi: 10.1063/1.4859656.